Measurement of Hadronic Form Factors in Semileptonic B Meson Decay

Thesis by

J. Stephen Miller

In Partial Fulfillment of the Requirements

for the Degree of

Doctor of Philosophy



California Institute of Technology

Pasadena, California

1998

(Submitted January 6, 1998)

© 1998
J. Stephen Miller
All Rights Reserved

Acknowledgements

When I arrived at Caltech over seven years ago to start doing experimental particle physics, I knew next to nothing about computer programming and the data analysis techniques needed to do research, and even less about the Standard Model and B mesons I was going to study. To have now arrived at a finished thesis is in large part due to the contributions of many individuals, both collaborators and those outside of physics, most of whom I do not have space to mention.

I thank all of my CLEO collaborators who have built and maintained an experiment that has taken the quality data used for this measurement. The CESR staff deserve recognition for the excellent performance of the accelerator.

My advisor, Alan Weinstein, has taught me a great deal about data analysis and particle physics. His enthusiasm for the subject has deepened my own interest, and he suggested the topic of this thesis. Caltech postdocs Jon Urheim, Doug Cowen and Chris O'Grady played significant roles in guiding my work on this subject as well as work on the SVD upgrade. My fellow graduate student Mandeepa Chadha survived many of the rigors of grad school at the same time as I did and made a great office mate.

For all those who played intramural and pick-up soccer with me over the past seven years, thanks for all the fun moments you helped create.

My parents and family have always been a strong support for me and encouraged my interest in asking "how and why" to develop. I am grateful to them for the love and support they have given me.

To my baby daughter, Annalane, thanks for the gurgles and smiles. It is a wonderful responsibility to be your daddy. For my wife Kathy, your deep friendship and love have been a wonderful gift. It is to you I dedicate this thesis.

Ultimate thanks, indeed worship, belongs to God; for creating beauty in the universe and giving us the minds to see it.

Abstract

We measure the hadronic form factors in the decays $B^- \to D^{*0}\ell^-\bar{\nu}$ and $\bar{B}^0 \to D^{*+}\ell^-\bar{\nu}$ using both electron and muon decay modes. The analysis is based on 2.36 fb^{-1} of data taken with the CLEO detector operating at the Cornell Electron Storage Ring. The quantities measured are the ratio of form factors R_1 and R_2, and the overall form factor slope $\rho^2_{A_1}$.

We perform a 3 parameter fit over the four-dimensional kinematic space describing the decay. For the mode $B^- \to D^{*0}\ell^-\bar{\nu}$ we measure $R_1 = 1.48 \pm 0.42 \pm 0.19$, $R_2 = 0.88 \pm 0.26 \pm 0.09$ and $\rho^2_{A_1} = 0.72 \pm 0.22 \pm 0.09$. For $\bar{B}^0 \to D^{*+}\ell^-\bar{\nu}$ we obtain $R_1 = 1.16 \pm 0.35 \pm 0.13$, $R_2 = 0.65 \pm 0.27 \pm 0.10$ and $\rho^2_{A_1} = 0.94 \pm 0.18 \pm 0.06$. We also perform a combined fit to both modes which yields the result $R_1 = 1.29 \pm 0.27 \pm 0.11$, $R_2 = 0.76 \pm 0.19 \pm 0.07$ and $\rho^2_{A_1} = 0.84 \pm 0.14 \pm 0.05$.

These results support the Heavy Quark Effective Theory (HQET) estimate of $R_1 \approx 1.3$ and $R_2 \approx 0.8$; and provide a measurement of $\rho^2_{A_1}$ which is not calculated in HQET.

Contents

Acknowledgements iii

Abstract iv

1 Introduction 1

1.1 Elementary Particles 1

1.2 Fundamental Forces 5

1.3 The Standard Model 9

1.4 B Meson Production and Decay 10

1.5 Aspects of the Standard Model 15

1.6 Review of B Meson Properties 17

1.6.1 B Production 17

1.6.2 B Lifetime 19

1.6.3 B Mass 19

1.6.4 B Decays 19

1.6.5 B Mixing 21

1.7 Semileptonic Decays 21

2 Theory of $\bar{B} \to D^* \ell^- \bar{\nu}$ Decay 28

2.1 Description of $\bar{B} \to D^* \ell^- \bar{\nu}$ Decay 28

2.1.1 Decay Amplitude 28

2.1.2 Helicity Form Factors 29

2.1.3 Decay Kinematics 30

2.1.4 Decay Distribution 30

2.1.5 Decay Asymmetries 34

2.2 Heavy Quark Effective Theory 37

2.3 Ratios of Form Factors 41

2.4 Form Factor Models 42

3 The CLEO Experiment **45**

3.1 CESR 45

3.2 The CLEO Detector 46

3.2.1 Tracking 47

3.2.2 Time of Flight 51

3.2.3 Crystal Calorimeter 52

3.2.4 Muon Chambers 55

3.2.5 Lepton Identification 55

3.2.6 Trigger and Data Acquisition 57

3.2.7 Offline Reconstruction 59

3.2.8 Monte Carlo Simulation 59

4 Data Analysis **61**

4.1 Event Selection 61

4.2 Backgrounds 68

4.2.1 Combinatoric Background 68

4.2.2 Correlated Background 71

4.2.3 Uncorrelated Background 75

4.2.4 Continuum Background 77

4.2.5 Lepton Fakes 78

4.3 Branching Ratio 80

5 Fitting Method **83**

5.1 Fit Variables 83

5.2 Fit Technique 87

5.3 Fit Backgrounds 89

5.4 Information and Minimum Error 96

6 Fit Results **102**

6.1 Standard Fit Results 102

6.2 Alternative Fitting Forms 103
6.3 Goodness of Fit 108

7 Systematic Errors **115**

7.1 Efficiency 115
7.2 Systematics of Fitter 117
7.2.1 Fit Volume Size 117
7.2.2 Monte Carlo Statistics 121
7.3 Fit Backgrounds 123
7.3.1 Correlated Background 123
7.3.2 Combinatoric Background 124
7.3.3 Uncorrelated Background 125
7.4 Decay Radiation 128
7.5 Combined Fit Systematic Errors 129
7.6 Comparison between Electrons and Muons 130
7.6.1 The Nature of the Difference 131
7.6.2 Source of the Difference 133

8 Conclusions **140**

8.1 Summary of Results 140
8.2 Tests of Factorization 141
8.3 Lorentz Structure of $\bar{B} \to D^* \ell^- \bar{\nu}$ 144
8.4 Other Form Factor Results 147
8.5 Measurement of $|V_{cb}|$ 148

A $\bar{B} \to D^* \ell^- \bar{\nu}$ Decay Details **151**

A.1 Phase Space 151
A.2 Decay Amplitude 153
A.2.1 Helicity Formalism 154
A.2.2 Decays with Massive Leptons 158
A.2.3 Partial Wave Amplitudes 160

A.3 CP Violating Terms 161

Bibliography **165**

List of Figures

1.1 A picture of the constituents of matter. 6
1.2 A picture of B meson decay. 9
1.3 Illustration of $B\bar{B}$ meson production. 11
1.4 The decay chain studied in this thesis. 13
1.5 The hadronic cross section in the region of the Υ resonances. 18
1.6 B decay diagrams. 22
1.7 B mixing diagrams. 22

2.1 Angles describing $\bar{B} \to D^* \ell^- \bar{\nu}$ decay. 31
2.2 The differential decay distribution in one-dimensional projections. . . 32
2.3 The differential decay distribution in two-dimensional projections. . . 33
2.4 Differential q^2 distribution for helicity states. 34
2.5 Schematic of D^* helicity configurations. 35
2.6 Shape of the Isgur-Wise function $\xi(w)$. 40

3.1 The Cornell Electron Storage Ring. 46
3.2 The Cleo Detector. 48
3.3 Event display of $B^- \to D^{*0} \mu^- \bar{\nu}_\mu$. 49
3.4 $\mathrm{d}E/\mathrm{d}x$ energy loss versus track momentum. 51
3.5 $1/\beta$ versus momentum, using the barrel TOF. 52
3.6 Invariant mass of photon pairs in the barrel calorimeter. 54
3.7 Ratio of calorimeter energy cluster to matching track momentum. . . 56
3.8 Track penetration in muon chambers. 57

4.1 Signal MC kinematic distributions. 62
4.2 Electron and muon momentum and associated lepton identification. . 64
4.3 Kinematic quantities of D^* decay products. 65

4.4 The Dalitz plot for the decay $D^0 \to K^-\pi^+\pi^\circ$. 66
4.5 The Dalitz amplitude for the decay $D^0 \to K^-\pi^+\pi^\circ$. 67
4.6 The definition of the angle θ_{BY}. 68
4.7 The D^*–D^0 mass difference for $D^{*+}(K\pi)$ events. 69
4.8 The D^*–D^0 mass difference for $D^{*0}(K\pi)$ events. 69
4.9 The D^*–D^0 mass difference for $D^{*0}(K\pi\pi^\circ)$ events. 70
4.10 D^0 candidate mass distributions. 73
4.11 The δm distribution of flipped events. 78

5.1 Resolution using the "average" rest frame. 84
5.2 Resolution versus kinematic variables. 85
5.3 The efficiency across the kinematic variables. 86
5.4 The δm distributions for the $D^{*0}(K\pi)$ combinatoric background samples. 91
5.5 The δm distribution for the total $D^{*0}(K\pi)$ combinatoric background. 92
5.6 The δm distributions for the $D^{*0}(K\pi\pi^\circ)$ combinatoric background samples. 93
5.7 The δm distributions for the $D^{*+}(K\pi)$ combinatoric background samples. 94
5.8 Number of MC events per data point. 96
5.9 One-dimensional projections of the information for the fit parameters. 99
5.10 The minimum error expected as a function of the fit parameter. . . . 99
5.11 Two-dimensional projections of the information on R_1. 100
5.12 Two-dimensional projections of the information on R_2. 101

6.1 Fit projections of the $D^{*0}(K\pi)$ mode. 104
6.2 Fit projections of the $D^{*0}(K\pi\pi^\circ)$ mode. 104
6.3 Fit projections of the $D^{*+}(K\pi)$ mode. 105
6.4 Fit projections for the combined fit. 105
6.5 2-D projections of the data. 106
6.6 2-D projections of the fit result. 106
6.7 Projections of each of the $D^{*0}(K\pi)$ backgrounds. 107
6.8 Projections of each of the $D^{*+}(K\pi)$ backgrounds. 108

6.9 q^2 versus $\cos\theta^*$. 109
6.10 Contour of R_1 versus R_2. 110
6.11 Contour of R_2 versus $\rho^2_{A_1}$. 110
6.12 2-D projections of data-fit difference. 113
6.13 $-\ln\mathcal{L}$ per event distribution. 114

7.1 Slow pion efficiency. 116
7.2 Lepton efficiency. 117
7.3 Fitted R_1 versus generated R_1. 118
7.4 Fitted R_2 versus generated R_2. 118
7.5 Fitted $\rho^2_{A_1}$ versus generated $\rho^2_{A_1}$. 119
7.6 Volume size dependence of fit result. 120
7.7 Comparison of background shape in sideband and signal regions. . . . 122
7.8 Comparison of $D^{*+}(K\pi)$ δm sideband data and MC. 126
7.9 Comparison of $D^{*0}(K\pi)$ δm sideband data and MC. 126
7.10 Comparison of $D^{*0}(K\pi\pi^\circ)$ δm sideband data and MC. 127
7.11 Comparison of uncorrelated background and signal MC. 128
7.12 Variation in fit result with MM^2 cut. 134
7.13 Variation in slope result with MM^2 cut. 135
7.14 Fit projections for electrons. 136
7.15 Fit projections for muons. 137

8.1 Transverse and longitudinal polarization dependence on q^2. 143
8.2 The asymmetries a_{FB} and a_A as functions of q^2. 145
8.3 $\cos\theta^*$ versus χ. 146
8.4 The plot of $h_{A_1}(w)$. 150

A.1 Definition of azimuthal decay angles. 155
A.2 Differential q^2 distribution for partial wave amplitudes. 161
A.3 T-odd observables. 164

List of Tables

1.1 CKM matrix elements measured in semileptonic decays. 26
1.2 Form factor measurements from semileptonic kaon decays. 26
1.3 Form factor measurements from semileptonic $D^{(*)}$ decays. 27

2.1 Predictions of form factor models. 44

4.1 Combinatoric background yields. 72
4.2 D^{**} background estimate 75
4.3 Estimate of other correlated backgrounds. 76
4.4 Uncorrelated background numbers. 77
4.5 The $D^{*+}(K\pi)$ yield and backgrounds. 79
4.6 The $D^{*0}(K\pi)$ yield and backgrounds. 79
4.7 The $D^{*0}(K\pi\pi^{\circ})$ yield and backgrounds. 80
4.8 $\bar{B}^0 \to D^{*+}\ell^-\bar{\nu}$ branching ratio numbers. 80
4.9 $B^- \to D^{*0}\ell^-\bar{\nu}$ branching ratio numbers. 81

5.1 Branching ratios for weighting combinatoric modes. 95
5.2 The background fractions in the fit. 95
5.3 Minimum errors predicted by Cramer-Rao theorem. 98

6.1 Individual and combined fit results. 102
6.2 Individual fit results for the D^{*0} modes 103
6.3 Fits with alternative fitting functions. 111
6.4 Comparison of models with data. 111
6.5 χ^2 confidence levels of fit projections. 112

7.1 Effect of changing background volume size. 123
7.2 Variation of D^{**} background in the fit. 124

7.3 Measured slopes from data and MC sideband comparison. 125
7.4 Systematic errors. 130
7.5 Combined fit result systematic errors. 131
7.6 Fit results for lepton samples. 132

8.1 Longitudinal polarization for $q^2 = m_V^2$. 144
8.2 Measurements and predictions of decay asymmetries. 145
8.3 Measurements of $\hat{\rho}^2$. 148

Chapter 1 Introduction

In *The Nature of the Physical World*, the physicist Arthur Eddington describes two different tables. One is the solid table that we use every day, to write on or eat off of or to support books and papers. This table is the one people think of when talking about tables and it is experienced as a solid or "substantial" table. The other kind of table is the "scientific" one which is mostly empty space and consists of infinitesimal particles held together by force fields. This quantum description of the world, is vastly different from the world we experience, yet the details of that world determine what we experience [1].

This chapter gives a general introduction to how physicists describe that world, and how this thesis contributes to that understanding. Sections 1.1 to 1.4 give a basic introduction for the non-physicist of what we know about particles and forces, and how we experimentally study them. Sections 1.5 and 1.6 give more detail on specifics of the Standard Model and B mesons.

1.1 Elementary Particles

In the early 1800's, science described a world in which everything was made of tiny atoms, with a different kind of atom for each element. Elements were observed to have different properties and it was discovered that atoms of different elements combined to produce compound materials with altogether new properties. The elements in compound materials could also be separated into their constituent atoms. As more kinds of elements were discovered, it was observed that certain groups of elements had similar chemical properties, and that as one arranged the elements according to increasing mass, the same chemical properties reappeared in a periodic fashion. This *classification* of elements by mass and chemical properties in the periodic table by Dmitry Mendeleyev in 1869 was central in the development of science, but

understanding *why* the pattern was regular did not occur until about 50 years later. Furthermore, the idea of atoms was mostly conceptual, since atoms were too small to be directly observed.

The reason atomic elements can be organized in the periodic table, and have similar properties, is that elements are not elementary. All atoms are made up of electrons, protons and neutrons[1]. The protons and neutrons form the nucleus at the center of the atom, and the electrons move around the nucleus. A neutral atom has equal numbers of electrons and protons. It is the number of protons that distinguishes the different types of elements from each other. The chemical properties of an element are determined by how the electrons are arranged in orbits around the nucleus. The more massive elements have more protons and electrons. As the electron orbits are filled, the same orbital patterns are repeated on a periodic basis, leading to elements with very similar chemical properties.

This understanding of the atom started one hundred years ago when J. J. Thompson discovered the first elementary particle, the electron. Electrons were found to have a negative electric charge and a very small mass. Since atoms are electrically neutral, it was realized that electrons and some kind of positive material were combined in the atom, and that electrons could be separated from the atom. The structure of the atom was discovered a few years later in 1911, when Ernest Rutherford directed α particles[2] at a thin film of gold. To his surprise most of the α particles passed right through the gold film without being slowed down, showing that atoms are made mostly of empty space. However, some of the particles bounced straight back. This led to the understanding explained above, of the atom being mostly empty space with protons contained in the nucleus, which is surrounded by the electrons. The nucleus also has most of the mass of the atom. To understand the amount of empty space, imagine that the protons are the size of marbles, in that case the electrons would be about 100 meters distant from the nucleus. The electrons themselves do not have a measurable size, and are considered point-like particles.

---

[1] The simplest hydrogen atom only has one electron, one proton and no neutrons.

[2] At that time, α particles were seen as heavy, positively charged particles coming from certain radioactive elements. Now we know they are made of 2 protons and 2 neutrons.

In Eddington's day, during the late 1920's and early 1930's when "modern physics" was being developed, it was believed that protons and electrons were the elementary constituents of matter. Soon after, however, the neutron was discovered and found to have a mass very close to that of the proton. The study of the atomic nucleus started and neutrons and protons were found to have other similar properties, although the proton is positively charged and the neutron is electrically neutral.

Around the same time, other elementary particles were discovered in the form of cosmic rays. Cosmic rays are elementary particles that are produced when highly energetic protons from space collide with atoms in the upper atmosphere. Most of these produced particles lose their energy traveling through the atmosphere and are stopped, although some make it to the earth. At sea level, about one cosmic ray per second passes through an area the size of your hand.

One of the remarkable discoveries in the study of cosmic rays was of anti-matter. For every elementary particle, there is a corresponding anti-particle which has the same mass but opposite charge. When a particle and its anti-particle collide, they annihilate each other into energy. The first anti-particle observed was a positively charged electron, called a positron. When a positron collides with an electron, both are annihilated to become light energy. There are also anti-protons and anti-neutrons.

Another discovery was that of muons, which make up most of the cosmic rays hitting the ground. Muons are particles that are just like electrons in every way, except they are about 200 times more massive than electrons, and they radioactively decay, producing an electron and neutrinos. Neutrinos are neutral, massless partners of electrons and muons and are quite difficult to detect. There is one type of neutrino associated with electrons, and one type associated with muons. Electrons, muons and neutrinos are all classified as leptons. There is a third charged lepton called a tau which is otherwise like a muon except for being 17 times more massive than a muon. The tau also has a corresponding neutrino. The leptons are organized into three families of doublets.

charge	Family 1	Family 2	Family 3
-1	electron (e)	muon (μ)	tau (τ)
0	electron neutrino (ν_e)	muon neutrino (ν_μ)	tau neutrino (ν_τ)

Other elementary particles were also discovered in cosmic ray experiments. These particles came in two general varieties called mesons and baryons. Specific mesons have names such as "pion" or "kaon," or π or K for short. Protons and neutrons are examples of baryons. These particles also come in charged and neutral varieties, along with their corresponding anti-particles.

Before long many different mesons and baryons were discovered and it was found that they could be classified according to their properties. This led to the idea that these "elementary" particles were composed of even smaller particles. In the early 1960's the quark model was proposed which explained all of the mesons and baryons as being made of combinations of quarks. A meson is a combination of a quark and an anti-quark, and a baryon is a combination of three quarks. At that time, only three different types of quarks were needed to explain all the particles. These quarks are called "up," "down" and "strange," or u, d and s for short. The up quark has an electric charge of +2/3 and a down quark has a charge of -1/3. Two up quarks and one down quark make a proton with a total charge of +1. Two down quarks and one up quark make a neutron which has a total charge of zero. A π^+ meson is made of an up quark and an anti-down quark. Its anti-particle, the π^- meson, is made of a down quark and an anti-up quark. There is also a π° meson made of an up and anti-up quark. The superscript refers to the meson's charge. Since then, three other quarks have been discovered, and are called "charm," "bottom" and "top," or c, b and t. Just like the leptons, the quarks are also arranged in three families of doublets.

charge	Family 1	Family 2	Family 3
$+2/3$	up (u)	charm (c)	top (t)
$-1/3$	down (d)	strange (s)	bottom (b)

As each family number increases, the quark masses increase. The up and down quarks are the least massive, the strange quark is about 20 times more massive than the up and down quarks. A charm quark is between 5 to 10 times more massive than a strange quark, a bottom quark is 3 to 4 times more massive than a charm quark, and a top quark is about 40 times more massive than a bottom quark. The top quark has about the same mass as a gold atom.

The B meson studied in this thesis comes in two types. The B^- meson is made of a bottom (b) quark and anti-up ($\bar{u}$) quark. (The horizontal bar indicates an anti-particle.) The $\bar{B}^0$ meson is made of a b and $\bar{d}$ quark. Both types of B meson have a corresponding anti-meson with $\bar{b}$ quarks. These are referred to as the B^+ and B^0 mesons[3].

Today quarks and leptons would be considered the truly "elementary" constituents of matter, and perhaps they are. But the pattern of three families for both quarks and leptons is suggestive of even a smaller set of particles that make up quarks and leptons. In fact, it is not known if there are only three families, although if there were more, the particles would be significantly more massive than the ones currently observed. It is also not known why the particles have the masses they do, or even why they have the property we call mass. Figure 1.1 illustrates our current understanding of matter.

1.2 Fundamental Forces

To understand the subatomic world, it is not enough to say what the elementary particles are; one must understand how they are held together, and how they decay into other particles. This is done by learning about the forces that govern their interactions. There are four known forces: gravity, electromagnetism, the strong force, and the weak force. Each force has an associated particle, generically called a boson, and it is by exchanging these bosons that the particles interact.

[3]Because of an odd historical naming convention, the $\bar{B}^0$ meson has a b quark and the B^0 meson has a $\bar{b}$ quark.

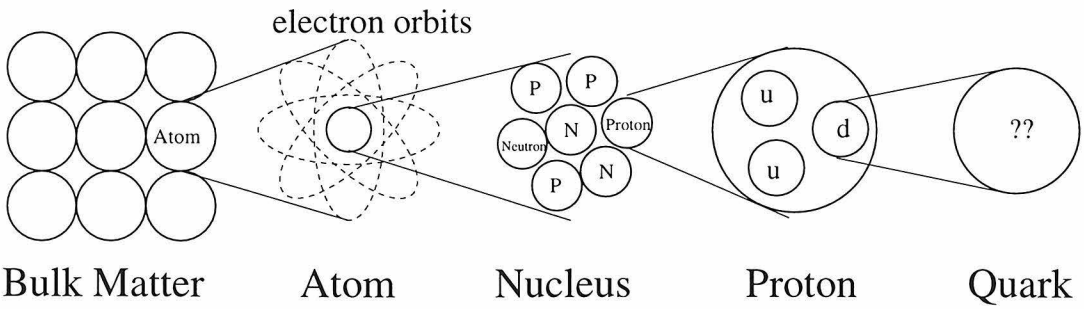


Figure 1.1: A picture of the constituents of matter. The actual size of the nucleus relative to the electron orbits, and the quark sizes relative to the proton size are greatly exaggerated. Their size would more accurately be represented by a tiny dot too small to be seen.

Gravity has been mathematically described since 1665 when Isaac Newton wrote an equation to describe the gravitational force. Gravity's force is easily experienced since it is always pulling us towards the earth. However, for particle physicists, gravity is the least understood force, and there isn't a good theory of how two subatomic particles would gravitationally attract each other. Fortunately, gravity is so weak relative to the other forces, that it can be ignored when describing the interaction of elementary particles. We only feel gravity since its force is felt over long distances, and it always attracts particles together. Since the earth is made of an enormous number of electrons and quarks, each of them only has to pull on us a little bit, for us to feel the total effect. It should be mentioned that Einstein's theory of general relativity gives an extremely accurate description of gravity when applied to bunches of particles, such as planets orbiting the sun, or someone falling out of bed in the morning. Having a theory which can explain gravity in the language of particle physics, as well as include general relativity is one of the most important problems of modern physics.

Electric and magnetic forces are used in every day life and provide the basis of modern technology. Besides the obvious example of electricity, the energy released in chemical reactions is also a manifestation of electric force, and it is this energy which is used to sustain life. In 1865, James Clerk Maxwell made the important discovery

that electricity and magnetism were just two different manifestations of the same force, now called electromagnetism, and furthermore that light is a manifestation of that force. What we know as visible light is just a small part of the electromagnetic spectrum which includes radio waves, microwaves, infrared, visible and ultraviolet light, as well as x-rays and gamma rays. All are manifestations of the same force. We now understand that electromagnetic energy comes in little packets of energy, or particles, called photons. Objects that interact via electromagnetic forces, do so by exchanging photons. It is this force which keeps the negatively charged electrons orbiting around the positively charged protons in the nucleus.

Light also is made of photons, with short wavelength light corresponding to higher energy photons. Ultraviolet (UV) light has a wavelength about one tenth that of visible light, and thus ultraviolet photons have ten times the energy of a visible light photon. That is why UV rays are the ones which cause sunburn. X-rays have an even shorter wavelength and an energy over a thousand times greater than light. That is why x-rays are highly penetrating and also cause significant damage. The high energy photons, called gamma particles, observed at high energy physics experiments are typically between 10 million and 10 billion times more energetic than a visible light photon.

The electromagnetic force acts between charged objects with the property of attracting objects of opposite charge and repelling objects of like charge. Like gravity, it is also a long range force, with the property that the force becomes weaker as the distance between the two objects increases. This property is readily apparent when pulling two magnets apart. Although it can act over long distances, the electromagnetic force is not "felt" as strongly as gravity, even though it is intrinsically far stronger. That is because atoms are made of equal numbers of electrons and protons and so have a net charge of zero. If one is far from the atom, one cannot distinguish the location of the electrons and protons in the atom and so their charges cancel giving an electrically neutral atom and no force is felt. Another way to say it is that the electrons and protons are equally repelling and attracting and so the net force experienced by a distant charged particle is zero.

As previously mentioned, the nucleus is made of positively charged protons, and neutral neutrons. The protons are electrically repelled from each other, but are held in the nucleus by the "strong" force, so called since it is about 100 times stronger than the electromagnetic force. The strong force is also what holds quarks together to make baryons and mesons. Quarks have a strong force charge, called "color" charge, that comes in three types, called "blue," "red," and "green." Each type of color can be either the color or the anti-color charge. In contrast, electric charge has only one type, which is either plus or minus. The strong force combines color-charged objects so that there is no net "color." This can be done by combining a color and anti-color charge together, such as red and anti-red, and similarly for the others. The other way to get a colorless object is to combine one red, one blue and one green charged object. This is analogous to how a television screen combines red, blue and green light to make white light. It is this strong force property of always making "colorless" objects that means quarks always combine in groups of three (baryons) or quark anti-quark pairs (mesons). The strong force is carried by particles called gluons, and quarks are held together by exchanging gluons. The strong force has the property that as two quarks get farther apart, the strength of the force between them remains constant. In contrast, the electromagnetic force gets weaker as the separation distance increases. This property ensures that quarks are always bound with other quarks. Leptons do not have color charge and do not interact via the strong force. As a result, leptons can exist separately from other particles.

The fourth force is called the weak force, and has about the same strength as the electromagnetic force. However, the weak force does not hold particles together since it can only act over extremely short distances. Instead, the weak force is responsible for radioactive decay, since it has the property of turning a quark or lepton into a lighter quark or lepton. The weak force is carried by one of three particles called W^+, W^-, and Z^0 bosons. Unlike the other force carriers, the photon and gluon, the weak force bosons have mass. In fact, it is this property of having mass that makes the weak force a short range force.

The weak decay of a meson is illustrated in Figure 1.2. A quark inside the meson

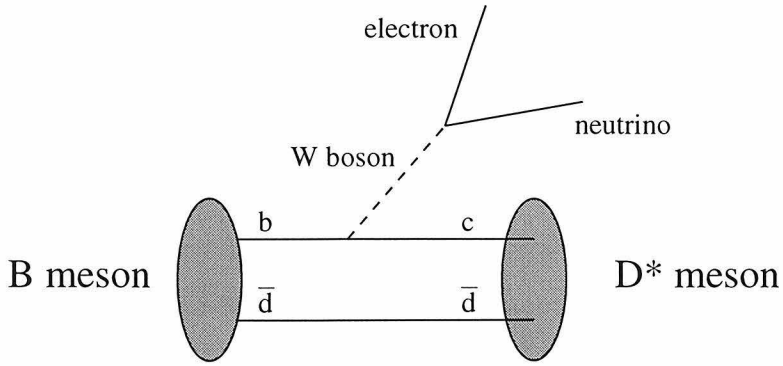


Figure 1.2: This is a picture of B meson decay. The b quark inside the B meson changes into a c quark by emitting a weak force W boson. The W immediately decays to produce an electron and neutrino. The c quark pairs up with the leftover $\bar{d}$ quark to form a D^* meson.

decays by emitting a weak force W particle and turning into a lighter quark. The W immediately turns into either a quark and an anti-quark, or a lepton and its corresponding (anti-)neutrino. Since quarks are bound to other quarks by the strong force, the new quark produced is immediately bound to the other quark in the meson. If two new quarks are produced from the W particle, they will also combine to form another meson. If instead the W particle turns into leptons, the leptons will fly off separately since they are not bound by the strong force. Studying this type of decay for a bottom quark in a B meson is the subject of this thesis.

1.3 The Standard Model

Around 30 years ago, a theory was developed which said the electromagnetic and weak forces were both manifestations of the same force called the electroweak force. This unification of the forces is similar to the unification of electricity and magnetism which occurred 100 years earlier. The electroweak theory has been repeatedly confirmed by a large number of experiments. That theory plus the theory of the strong force, along with the families of quarks and leptons, constitute our most basic understanding of the physical world. This understanding is referred to as the Standard Model.

Although the Standard Model has been enormously successful in describing ex-

periments, physicists believe it is an incomplete description and will someday be incorporated into an even more comprehensive theory. One expectation of this new theory is that it will unify the strong and electroweak forces and describe them as manifestations of just one force. It is also expected that gravity will be included in this way as well. As mentioned, there is also the possibility that leptons and quarks will be described as being made of yet more fundamental particles. There is also the possibility of finding other elementary particles that might be similar to quarks and leptons, yet much more massive which would explain why they have not yet been observed.

1.4 B Meson Production and Decay

Only the first family of particles, electrons and the up and down quarks, which make up protons and neutrons, are found in the stuff of everyday matter. That is because the heavier quarks and leptons decay to the least massive particles. Only some of the other heavier quarks and leptons have been observed in cosmic rays, but not enough to study in great detail. To study the short lived heavier particles, physicists create them in particle accelerators. One type of accelerator, called an electron-positron collider, takes electrons and uses an electric field to accelerate the electrons to nearly the speed of light. The electrons are kept moving in a circular trajectory, by being kept inside an airless tube. At the Cornell Electron Storage Ring (CESR), where this thesis research was carried out, the circular ring is about 800 meters in circumference. Figure 3.1 illustrates the storage ring. Anti-electrons (positrons), which are first made by colliding energetic electrons into a metal target, travel in the opposite direction inside the ring and are made to collide with the electrons.

When an electron and a positron collide, they annihilate each other and their energy of motion is converted to electromagnetic energy which is immediately turned into a pair of leptons or a pair of quarks. The only requirement to produce a given pair of quarks or leptons, is that the energy of the collision is greater than the energy equivalent of the mass of the produced quark or lepton pair. For a given collision,

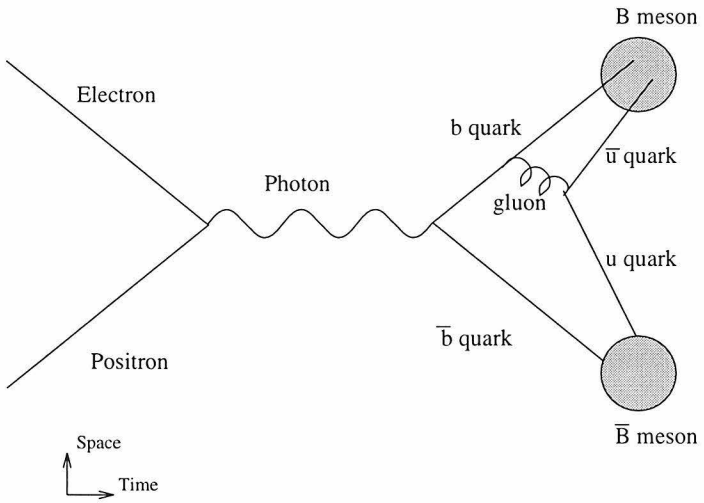


Figure 1.3: This is a picture of B meson production. The vertical axis shows distance and the horizontal axis is the change in time. The electron and positron collide and annihilate to form a photon which turns into a $b\bar{b}$ quark pair. A gluon is also produced giving rise to a $u\bar{u}$ quark pair which combine with the b and $\bar{b}$ quarks to produce a B and $\bar{B}$ meson. The quarks in the meson are held together by many gluons which are not drawn.

one cannot know what will be produced, but there is a fixed probability for each type of quark or lepton to be produced. At CESR, there is enough energy to produce a bottom and anti-bottom quark pair, which happens in 1 out of every 20 annihilations. All other quark and lepton types are also produced at CESR, except the top quark which would require a machine with 35 times more energy.

As the produced bottom and anti-bottom quarks move apart, the strong force binding them becomes stronger. In fact, it becomes strong enough to produce either an up quark and an anti-up quark, or a down and an anti-down quark. Each of these quarks pairs with one of the b quarks to form a pair of B and anti-B ($\bar{B}$) mesons. Figure 1.3 illustrates electron-positron annihilation and B meson production.

The B mesons typically exist for about a trillionth of a second before decaying to other mesons, baryons and leptons. There are many different decays possible, and there is a different probability for each type of decay to occur. Studying how often a specific final state occurs tells us about the nature of the strong and weak forces. The

decay of the B meson to a D^* meson plus an electron and neutrino occurs about 5% of the time, and is the single most common decay of the B meson. A D^* meson is a combination of a charm quark and either an up or down anti-quark. Another 5% of the time the B meson decays to a D^* a neutrino and a muon, instead of an electron, in the final state. These are the two decays studied in this thesis.

Since the B mesons decay so quickly, they cannot be directly observed. In fact, the D^* meson is not directly observed either, since it also decays quickly. There can be a series of intermediate mesons produced which decay right away and are not detected, but eventually K and π mesons are produced which live long enough and travel far enough to be detected. Electrons and muons can be also be directly detected, but neutrinos pass right through the detector without being observed. The neutrino's presence is inferred from a deficit in the total energy observed.

The most ubiquitous particle detector is the eyeball. In this case photons, light particles, hit the retina which is made up of many rods and cones. The rods and cones measure the position and energy (color) of the photon. This information is converted to an electrical pulse which is sent to the brain. The brain processes the signals from the rods and cones to reconstruct the image which tells us something about the source of the light. A modern particle physics experiment operates on essentially the same principle, but is sensitive to not only photons, but can also detect the electrons, muons, protons and mesons which pass through it. When a particle goes through the detector, it leaves some or all of its energy along its path which can be detected and converted to electrical signals. Typically the particle's momentum, direction and/or energy is measured. This information is sent to a computer which reconstructs what kind of decay occurred. The detector used for this research is named the CLEO detector[4]. This detector is illustrated in Figure 3.2.

A common example of a charged particle detector is a television screen. In this case electrons are accelerated by a tiny particle accelerator, and directed to strike the television screen. The screen converts the motion energy of the electrons to light by means of phosphoresence. In this case the light is observed by the viewer, but a

[4]CLEO is not an acronym but a word play on the names Cleopatra and Caesar (CESR).

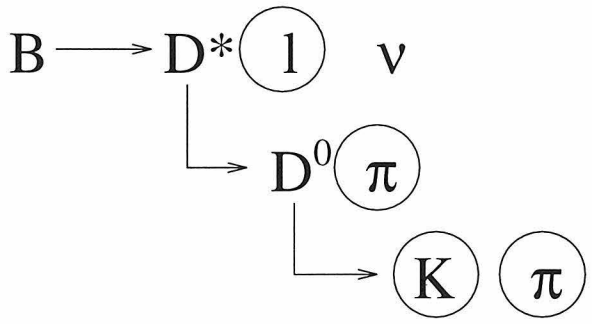


Figure 1.4: The decay studied in this thesis. Circled particles are those which are actually observed by the CLEO detector. Measuring the momentum of the particles allows us to infer which intermediate particle they came from.

particle detector would convert the light to an electrical signal. The viewer can also distinguish a meaningful pattern on the screen, if the electrons are being directed in an ordered way, for example by the signal from a television station. If the television is receiving static, just a random fuzz is observed. Much of the challenge of particle physics is to find a signal from a specific decay, amidst the random background noise due to all other decays.

This analysis studies the decay of a B meson to a D^* meson, lepton and neutrino, where the lepton is either an electron or a muon. The D^* meson also decays, and we reconstruct the D^* through its decay to a D^0 meson and a π meson. The D^0 also decays before being detected, and we reconstruct the D^0 by observing its decay to a K and a π meson, which happens about 4% of the time. Figure 1.4 graphically represents this decay chain. What is actually observed in the detector is one K meson, two π mesons, and an electron or muon. Out of over 2.5 million B meson events produced at CLEO, we expect about 3,400 events where those four particles are the result of this decay sequence. However, since we are studying both B^+'s and B^0 mesons and their decays to electrons and muons, there are four times that many events to look for.

Unfortunately, the detector is not completely efficient at observing the particles, and so we only measure all four of the final state particles less than 10% of the time. This gives about one thousand events to analyze in detail. Figure 3.3 illustrates one

of these events. Since the other B meson produced in the event also decays, there are other particles in the event besides the ones we are looking for. We cannot always distinguish which particle came from which B meson, leading to a misassignment of the measured particles. Sometimes a decay of a B meson will be similar to the signal decay we are interested in. We cannot always distinguish these fake, or "background," events from the signal events. However, we can estimate what fraction of our event sample is signal and what fraction is background. We can then account for the background events in our analysis, to avoid their biasing our results.

The momentum of the particles produced in the decay and the angles between them is determined by the weak and strong forces. By measuring the distributions of angles and momenta for the K and π mesons and electron, we can compare what is observed, with what is predicted by theory. However, for this type of decay, it is currently not possible for theory to exactly predict the results. That is because the effects of the strong force cannot be exactly calculated for this decay. As a result, the calculation must use simplifying assumptions about the strong force. This measurement is used to test how valid these simplifying assumptions are. If the assumptions are found to be valid, then they can be used for calculating other decays.

For this analysis, our results are in agreement with the predictions of theory, and thus support the Standard Model description of the decay. However, our results are only measured with a limited precision. For example, it would be like measuring an object that was a foot long, but having such a crude ruler that one could only say that it was most likely between 10 and 14 inches. That type of measurement is useful for knowing that the object is not 1 inch or 20 inches long, but cannot be used to exclude a theory that predicted the foot long object to be only 11 inches in length. Future experiments will have a larger number of events, and will be able to test the theoretical prediction with greater precision.

1.5 Aspects of the Standard Model

This section discusses only those aspects of the Standard Model which are directly related to this thesis. Comprehensive and detailed discussions of the Standard Model can be found in many other sources, for example [2]. This discussion assumes the reader is familiar with the Standard Model, and its only purpose is to place the thesis in the broader context of the Standard Model.

The Cabibbo-Kobayashi-Maskawa (CKM) matrix relates the weak quark eigenstates to the physical (mass) quark eigenstates in flavor changing weak interactions. The matrix comes from diagonalizing the mass matrix that arises from the coupling of the weak quark fields to the Higgs field. The CKM matrix is typically written as

$$\begin{pmatrix} V_{ud} & V_{us} & V_{ub} \\ V_{cd} & V_{cs} & V_{cb} \\ V_{td} & V_{ts} & V_{tb} \end{pmatrix}. \tag{1.1}$$

The matrix has nine complex elements, but since it is unitary, the nine elements can be expressed in terms of three real rotation angles and one complex phase.

Besides describing mass mixing, the CKM matrix is also used to explain CP violation in the Standard Model, which arises because of the complex phase. The values of the matrix elements are not predicted by theory and must be measured by experiment. Obtaining precise measurements of the CKM elements is important for understanding CP violation in the Standard Model, as well as testing the unitarity of the matrix.

As described in section 1.7, semileptonic decays are used for measuring the CKM matrix elements; and understanding the hadronic dynamics in semileptonic decays is crucial for extracting the CKM element. The decay $\bar{B} \to D^* \ell^- \bar{\nu}$ is used for measuring V_{cb} and relies on theoretical predictions of the hadronic form factors. This thesis provides a test of the theoretical framework used to understand the form factors.

Our understanding of the form factors is based on how well we can calculate the effects of the strong interaction in the decay. Quantum chromodynamics, the theory

of the strong interaction, has the property that the coupling strength gets stronger at low energies. This dependence is given by

$$\alpha_s(Q^2) = \frac{\alpha_s(\mu^2)}{1 + \frac{\alpha_s(\mu^2)}{12\pi}(33 - 2n_f)\log(Q^2/\mu^2)}, \tag{1.2}$$

where Q^2 is the momentum transfer, μ^2 is the scale at which $\alpha_s(\mu^2)$ is known, and n_f are the number of quark flavors. For small enough momentum transfer, the coupling strength becomes large enough that perturbation expansions are no longer valid for calculations. That energy scale occurs when the denominator of Equation 1.2 becomes small, and is given by the scale

$$\Lambda_{QCD} = \mu \exp\left(-\frac{6\pi}{(33 - 2n_f)\alpha_s(\mu^2)}\right). \tag{1.3}$$

The Q^2 dependence can then be rewritten as

$$\alpha_s(Q^2) = \frac{12\pi}{(33 - 2n_f)\log(Q^2/\Lambda^2_{QCD})}. \tag{1.4}$$

Λ_{QCD} is about 200 MeV, which sets the energy scale for binding quarks in hadrons. Form factors in semileptonic meson decay describe the effect of hadronization on the quark decay, and are also in this region of non-perturbative QCD.

Form factors can still be calculated to some degree in semileptonic decays by taking advantage of two symmetries in QCD. One is for decays of light quarks to light quarks such as in nuclear beta decay. For this decay $|m_d - m_u| << \Lambda_{QCD}$, and the form factors between the initial and final state baryons can be related to each other. This relationship between the light quarks is the reason for isospin symmetry, and can also be extended, although with larger symmetry breaking corrections, to include strange quarks in an $SU(3)$ symmetry. For heavy to heavy meson transitions, such as in $\bar{B} \to D^* \ell^- \bar{\nu}$, $m_Q >> \Lambda_{QCD}$ and another symmetry results known as Heavy Quark Symmetry (HQS). This symmetry is further discussed in section 2.2, and testing the validity of this symmetry is a goal of this thesis.

The other part of the Standard Model relevant for semileptonic decays is the

Lorentz structure of the weak current. The structure of the charged weak current has been precisely measured in muon [3] and tau [4] decays. These measurements show that the charged weak current is of the form $\bar{\psi}\gamma_\mu(1-\gamma^5)\psi$, which is a parity violating $V-A$ structure. This flavor changing current couples left-handed fermions and right-handed anti-particles. The structure of the current, the spins of the particles, and conservation of angular momentum determine the angular distributions of the decay products. For the decays of leptons this is strictly true; for quarks bound inside hadrons the strong interaction effects modify the free fermion decay distributions. Nevertheless, for hadron decays the shape of the kinematic distributions are still largely determined by the $V-A$ structure and momentum conservation. The measurement of this thesis assumes the Standard Model weak current for quark and lepton couplings, and then measures the effect of the form factors using the kinematic distributions. We can also exclude certain non-Standard Model couplings without having to rely on theoretical predictions for the form factors.

1.6 Review of B Meson Properties

This section provides a brief overview of B meson properties, in order to place the subject of this thesis in a larger context. There are numerous B reviews which provide extensive detail and explanation of B properties. Some of these [5, 6] were relied on for writing this section.

1.6.1 B Production

The b quark was discovered in 1977 when a family of resonances called Υ were found in a proton fixed target experiment at Fermilab [7]. These resonances have since been studied in detail at e^+e^- colliders. The lowest resonance called the $\Upsilon(1S)$, which has a mass of 9.460 GeV and a width of 52 keV, is a bound state of a $b\bar{b}$ quark pair. Other states of the $b\bar{b}$ system are the radially excited $\Upsilon(2S)$ and $\Upsilon(3S)$, along with a number of χ_b states where the quarks have orbital angular momentum. The χ_b states are not directly produced in e^+e^-collisions, but are observed in the decays of

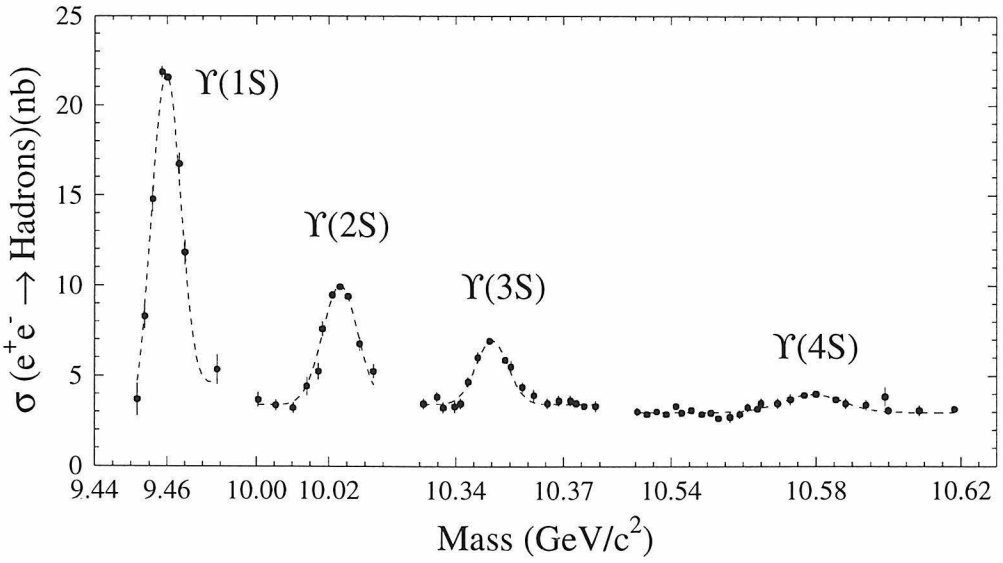


Figure 1.5: The hadronic cross section in the region of the Υ resonances.

the $\Upsilon(2S)$ and $\Upsilon(3S)$ states. Another resonance, the $\Upsilon(4S)$, was discovered at CESR and has an energy of 10.58 GeV and a width of 24 MeV which is much broader than the lower mass resonances. That is because at 10.58 GeV there is enough energy to produce not only a $b\bar{b}$ quark pair but also a $u\bar{u}$ or $d\bar{d}$ quark pair; so the $\Upsilon(4S)$ can decay to a pair of B mesons. These resonances are shown in Figure 1.5.

The $\Upsilon(4S)$ has only been observed to decay into B mesons, and the measured cross section for $e^+e^- \rightarrow B\bar{B}$ is 1.07 nb. This is about 1/4 of the total hadronic cross section at that energy. The $\Upsilon(4S)$ decays into either a pair of B^+B^- or $B^0\bar{B}^0$ mesons, but the production ratio of charged to neutral B mesons, f_{+-}/f_{00}, is not well known. The decay $\Upsilon(4S) \rightarrow B\bar{B}$ is a p-wave decay, so the rate depends on the momentum to the third power. However, the difference in the charged and neutral B masses is quite small, so this effect is negligible. Coulombic corrections could lead to an enhancement of B^+B^- production [8]. Presently f_{+-}/f_{00} has been measured to be 1.08 ± 0.18 [9], and is generally taken to be 1. We discuss this ratio further in section 4.3.

By fully reconstructing B meson decays, CLEO has measured the production angle of the B's to have a $\sin^2\theta$ distribution relative to the beam direction. The $\Upsilon(4S)$ is a $J = 1$ state, and thus gives a $\sin^2\theta$ distribution when decaying to two

spin 0 objects. That the B has spin 0 is expected since it is the lowest mass meson containing a bottom quark and an up or down quark.

1.6.2 B Lifetime

At the $\Upsilon(4S)$, the B's are produced with a β of 0.06, and travel only 30 μm on average. This distance is too short to directly measure the B lifetime. The lifetime has been measured at higher energy machines such as LEP, where the average B flight distance is 2.6 mm, and the Tevatron. These measurements are complicated by the fact that at these higher energies, other B hadrons, such as B_s, B_c, and b baryons, are produced along with the B_d and B_u mesons. The world average lifetime measurements are (1.65 ± 0.04) ps for B^-, (1.55 ± 0.04) ps for $\bar{B}^0$, with a ratio of lifetimes $\tau_{B^-}/\tau_{\bar{B}^0} = 1.06 \pm 0.04$ [10].

1.6.3 B Mass

Fully reconstructing hadronic decays of the B meson gives a measurement of the B mass. Typically, a B is fully reconstructed in the decay mode $B \to D^{(*)} n\pi$. This gives a resolution of about 14 to 46 MeV on the B energy, depending on the decay mode. However, since the $\Upsilon(4S)$ decays to two B's and nothing else, each B is produced with the beam energy which is known to within 3 MeV. This information is used to calculate the beam constrained mass which is given by $m_B^2 = E_{beam}^2 - \vec{p}_B^2$. Current measurements give $M_{B^-} = 5278.9 \pm 1.8$ MeV and $M_{\bar{B}^0} = 5279.2 \pm 1.8$ MeV. The error is dominated by systematic uncertainties which cancel in the mass difference which is measured to be 0.35 ± 0.29 MeV [3].

1.6.4 B Decays

The decays of the B^-, $\bar{B}^0$ and B_s mesons proceed via the weak interaction, and involve the change of the b quark to an up-type quark via the coupling of a W boson. Nonetheless, this interaction can happen in a number of ways, not to mention the variations introduced by the strong interaction. Because the b quark mass is quite

large relative to the first and second generation quarks, there is a large amount of energy available for producing multiple mesons in the decays. The large number of decay modes means that the largest B decay modes typically have branching fractions of a few percent at most.

The most common type of decay is the spectator decay, illustrated in Figure 1.6a. In this decay the W independently produces an $\ell\nu$ or $q\bar{q}$ pair, and the "spectator" quark in the B meson doesn't participate in the decay, except for forming a hadron with the quark directly produced from the b quark conversion. All semileptonic decays are produced via this diagram. If a pair of quarks are produced at the W vertex, then gluons can be exchanged between all the quarks in the decay, and quarks from the upper and lower vertices can combine to hadronize. There is also the possibility of strong rescattering of the mesons after hadronization, although this is much less likely in B decays than in D decays.

Internal W decays, as shown in Figure 1.6b, directly combine the quarks from the W with those from the B. These are also referred to as color suppressed decays because the quarks from the W vertex are not free to be any color, but must match that of the quarks in the original meson. This leads to a suppression factor of 1/3, relative to a spectator decay, in the decay amplitude. For some charged B decays, such as $B^- \to D^0\pi^-$, the spectator and internal W decays lead to the same final state, and there is interference between the two decay diagrams. Internal W decays have been directly observed only in the modes $B \to \psi K^{(*)}$.

Figure 1.6c illustrates an annihilation decay. This decay only occurs for charged B's and is suppressed by the coupling V_{ub}, helicity conservation, and the overlap of the quark wavefunctions, which is parametrized by the meson decay constant, f_B. This diagram gives the fully leptonic decays such as $B^- \to \tau^-\bar{\nu}_\tau$, but these have not yet been observed.

The W exchange diagram, in Figure 1.6e, only exists for neutral B's. A decay such as $\bar{B}^0 \to D_s^+ K^-$ is a clear signature for such a mode, but has not been observed at the level of 2×10^{-4}. This diagram is helicity suppressed.

The penguin diagram in Figure 1.6d gives an effective $b \to s(\mathrm{or}d)$ transition,

by means of an internal loop. If the W, or a quark, radiates a photon, then it is an electromagnetic penguin. CLEO has measured both the exclusive decay $\mathcal{B}(\bar{B} \to \bar{K}^*\gamma) = (4.2 \pm 1.0) \times 10^{-5}$ [11] as well as the inclusive rate $\mathcal{B}(b \to s\gamma) = (2.3 \pm 0.7) \times 10^{-4}$ [12]. This transition could also occur through non-standard model particles in the internal loop, and the measurement of this decay gives important bounds on new physics, for example in the Higgs sector or for supersymmetric models [13].

Penguin annihilation, as shown in Figure 1.6f, only occurs for neutral B mesons. Its hadronic final states can interfere with the final states produced by other diagrams. However, this decay mode is OZI suppressed, and the decay amplitude should be quite small relative to the other diagrams.

1.6.5 B Mixing

The neutral B's are produced as flavor eigenstates, which are linear combinations of the physical mass eigenstates that propagate. As a result, neutral B's undergo mixing via the box diagrams shown in Figure 1.7. Thus a produced B^0 can oscillate to a $\bar{B}^0$ before decaying. At CLEO, the B^0 and $\bar{B}^0$ are produced in a coherent, antisymmetric ($L = 1$) state so that both mesons mix at the same time, until one of them decays. After that time, the other B may oscillate into a $\bar{B}$ and then decay. This can result in the decay of two B^0's in the same event. The parameter $\chi_d = 0.175 \pm 0.016$ [3] is the probability that a B^0 will decay as a $\bar{B}^0$.

1.7 Semileptonic Decays

Semileptonic decays are the result of one quark species changing into another via the emission of a W boson, which then decays to a lepton and neutrino. This decay is always a spectator decay as illustrated in Figure 1.6a. Because the $\ell\nu$ system does not interact[5] with the final state quarks, the decay amplitude can be factorized into

[5]There can be an interaction between the lepton and quarks due to the exchange of a photon, but that is suppressed by α^2 in the amplitude.

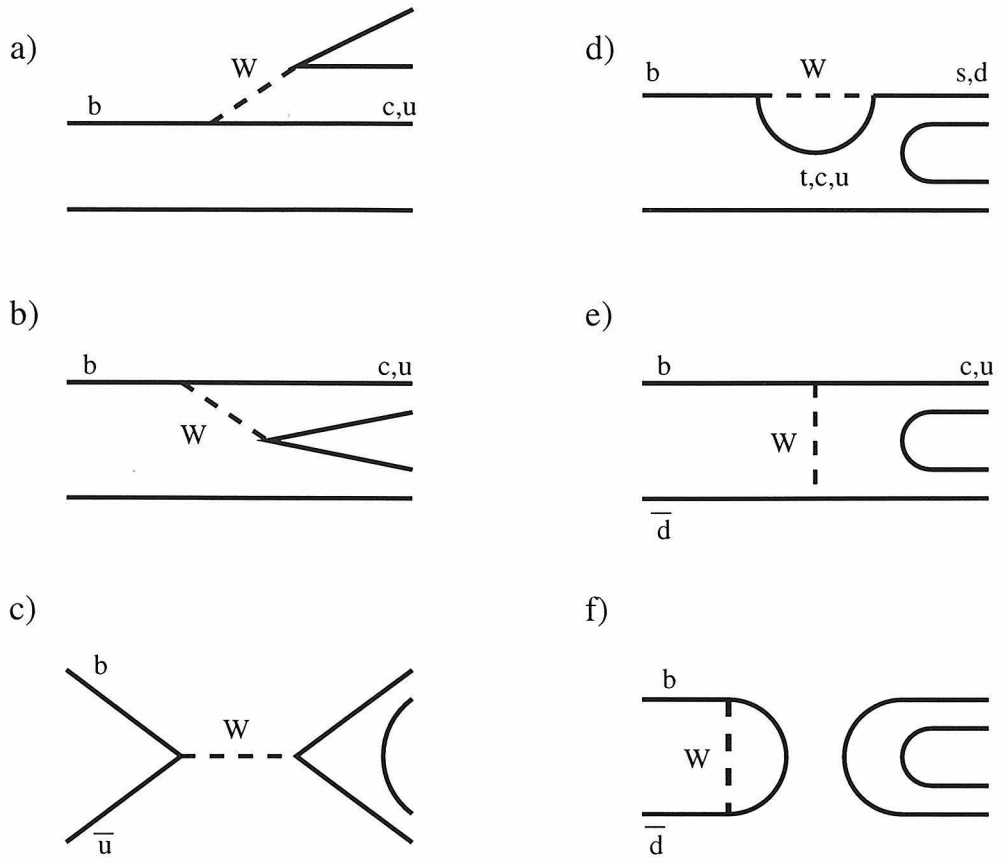


Figure 1.6: Schematic decay diagrams for B decays. The solid lines are quarks and the dashed lines are W bosons. Not shown are radiated gluons which produce quark pairs.

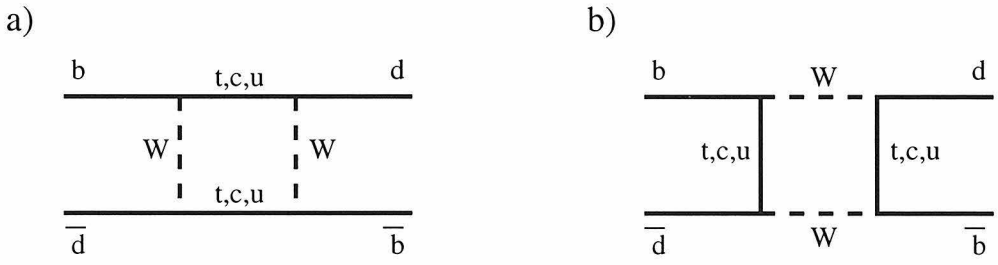


Figure 1.7: Schematic diagrams for B mixing.

separate leptonic and hadronic currents, and written as

$$\mathcal{M} = -i\frac{G_F}{\sqrt{2}} V_{q'q} L^\mu H_\mu, \tag{1.5}$$

where G_F comes from the weak coupling strength and the W propagator, and $V_{q'q}$ is the appropriate CKM matrix element (e.g., V_{cb} or V_{ub}). The leptonic current, L^μ is given by the weak current

$$L^\mu = \langle \ell\nu | \bar{u}_\ell \gamma^\mu (1-\gamma_5) v_\nu | 0 \rangle. \tag{1.6}$$

The hadronic current H_μ, such as for a $b \to c$ transition, is written

$$H_\mu = \langle \text{final meson} | c\gamma_\mu (1-\gamma_5) b | B \rangle. \tag{1.7}$$

This current cannot be calculated from the Standard Model Lagrangian because of the non-perturbative QCD effects which describe the hadron formation. Instead, the hadronic current is written in general terms using the four vectors in the decay and form factors which parametrize the QCD part of the decay. The form factors are functions of q^2, the invariant mass squared of the $\ell\nu$ system, which is the only dynamical Lorentz invariant in the decay. The form of the current depends on the spin and parity of the initial and final state hadrons. For a pseudo-scalar to pseudo-scalar transition, $0^- \to 0^-$, (e.g., $B \to D$), the hadronic current is generally written as

$$\langle M_f(k) | \bar{q}_f \gamma_\mu q_i | M_i(P) \rangle = f_+(q^2)(P+k)_\mu + f_-(q^2)(P-k)_\mu, \tag{1.8}$$

where P and k are the four vectors of the initial and final state mesons. f_+ and f_- are functions of q^2 where $q = p_\ell + p_\nu = P - k$, and q^2 varies from $q^2_{min} = m^2_\ell$ to $q^2_{max} = (m_i - m_f)^2$. For pseudo-scalar to vector transitions, $0^- \to 1^-$, (e.g., $B \to D^*$), there must be four independent form factors,

$$\langle M_f(k,\varepsilon) | \bar{q}_f \gamma_\mu (1-\gamma_5) q_i | M_i(P) \rangle = \varepsilon^{*\nu} [F_{A_1} g_{\mu\nu} + F_{A_2} P_\nu (P+k)_\mu + F_{A_3} P_\nu (P-k)_\mu$$

$$+iF_V\epsilon_{\mu\nu\rho\sigma}(P+k)^\rho(P-k)^\sigma], \tag{1.9}$$

where ε is the spin vector of the final state meson, and the constraint $\varepsilon^{*\nu}k_\nu = 0$ has been applied. The subscripts V and A denote vector and axial-vector form factors respectively. For a pseudo-scalar to spin 2 meson transition, $0^- \to 2^+$ (e.g., $B \to D_2^*$), the current is [14]

$$\begin{aligned}\langle M_f(k,\varepsilon)|\bar{q}_f\gamma_\mu(1-\gamma_5)q_i|M_i(P)\rangle &= \varepsilon^{*\nu\alpha}P_\alpha[G_{A_1}g_{\mu\nu} + G_{A_2}P_\nu(P+k)_\mu + \\ &\quad G_{A_3}P_\nu(P-k)_\mu + iG_V\epsilon_{\mu\nu\rho\sigma}(P+k)^\rho(P-k)^\sigma].\end{aligned} \tag{1.10}$$

These general forms are valid for meson decays of the form $M_i \to M_f\ell\nu$. Similar forms can also be written for semileptonic decays with two mesons in the final state, such as $K \to \pi\pi\ell\nu$, or for baryon semileptonic decays.

One general result is that terms of the form $(P-k)_\mu$, when contracted with the lepton current, are multiplied by the mass of the lepton. As a result, when the lepton mass is much less than the total q^2 available for the decay, these terms can be neglected. This result comes from $\bar{u}_\ell\gamma^\mu(1-\gamma_5)v_\nu(p_\ell+p_\nu)_\mu = \bar{u}_\ell(1-\gamma_5)v_\nu(m_\ell+m_\nu)$ where the Dirac equation $\bar{u}(\gamma^\mu p_\mu - m) = 0$ has been used.

Because the matrix element factorizes in semileptonic decays, the theoretical description of the decay is simpler than that of hadronic decays. Since the leptonic part of the decay is well understood, that leaves measuring H^μ and $|V_{q'q}|$ as the experimental goal in semileptonic decays. In effect, the leptonic current is used to probe the structure of the hadronic current. One approach is to measure the absolute rate of a decay, which when combined with a phenomenological description of the form factors, gives the value of $|V_{q'q}|$. The other approach is to measure H_μ using the kinematic distributions of the decay, which is the subject of this thesis.

Semileptonic decays have been extensively studied in numerous decay modes, and used to measure a number of the CKM matrix elements [3]. These measurements depend on a theoretical description of the form factors. In order to reduce the theoretical uncertainty, theorists have made use of approximate symmetries in calculating

the form factors, with symmetry breaking effects included in the calculations. Measurements of nuclear beta decay have been used to measure $|V_{ud}|$. In this case isospin symmetry is used in the calculation of the nuclear form factor [15]. Table 1.1 gives the measured values of CKM matrix elements measured in semileptonic decays.

The matrix element $|V_{us}|$ has been measured using the decay $K \to \pi\ell\nu$. The form factors $f_{\pm}$ are calculated using chiral perturbation theory which is based on the chiral symmetry which holds in the limit that the u, d and s quark masses are equal. The theoretical uncertainty is reduced even further because of the Ademollo-Gatto theorem [16] which states that the symmetry breaking corrections only occur at second order for $f_+(q^2 = 0)$.

The decay $D \to K\ell\nu$ is used to measure $|V_{cs}|$. This decay involves the transition from a heavy to a light quark, and there is not any symmetry to reduce the theoretical uncertainty in the form factors. As a result, theorists rely entirely on form factor models, and the difference between the model predictions is used as a measure of the theoretical uncertainty. The unitarity of the CKM matrix, with the assumption of 3 quark generations, provides a significantly better constraint on $|V_{cs}|$ than the measured value, and is constrained to be between 0.9736 and 0.9750 at the 90% C.L. [3].

The CKM element $|V_{cb}|$ has been measured most precisely in the decay $\bar{B} \to D^*\ell^-\bar{\nu}$. Again, the theoretical knowledge of the form factors is enhanced by the symmetry exploited in Heavy Quark Effective Theory. This symmetry is based on the b and c quarks being significantly more massive than the meson energy scale of $\Lambda_{QCD} \approx 200MeV$. There is also a result, known as Luke's theorem [17], that the symmetry breaking corrections only contribute at second order at maximum q^2. HQET is discussed in greater detail in section 2.2.

Measurements of the decay rates of $B \to \pi\ell\nu$ and $B \to \rho\ell\nu$ provide a measurement of the CKM element V_{ub}. Again this is a heavy quark to light quark transition and there is not any symmetry to exploit for calculating the form factors. As a result, there is a large uncertainty on the measurement due to model dependence.

By measuring the kinematic distribution across phase space for the decay, the

CKM Element	Measured with	Symmetry Used
$V_{ud} = 0.9736 \pm 0.0010$	Nuclear Beta Decay	isospin $m_u = m_d$
$V_{us} = 0.2196 \pm 0.0023$	$K \to \pi\ell\nu$	$SU(3)$ $m_u = m_d = m_s$
$V_{cs} = 1.01 \pm 0.18$	$D \to K\ell\nu$	No symmetry
$V_{cb} = 0.0391 \pm 0.0030$	$\bar{B} \to D^*\ell^-\bar{\nu}$	HQET $m_b, m_c >> \Lambda_{QCD}$
$V_{ub} = 0.0033 \pm 0.0008$	$B \to \pi(\rho)\ell\nu$	No symmetry

Table 1.1: CKM matrix elements measured in exclusive semileptonic decays. The values shown are taken from [3] and [18].

relative form factor sizes and the form factor shapes are measured. To measure the absolute form factor value requires measuring the absolute rate and knowing the CKM matrix element.

The form factors in $K \to \pi\ell\nu$ are parametrized as [3]

$$f_\pm = f_\pm(0)[1 + \lambda_\pm \frac{q^2}{m_\pi^2}]. \tag{1.11}$$

Since the term multiplying the f_- form factor depends on m_ℓ, decays into electrons are not sensitive to this form factor, and just the slope λ_+ is measured. Decays to muons also measure the ratio $\xi(0) = f_-(0)/f_+(0)$, with λ_- set to 0. The parameters have been measured in both charged and neutral kaon decays, and the results are given in Table 1.2 [3].

	λ_+	$f_-(0)/f_+(0)$
$K^\pm_{e3}$	0.0286 $\pm$ 0.0022	
$K^\pm_{\mu 3}$	0.033 $\pm$ 0.008	-0.35 $\pm$ 0.15
K^0_{e3}	0.0300 $\pm$ 0.0016	
$K^0_{\mu 3}$	0.034 $\pm$ 0.005	-0.11 $\pm$ 0.09

Table 1.2: Form factor measurements from semileptonic kaon decays.

The form factors have been measured for the decays $D^0 \to K^-\ell^+\nu$, $D^+ \to \bar{K}^0\ell^+\nu$, $D^+ \to \bar{K}^{*0}\ell^+\nu$, and $D_s \to \phi\ell^+\nu$ [5]. These results measure the value of the form factors at $q^2 = 0$, assuming a pole-mass q^2 dependence for the form factors, given

by [5]

$$F(q^2) = \frac{F(0)}{(1 - \frac{q^2}{m^2_{pole}})^n}, \tag{1.12}$$

where m^2_{pole} is the mass of the lowest lying (cs) meson with the correct quantum numbers. For the decay $D \to K\ell\nu$, only the pole mass for the the f_+ form factor is measured, since the f_- form factor is multiplied by the lepton mass and doesn't significantly contribute to the decay. For $D \to K^*\ell\nu$, the kinematic decay distribution is fit to extract two ratios of form factors at $q^2 = 0$. These ratios are defined as

$$\begin{aligned} r_V(0) &= \frac{F_V(0)}{F_{A_1}(0)}, \\ r_2(0) &= \frac{F_{A_2}(0)}{F_{A_1}(0)}. \end{aligned} \tag{1.13}$$

The q^2 dependence of the form factors is assumed to be a pole mass form. The technique developed for the first measurement of these ratios [19] is the method used for this thesis. Since $|V_{cs}|$ is known from the unitarity of the CKM matrix, measuring the branching ratio gives the absolute values of the form factors. The world average results [20] are given in Table 1.3.

	Experimental Average
r_V	1.85 ± 0.12
r_{A_1}	0.72 ± 0.09
$F_{A_1}(0)$	0.58 ± 0.03
$F_V(0)$	1.07 ± 0.09
$F_{A_2}(0)$	0.41 ± 0.05

Table 1.3: Form factor measurements from semileptonic D and D^* decays, evaluated at $q^2 = 0$.

Chapter 2 Theory of $\bar{B} \to D^* \ell^- \bar{\nu}$ Decay

2.1 Description of $\bar{B} \to D^* \ell^- \bar{\nu}$ Decay

The decay $\bar{B} \to D^* \ell^- \bar{\nu}$ is a semileptonic spectator decay as illustrated in Figure 1.6a. This decay has been described in detail by several authors [21, 22, 23]. Here we give some of the elements of the derivation, with a detailed derivation of the decay given in Appendix A.

2.1.1 Decay Amplitude

The decay rate is given by

$$d\Gamma = \frac{1}{2m_B}|A|^2 d\Phi_4, \tag{2.1}$$

where $|A|^2$ is the matrix element squared and Φ_4 is four body phase space for the final state $D^0 \pi \ell^- \nu$, since we include the decay $D^* \to D\pi$ in our description of the decay.

The amplitude for the decay is

$$A = i\frac{G_F}{\sqrt{2}} V_{cb} L^\mu H_\mu \tag{2.2}$$

where L^μ and H_μ are the leptonic and hadronic currents. The $V-A$ leptonic current has been given in Equation 1.6.

The hadronic current is written using the available four vectors and form factors as discussed in section 1.7. We write the vector and axial vector contributions to the current separately as

$$\begin{aligned} \langle D^*(k,\varepsilon)|V_\mu|\bar{B}(P)\rangle &= i\frac{V(q^2)}{m_B + m_{D^*}} \epsilon_{\mu\nu\rho\sigma} \varepsilon^{*\nu} (P+k)^\rho (P-k)^\sigma, \\ \langle D^*(k,\varepsilon)|A_\mu|\bar{B}(P)\rangle &= (m_B + m_{D^*}) A_1(q^2) \varepsilon^*_\mu - \frac{A_2(q^2)}{m_B + m_{D^*}} (\varepsilon^* \cdot P)(P+k)_\mu \end{aligned} \tag{2.3}$$

$$+\frac{A_3(q^2)}{m_B+m_{D^*}}(\varepsilon^*\cdot P)(P-k)_\mu$$

where P and k are the four momenta of the B and D^*, ε is the polarization vector of the D^*, and m_B and m_{D^*} are the masses of the B and D^* mesons. $A_1(q^2)$, $A_2(q^2)$, $V(q^2)$, and $A_3(q^2)$ are the form factors which describe the strong interaction effects. In the limit of the lepton mass being zero, which is a good approximation for electrons and muons, the term $A_3(q^2)(\varepsilon^*\cdot P)(P-k)_\mu$ does not contribute and will not be considered further.

2.1.2 Helicity Form Factors

Besides using the Lorentz-invariant form factors given above, it is useful to write the decay in terms of the helicity form factors H_+, H_-, and H_0 which correspond to the three helicity states of the D^* or W. The helicity projection operators of the W, in the B rest frame and with the z axis along the D^* direction, are defined as [22]

$$\begin{aligned}
\bar{\varepsilon}_\mu(\pm) &= \frac{1}{\sqrt{2}}(0,\pm 1,-i,0)\\
\bar{\varepsilon}_\mu(0) &= \frac{1}{\sqrt{q^2}}(p,0,0,-q_0)\\
\bar{\varepsilon}_\mu(t) &= \frac{1}{\sqrt{q^2}}(q_0,0,0,-p),
\end{aligned} \tag{2.4}$$

where p and q_0 are the momentum and energy of the W. The helicity state $\bar{\varepsilon}_\mu(t)$ is the spin 0 time component of the off-shell W, which only contributes when the spin of the lepton has been flipped. This helicity state does not contribute in the limit of massless leptons, which is a good approximation for electrons and muons, but is important for decays to a τ lepton.

The D^* has three helicity states which are given in the B rest frame by

$$\begin{aligned}
\varepsilon_\mu(\pm) &= \mp\frac{1}{\sqrt{2}}(0,1,\pm i,0)\\
\varepsilon_\mu(0) &= \frac{1}{m_{D^*}}(p,0,0,E_{D^*}).
\end{aligned} \tag{2.5}$$

The helicity form factors can be directly related to the Lorentz invariant form factors given above by $H_m = \varepsilon^{*\mu}(m)\langle D^*(k,\varepsilon)|J_\mu|\bar{B}(P)\rangle$. This projection gives

$$\begin{aligned}
H_\pm(q^2) &= (m_B + m_{D^*})A_1(q^2) \mp 2m_B P_{D^*}\frac{V(q^2)}{m_B + m_{D^*}} \\
H_0(q^2) &= \frac{1}{2m_{D^*}\sqrt{q^2}}[(m_B^2 - m_{D^*}^2 - q^2)(m_B + m_{D^*})A_1(q^2) - 4m_B^2 P_{D^*}^2\frac{A_2(q^2)}{m_B + m_{D^*}}] \\
H_t(q^2) &= \frac{m_B P_{D^*}}{m_{D^*}\sqrt{q^2}}[(m_B + m_{D^*})A_1(q^2) + \\
&\quad (m_B^2 - m_{D^*}^2)\frac{A_2(q^2)}{m_B + m_{D^*}} + q^2\frac{A_3(q^2)}{m_B + m_{D^*}}].
\end{aligned} \tag{2.6}$$

P_{D^*} is the momentum of the D^* in the B rest frame and is given by

$$P_{D^*} = \frac{1}{2m_B}[(m_B^2 - m_{D^*}^2 - q^2)^2 - 4m_{D^*}^2 q^2]^{1/2}. \tag{2.7}$$

2.1.3 Decay Kinematics

The four body final state $D^0\pi\ell^-\nu$ can be described using four kinematic variables, since the $D\pi$ come from a narrow D^*. We use a set of variables that are natural for the helicity formalism, which are

1. $q^2 = (p_\ell + p_\nu)^2$, the invariant mass squared of the $\ell\nu$ system;
2. $\cos\theta_\ell$, which is the angle of the lepton in the W rest frame with respect to the direction of the W in the B rest frame;
3. $\cos\theta^*$, which is the angle of the D in the D^* rest frame with respect to the direction of the D^* in the B rest frame and;
4. χ, which is the angle between the $D\pi$ and $\ell\nu$ decay planes.

These variables are illustrated in Figure 2.1.

2.1.4 Decay Distribution

The decay amplitude can be written in terms of the helicity form factors and the kinematic variables discussed in the previous sections. Because the B is a spin-zero

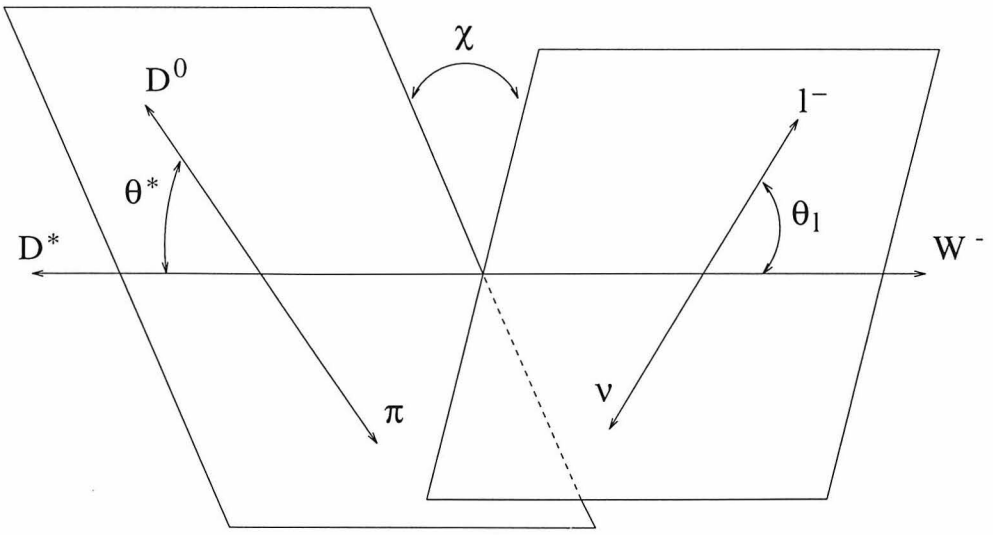


Figure 2.1: Illustration of angles for the decay in the B rest frame.

particle and the D^* and W are spin-one particles, the D^* and W are constrained to have the same helicity. We write the decay amplitude as the sum over the three helicity states of the D^*,

$$A \propto \sum_{\lambda_{D^*}} H_{\lambda_{D^*}} d^1_{\lambda_{D^*},0}(\theta^*) d^1_{\lambda_{D^*},-1}(\theta_\ell) e^{i\lambda_{D^*}(\pi-\chi)}, \tag{2.8}$$

where the d-functions, given in Appendix A, give the angular distributions associated with each helicity state.

After squaring the amplitude and writing out four body phase space for Equation 2.1, the full differential decay rate written in the helicity basis is

$$\begin{aligned}\frac{d\Gamma}{dq^2 d\cos\theta_\ell d\cos\theta^* d\chi} = \frac{3G_F^2|V_{cb}|^2 P_{D^*} q^2 \mathcal{B}(D^* \to D\pi)}{8(4\pi)^4 m_B^2} [&(1-\cos\theta_\ell)^2(\sin^2\theta^*)|H_+|^2 \\ &+(1+\cos\theta_\ell)^2(\sin^2\theta^*)|H_-|^2 + 4\sin^2\theta_\ell\cos^2\theta^*|H_0|^2 \\ &-2(\sin^2\theta_\ell)(\sin^2\theta^*\cos 2\chi)H_+H_- \\ &-4\sin\theta_\ell(1-\cos\theta_\ell)(\sin\theta^*\cos\theta^*\cos\chi)H_+H_0 \\ &+4\sin\theta_\ell(1+\cos\theta_\ell)(\sin\theta^*\cos\theta^*\cos\chi)H_-H_0].\end{aligned} \tag{2.9}$$

Figures 2.2 and 2.3 show the differential decay distribution in one and two-dimensional

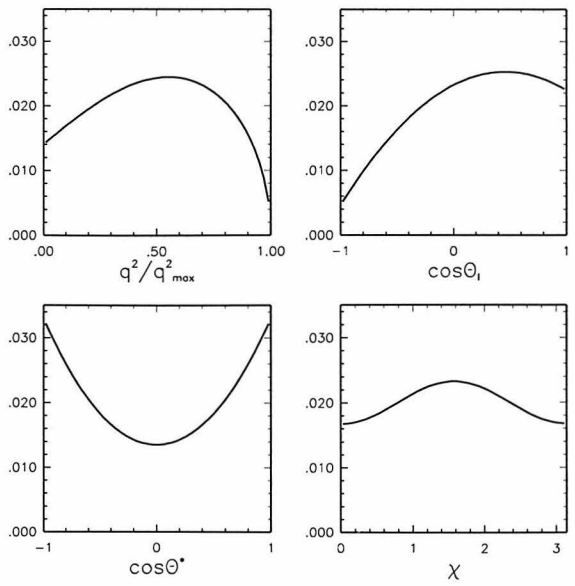


Figure 2.2: Projection of the differential decay distribution in each of the four kinematic variables.

projections of the kinematic variables, using the form factor parametrizations given in Equations 2.24, 2.27 and 2.28 below, and the results measured in this thesis.

The cross terms do not contribute to the total rate, after integrating over the angle χ. Nonetheless, the distribution in that variable does depend on the relative size of the form factors. The longitudinal, (H_0), and transverse, ($H_\pm$), helicity amplitudes are separated in $\cos\theta^*$ while H_+ and H_- are separated in $\cos\theta_\ell$, and $\cos\theta_\ell$ versus χ.

Integrating over all decay angles leaves just the q^2 distribution

$$\frac{d\Gamma}{dq^2} = \frac{G_F^2 |V_{cb}|^2 \, P_{D^*} \, q^2}{96\pi^3 {m_B}^2}(|H_+(q^2)|^2 + |H_-(q^2)|^2 + |H_0(q^2)|^2), \tag{2.10}$$

where q^2 ranges from $q^2_{min} = m_\ell^2 \approx 0$ GeV/c^2 to $q^2_{max} = (m_B - m_{D^*})^2 \approx 10.7$ GeV/c^2. In Figure 2.4 we plot $\frac{d\Gamma}{dq^2}$ and the contribution of the different helicity amplitudes. At q^2_{min}, only the H_0 helicity amplitude contributes. This can be understood from simple helicity arguments [5] as illustrated in Figure 2.5. q^2_{min} corresponds to maximum D^* momentum, where the D^* is recoiling against the lepton and neutrino. The lepton and neutrino helicities combine to give a helicity zero state for the W, which forces the D^* to be in its helicity zero state. At q^2_{max}, the D^* is produced at rest, in the

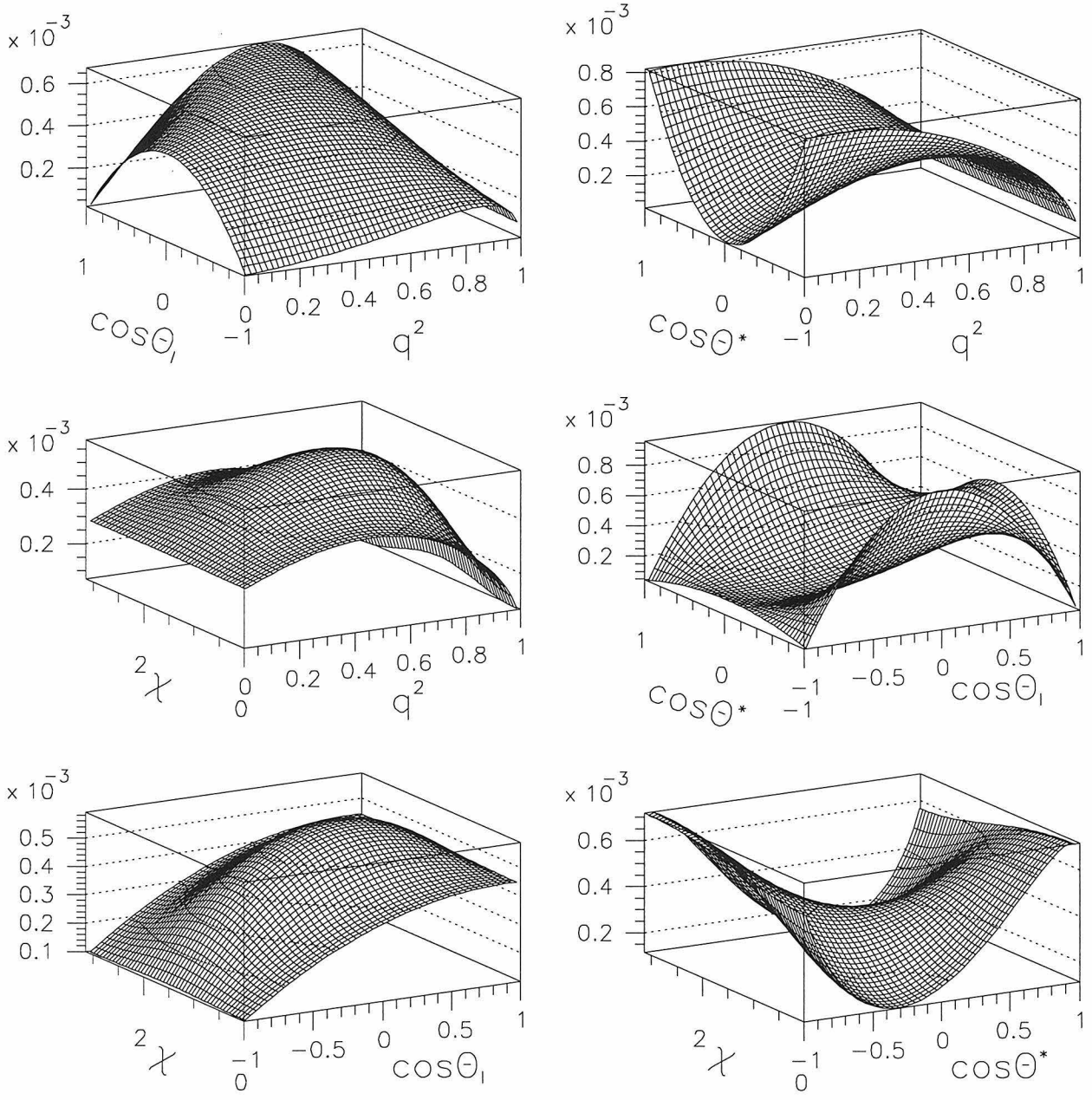


Figure 2.3: The differential decay distribution in two dimensions, for all of the four kinematic variables. The normalization is arbitrary.

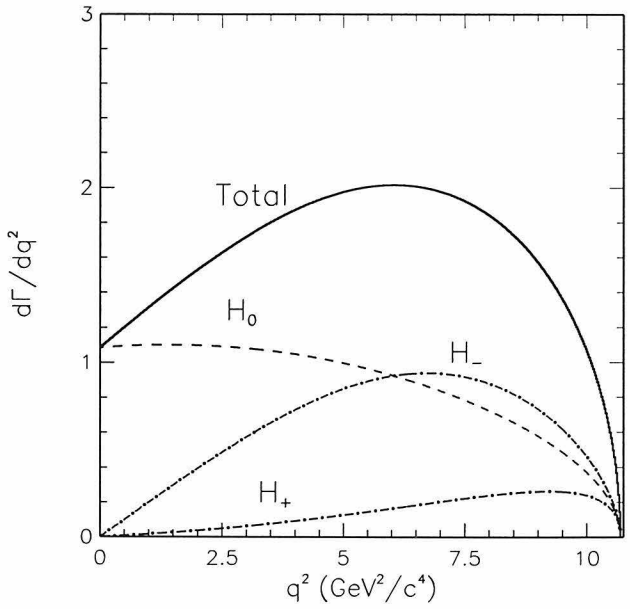


Figure 2.4: Differential q^2 distribution and the contribution of the different helicity amplitudes.

B rest frame, and its helicity state is undefined so all three states contribute equally. The total rate goes to zero at this point because phase space, which is proportional to P_{D^*}, becomes zero.

The transverse (Γ_T) and longitudinal (Γ_L) decay widths are defined by

$$\Gamma_L = \Gamma_0; \quad \Gamma_T = \Gamma_+ + \Gamma_-$$
$$\Gamma_i = (G_F^2 |V_{cb}|^2 / 96\pi^3) \int dq^2 P_{D^*}(q^2/{m_B}^2) |H_i(q^2)|^2. \tag{2.11}$$

2.1.5 Decay Asymmetries

When a b quark decays by emitting a virtual W, the c quark is most often produced with a negative (or left-handed) helicity. This is a result of the $(1-\gamma_5)$ nature of the weak interaction. The spectator quark in the decay is just as likely to have a right or left handed helicity. Combining the left handed c quark spin with the spectator quark spin will produce a D^* with a helicity state of H_- or H_0. If the c quark is produced with a right handed helicity, then the D^* helicity will be either H_+ or H_0. This way information about the spin of the produced c quark is preserved in the D^* helicity. In contrast, for the decay $\bar{B} \to D\ell^-\bar{\nu}$, the D meson is always in a spin zero

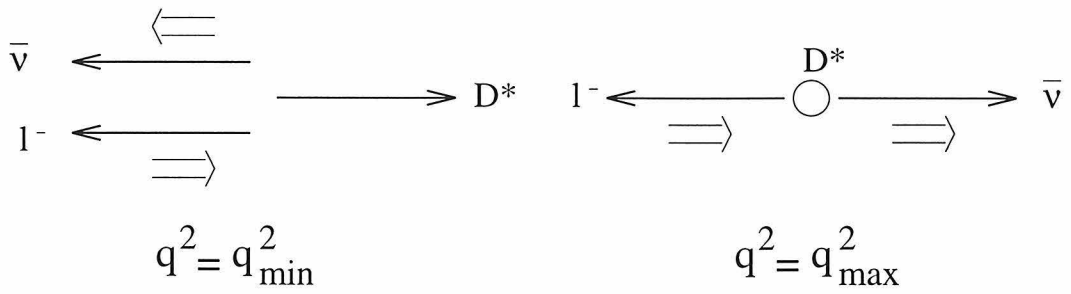


Figure 2.5: At $q^2 = q^2_{min}$, the lepton and neutrino are parallel giving a helicity zero state. At $q^2 = q^2_{max}$, the D^* is produced at rest and its helicity is not defined.

state, and the c quark spin information is not preserved.

If the b quark decay is due to the weak interaction, the predominance of a left handed helicity for the c quark will result in $H_- > H_+$ for the D^* helicity. This results in two parity violating terms in the differential decay rate. The difference in H_+ and H_- is determined by the size of the vector form factor, as seen in Equation 2.6. If the decay distribution given in Equation 2.9 is rewritten so that terms with H_+ and H_- are grouped together, the two parity violating terms are

$$\begin{aligned} &+2\cos\theta_\ell \sin^2\theta^*(|H_-|^2 - |H_+|^2), \\ &+4\sin\theta_\ell \sin\theta^* \cos\theta^* \cos\chi(H_- - H_+)H_0. \end{aligned} \tag{2.12}$$

The first term leads to an asymmetry in the decay distribution of $\cos\theta_\ell$ as is evident in Figure 2.2. The asymmetry does not show up in $\cos\theta^*$ because the D^* decays to 2 scalars and so the angular distribution for H_- and H_+ helicities are the same. However, that is not the case for the decay into leptons of the W, which carries the same helicity as the D^*.

The semileptonic decay of a c quark also tends to produce a left handed helicity

quark state, over a right handed helicity state. However, the emitted W^+ decays to a right handed anti-lepton and left handed neutrino. As a result, the $\cos\theta_\ell$ terms change sign and the decay asymmetry is opposite. This leads to leptons being more often produced in the backward direction, and a softer lepton spectrum for c decays than for b's. In the decay of a $\bar{b}$ quark, a W^+ also produces a right handed anti-lepton leading to a change in the sign for $\cos\theta_\ell$ terms. However, the weak current tends to produce right handed anti-quarks, which results in $H_+ > H_-$ at the meson level. This introduces another sign change, leaving the lepton angular distribution the same as for the b quark decay. Specifically, one must exchange $H_+ \leftrightarrow H_-$ when comparing b and $\bar{b}$ decays. This is because the complex conjugation of the hadronic current in Equation 2.3 changes the sign in front of the vector form factor. Section A.3 further discusses the difference between particle and anti-particle form factors.

A second asymmetry, shown in the second term, is evident in the two-dimensional distribution of $\cos\theta^*$ and χ. Figure 2.3 illustrates this asymmetry. This term doesn't contribute to the total rate after integrating over χ. However, this asymmetry is easily observed in the data as shown in Figure 8.3.

Korner and Schuler [24] define these two parity violating asymmetries as

$$a_{FB} = \frac{d\Gamma(\theta_\ell) - d\Gamma(\pi - \theta_\ell)}{d\Gamma(\theta_\ell) + d\Gamma(\pi - \theta_\ell)}, \quad \frac{\pi}{2} \geq \theta_\ell \leq \pi, \tag{2.13}$$

$$a_A = \frac{d\Gamma(\theta^*, \chi) - d\Gamma(\theta^*, \pi + \chi) - d\Gamma(\pi - \theta^*, \chi) + d\Gamma(\pi - \theta^*, \pi + \chi)}{d\Gamma(\theta^*, \chi) + d\Gamma(\theta^*, \pi + \chi) + d\Gamma(\pi - \theta^*, \chi) + d\Gamma(\pi - \theta^*, \pi + \chi)},$$
$$0 \leq \theta^* \leq \frac{\pi}{2}, \quad -\frac{\pi}{2} \leq \chi \leq \frac{\pi}{2}. \tag{2.14}$$

The angles not used in the asymetries have been integrated over their entire range. Integrating over q^2 gives the integrated asymmetries [25]:

$$A_{FB} = \frac{3}{4}\frac{\int(|H_-|^2 - |H_+|^2)P_{D^*}q^2dq^2}{\int(|H_-|^2 + |H_+|^2 + |H_0|^2)P_{D^*}q^2dq^2} = \frac{3}{4}\frac{(\Gamma_- - \Gamma_+)}{(\Gamma_0 + \Gamma_+ + \Gamma_-)}, \tag{2.15}$$

$$A_A = \frac{3}{4}\frac{\int(H_- - H_+)H_0 P_{D^*} q^2 dq^2}{\int(|H_-|^2 + |H_+|^2 + |H_0|^2)P_{D^*} q^2 dq^2}, \tag{2.16}$$

There is a third asymmetry given in [26], which describes the D^* polarization. This integrated asymmetry is defined as

$$A_{pol} = \frac{2\int |H_0|^2 P_{D^*} q^2 dq^2}{\int(|H_-|^2 + |H_+|^2)P_{D^*} q^2 dq^2} - 1 = 2\frac{\Gamma_0}{\Gamma_+ + \Gamma_-} - 1. \tag{2.17}$$

The asymmetries measured in the data are discussed in section 8.3.

2.2 Heavy Quark Effective Theory

In order to actually calculate the decay rate, one needs to know the normalization and q^2 dependence of the form factors. The form factors describe the QCD effects in the decay, and are a measure of the difference between the decay of a free quark and a quark bound inside a meson. However, it is not known how to calculate the form factors directly since they involve non-perturbative QCD effects.

A meson with one heavy and one light quark has a size on the order of 1 fm, which corresponds to an energy scale $\Lambda_{QCD} \approx 200$MeV. The meson can be thought of as a heavy quark surrounded by the light quark plus gluons which constitute the light degrees of freedom. In the case where the heavy quark mass is much larger than the energy scale of the light degrees of freedom ($m_Q >> \Lambda_{QCD}$), many of the meson properties are basically independent of the spin and flavor of the heavy quark, which behaves like a static color charge. This is analagous to the atomic spectra of an atom being mostly independent of the nuclear spin and structure. In a sense the light degrees of freedom are not energetic enough to probe the properties of the heavy quark at the center of the meson [26].

In the limit where the masses of b and c quarks are infinite, the light degrees of freedom are independent of the heavy quark spin and flavor. This gives a $SU(2N_f)$ heavy quark symmetry (HQS) for 2 spins and N_f heavy flavors. This symmetry provides the basis for Heavy Quark Effective Theory (HQET) [27, 28, 26]. Since

b and c quarks do not have infinite mass, HQET uses an expansion in $1/m_Q$ to calculate corrections to the symmetry limit. With HQET, one can relate the $B^* - B$ mass splitting to that for $D^* - D$, as well as other "spectroscopic" relations between bottom and charm mesons. Most importantly for our subject, HQET relates the form factors in $\bar{B} \to D^* \ell^- \bar{\nu}$ to each other as well as to the form factors in $\bar{B} \to D \ell^- \bar{\nu}$.

In the infinite mass limit, the appropriate kinematic variables are the four velocities, v and v', of the initial and final state mesons. The hadronic matrix element for the $B \to D^*$ transition is then written as [26]

$$\begin{aligned} \langle D^*(v',\varepsilon)|V_\mu|\bar{B}(v)\rangle &= i h_V(w)\epsilon_{\mu\nu\rho\sigma}\varepsilon^{*\nu}v'^{\rho}v^{\sigma}, \\ \langle D^*(v',\varepsilon)|A_\mu|\bar{B}(v)\rangle &= h_{A_1}(w)(w+1)\varepsilon^*_\mu - [h_{A_2}(w)v_\mu + h_{A_3}(w)v'_\mu]\varepsilon^*\cdot v. \end{aligned} \tag{2.18}$$

The form factors h are functions of $w \equiv v \cdot v'$ which is just the relativistic factor $\gamma = \frac{E_{D^*}}{m_{D^*}}$ of the D^* in the B rest frame. This is related to q^2 by $w = (m_B^2 + m_{D^*}^2 - q^2)/(2m_B m_{D^*})$, where $w = 1$ at $q^2_{max} = (m_B - m_{D^*})^2$ and $w \approx 1.5$ at $q^2_{min} = m_\ell^2 \approx 0$.

In the symmetry limit, all of the form factors are related by

$$h_V(w) = h_{A_1}(w) = h_{A_3}(w) = \xi(w); \quad h_{A_2}(w) = 0. \tag{2.19}$$

The function $\xi(w)$ is referred to as the Isgur-Wise function, and also describes the form factors for the $B \to D$ matrix element. HQS also predicts the normalization of this function as $\xi(w = 1) = 1$. This can be understood as the wavefunctions for the b and c quarks being identical when the c quark is produced at rest.

The masses of the heavy quarks are not infinite and these symmetry relations are broken. HQET is used to calculate the corrections to the theory as an expansion in $1/m_Q$. However, these corrections reintroduce some model dependence. Perturbative hard gluon corrections also change the symmetry relations, and have been calculated to sub-leading order for the form factors. One other important result, known as Luke's Theorem, is that the first order $1/m_Q$ corrections vanish for the h_{A_1} form factor at $w = 1$ [17]. Since this form factor determines the overall rate at zero recoil,

measuring the decay rate at that point gives a value for V_{cb} with a small theoretical uncertainty. This is now a commonly used method to measure V_{cb}.

The HQET form factors are directly related to the conventional form factors given in Equation 2.3 by [26]

$$\begin{aligned} R^* V(q^2) &= h_V(w) \\ R^{*-1} A_1(q^2) &= \frac{w+1}{2} h_{A_1}(w) \\ R^* A_2(q^2) &= h_{A_3}(w) + \frac{m_{D^*}}{m_B} h_{A_2}(w), \end{aligned} \tag{2.20}$$

where $R^* = \frac{2\sqrt{m_B m_{D^*}}}{m_B + m_{D^*}} \approx 0.89$. In the symmetry limit, the conventional form factors are related to the Isgur-Wise function by

$$\frac{m_B + m_{D^*}}{2\sqrt{m_B m_{D^*}}} \xi(w) = V(q^2) = A_2(q^2) = [1 - \frac{q^2}{(m_B + m_{D^*})^2}]^{-1} A_1(q^2). \tag{2.21}$$

HQET does not give a prediction for the dynamical w dependence of the form factors. However, we can write the function $\xi(w)$ as a series expansion [26]

$$\xi(w) = 1 - \rho^2(w-1) + \mathcal{O}[(w-1)^2]. \tag{2.22}$$

The function is defined with the slope parameter $\rho^2 > 0$ so that $\xi'(1) = -\rho^2$. We use a linear form for the function by just keeping the first term in the expansion. Other forms for the w dependence which have also been suggested are [26]

$$\begin{aligned} \xi(w) &= \exp[-\rho^2(w-1)], \\ \xi(w) &= \frac{2}{w+1} \exp[(1-2\rho^2)\frac{w-1}{w+1}], \\ \xi(w) &= (\frac{2}{w+1})^{2\rho^2}. \end{aligned} \tag{2.23}$$

Figure 2.6 plots the different forms for $\xi(w)$ over the w range in $\bar{B} \to D^* \ell^- \bar{\nu}$. As shown, there is not a significant difference between the forms over this limited w range. For the w range in $b \to u$ transitions, the difference between form factor

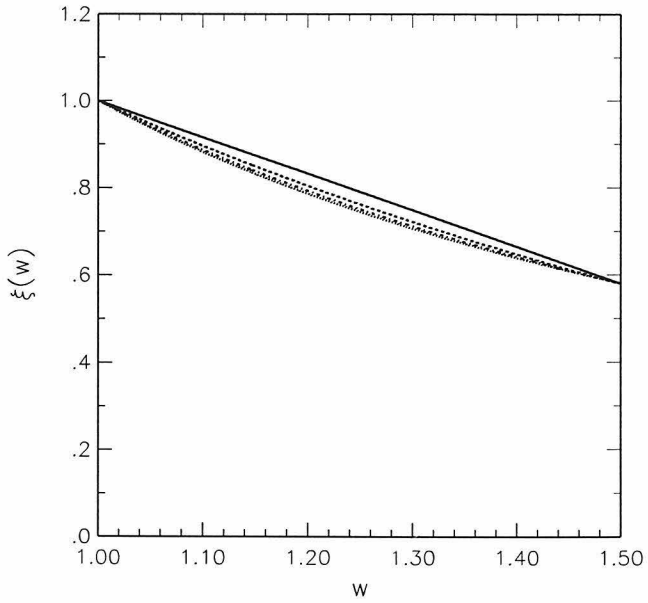


Figure 2.6: Plot of $\xi(w)$ for the forms given in equations 2.22 and 2.23. The values of ρ^2 used are those obtained from the fit to the data as given in Table 6.3.

models is more significant.

The function $\xi(w)$ is actually the universal form factor in the symmetry limit. However, what is measured are the physical form factors which have the symmetry breaking effects. We characterize the overall q^2 dependence with the function

$$h_{A_1}(w) = h_{A_1}(1)[1 - \rho^2_{A_1}(w-1) + \mathcal{O}[(w-1)^2]], \tag{2.24}$$

where $\rho^2_{A_1}$ is the physical form factor slope.

The form factor slope is not predicted, but bounds have been placed on its value using QCD sum rules. The Bjorken sum rule [29] relates the probability for a free quark semileptonic decay, to the sum of the probabilities for decays to exclusive semileptonic final states, in the infinite mass limit. This gives the relation [26]

$$\begin{aligned} 1 \;=\; & \frac{w+1}{2}|\xi(w)|^2 + \sum_l |\xi^{(l)}(w)|^2 \\ & +(w-1)2\sum_m |\tau^{(m)}_{1/2}(w)|^2 + (w+1)^2 \sum_n |\tau^{(n)}_{3/2}(w)|^2 \\ & +\mathcal{O}[(w-1)^2]. \end{aligned} \tag{2.25}$$

The states are denoted by the quantum numbers of the light degrees of freedom, $1/2^+$ and $3/2^+$, and the sums over l, m, and n are for the radial excitations. Expanding $\xi(w)$ and just keeping terms that contribute to first order in $(w-1)$ gives the relation

$$\rho^2 = \frac{1}{4} + \sum_m |\tau_{1/2}^{(m)}(w)|^2 + 2\sum_n |\tau_{3/2}^{(n)}(w)|^2 > \frac{1}{4}. \tag{2.26}$$

A recent paper finds $\tau(1) = 0.55 \pm 0.05$ using an HQET analysis of the decay $B \to D_1 \ell\nu$ and the measured branching ratio. This leads to the lower bound $\rho^2 > 0.25 + \tau^2(1) = 0.55$ [30]. There is a similar Voloshin sum rule [31] that gives an upper bound of $\rho^2 < 0.75$. However, these sum rule bounds are modified by α_s and $\Lambda_{QCD}/m_{c,b}$ corrections, with the Voloshin bound loosening the most. Sum rules, with corrections, have been calculated for the h_{A_1} form factor and the bounds are $0.4 < \rho_{A_1}^2 < 1.3$ [32].

2.3 Ratios of Form Factors

Equation 2.6 shows that all helicity states depend on the form factor $A_1(q^2)$. This form factor can be factored out in front and the helicity form factors can be written in terms of the ratio of form factors R_1 and R_2 where

$$R_1 = \left[1 - \frac{q^2}{(m_B + m_{D^*})^2}\right] \frac{V(q^2)}{A_1(q^2)} = \frac{h_V(w)}{h_{A_1}(w)} \tag{2.27}$$

$$R_2 = \left[1 - \frac{q^2}{(m_B + m_{D^*})^2}\right] \frac{A_2(q^2)}{A_1(q^2)} = \frac{h_{A_3}(w) + r h_{A_2}(w)}{h_{A_1}(w)}, \tag{2.28}$$

with $r = m_{D^*}/m_B$. The q^2 dependent term in front cancels the relative q^2 dependence between A_1 and the other form factors that is predicted by HQET. In the full symmetry limit $R_1 = R_2 = 1$ but the hard gluon and $1/m_Q$ corrections lead to predictions of $R_1 \approx 1.3$ and $R_2 \approx 0.8$ [26]. These corrections also predict a small q^2 dependence with Neubert [26] predicting

$$\begin{aligned} R_1(w) &= 1.35 - 0.22(w-1) + 0.09(w-1)^2, \\ R_2(w) &= 0.79 + 0.15(w-1) - 0.04(w-1)^2. \end{aligned} \tag{2.29}$$

Close and Wambach [33] calculate

$$\begin{aligned} R_1(w) &= R_1[1 - 0.06(w-1)], \\ R_2(w) &= R_2[1 + 0.04(w-1)]. \end{aligned} \tag{2.30}$$

The deviation from 1 for R_1 is mostly due to perturbative hard gluon corrections and thus has less model dependence than R_2 which depends on assumptions about the sub-leading Isgur-Wise functions.

The relative distribution across the four-dimensional space describing the decay as given in Equation 2.9 will be determined by these ratios of form factors and the overall q^2 dependence given by $A_1(q^2)$. To obtain the absolute rate, a knowledge of $A_1(q^2_{max})$ and $|V_{cb}|$ is also needed. This analysis uses the relative distribution to measure these ratios of form factors and $\rho^2_{A_1}$, and thus does not require a knowledge of $|V_{cb}|$ or the absolute normalization of the form factors.

2.4 Form Factor Models

Before the development of HQET, the form factors for exclusive semileptonic B decay were calculated in a variety of models. Although these models have been superseded by HQET (especially for measurements of V_{cb}), HQET has not replaced them altogether. That is because HQET does not predict the form of $\xi(w)$, the expansion in $1/m_Q$ reintroduces model dependence, and the corrections to the symmetry limit have not been calculated for many semileptonic decays. As a result, models are still used for generating Monte Carlo samples of semileptonic decays. Models are even more important in $b \to u$ semileptonic decays, where HQET does not apply. Here we briefly describe some of the better known form factor models and their predictions for the Lorentz-invariant form factors $V(q^2)$, $A_1(q^2)$, and $A_2(q^2)$.

The KS model by Korner and Schuler [21] gets the normalization of the form factors at $q^2 = 0$ and uses a "pole-form" for the q^2 dependence, which assumes

nearest meson-dominance. The general form is

$$F(q^2) = F(0)\left(\frac{m_{FF}^2}{m_{FF}^2 - q^2}\right)^n \tag{2.31}$$

where $n = 1$ for A_1 and $n = 2$ for A_2 and V, and $m_{FF} = 6.34$ GeV/c^2, which is the effective B_c^* meson mass. The model by Bauer, Stech and Wirbel [34] writes the form factors in the same way as the KS model but uses $n = 1$ as the power dependence for all the form factors. They also use slightly different values for the normalization, $F(0)$, and the effective meson mass, m_{FF}, for each of the form factors.

The ISGW model [14] by Isgur, Grinstein, Scora, and Wise takes a different approach by calculating the normalization of the form factors at q_{max}^2 where the D^* is at rest. They characterize the q^2 dependence of the form factors as a falling exponential. These form factors are obtained using a non-relativistic treatment of harmonic oscillator wave functions in a potential that mocks up the non-relativistic effects of QCD. The general form for these form factors is

$$F(q^2) = F(q_{max}^2)\exp[-\alpha(q_{max}^2 - q^2)]. \tag{2.32}$$

The ISGW model calculates a value for α of 0.03.

HQET can provide important constraints on the models. For example, both the ISGW and BSW models do not predict the relative q^2 dependence between the A_1 form factor and the others as given in Equation 2.21. However, the ISGW model has been updated using the constraints of HQET to become the ISGW2 model [35]. The general form of the ISGW2 form factor is

$$F(q^2) = F(q_{max}^2)[1 + \alpha(q_{max}^2 - q^2)]^{-2}, \tag{2.33}$$

where $\alpha = 0.016$. The A_1 form factor also has the correct q^2 dependence relative to the other form factors.

The predictions of the form factors, at $q^2 = q_{max}^2$ and $q^2 = 0$, for various models and HQET with corrections are given in Table 2.1.

	$R_1(q^2_{max})$	$R_2(q^2_{max})$	$R_1(q^2_{min})$	$R_2(q^2_{min})$	$\rho^2_{A_1}$
HQET	1.35	0.79	1.27	0.85	
ISGW	1.01	0.91	1.27	1.14	0.64
ISGW2	1.27	1.02	1.27	1.02	0.68
BSW	0.91	0.85	1.09	1.06	0.72
KS	1.09	1.09	1.00	1.00	0.72

Table 2.1: Predictions of form factor ratios given by models and HQET with corrections from [26]. Here, $q^2_{max} = (m_B - m_{D^*})^2$ and $q^2_{min} = 0$.

Chapter 3 The CLEO Experiment

3.1 CESR

The Cornell Electron Storage Ring (CESR) is an e^+e^-collider operating in the center of mass (CM) energy range of 9.4 to 11.2 GeV. CESR has been in operation since 1979 and originally provided collisions for the CLEO I and CUSB detectors. Since 1990, CESR has used only one interaction region at the CLEO detector. CESR is also a source of synchroton radiation for the users of the CHESS facilities.

Figure 3.1 shows a schematic drawing of the accelerator facility. Electrons are initially accelerated in a 30 meter linac to an energy of about 150 MeV. They are then injected into the synchrotron which accelerates the particles to an energy of about 5 GeV, before being transferred to the storage ring. Positrons are created by having electrons at 140 MeV strike a tungsten target midway in the linac. The collected positrons are accelerated in the rest of the linac before injection in the synchroton.

The storage ring has a circumference of 768 meters and maintains beam energies of around 5 GeV. With the usual synchrotron radiation loss and the effect of wiggler magnets to provide radiation for CHESS, the electrons lose on average 1.2 MeV of energy per turn. The total rate of power loss due to radiation is about half a megawatt. To restore the energy there are two RF regions each containing two 5-cell accelerating cavities which operate at 500 MHz [36].

The rate of collisions is determined by the cross section, as given by nature, times the luminosity which is delivered by CESR. The luminosity is given by [37]

$$\mathcal{L} = \frac{f N_B n_1 n_2}{4A}, \tag{3.1}$$

where n_i is the number of particles in each bunch, N_B is the number of bunches and

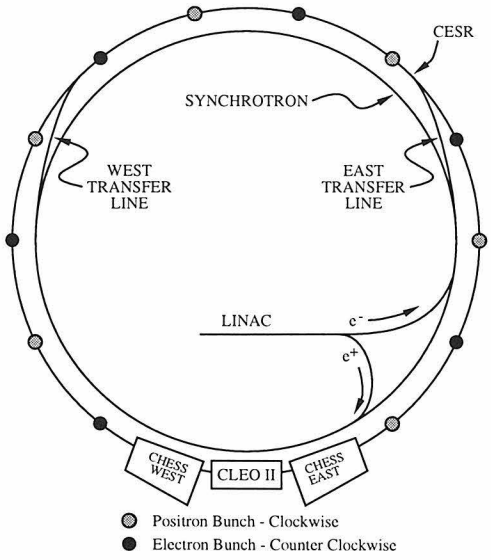


Figure 3.1: The Cornell Electron Storage Ring.

f is the frequency at which a bunch passes the collision point. A is the effective interaction area of the two colliding bunches. A bunch at CESR typically has transverse dimensions (FWHM) of 0.1 cm in the horizontal and 0.01 cm in the vertical direction. This gives an effective area $A = \frac{\pi\Gamma_x\Gamma_y}{2.35^2} = 5.7 \times 10^{-4}$ cm^2. The beam length is 4.2 cm.

During the time when the data for this analysis was taken, there were seven bunches with $\approx 3 \times 10^{11}$ particles per bunch. The crossing frequency for a bunch is 390 kHz. The peak luminosity during this time was typically $(1-2) \times 10^{32}$ cm^{-2}s^{-1}.

3.2 The CLEO Detector

We present the major features of the CLEO detector as they were during the period of data taking for this analysis. This is sometimes referred to as the CLEO-II detector. The CLEO detector has been described in detail elsewhere [38]. We give an overview of the detector and highlight the features relevant to this analysis. The following description of the detector is primarily based on [38], unless referenced otherwise.

The CLEO detector has the features of most general purpose particle detectors at e^+e^- colliders. CLEO has tracking chambers in a 1.5 T solenoidal magnetic field for momentum measurements and $\mathrm{d}E/\mathrm{d}x$ particle identification, an electromagnetic

calorimeter for photon and electron identification, a time of flight system for the trigger and particle identification, and outer muon chambers. The primary strengths of CLEO are precision tracking and photon energy measurements that cover 94% of the solid angle. Figure 3.2 illustrates the CLEO detector. Figure 3.3 shows an event display for a candidate event for the decay $B^- \to D^{*0}\ell^-\bar{\nu}$. The event display shows the r-phi view of the detector, with the barrel calorimeter opened up to display z position as well. Tracks and showers are labeled with their momenta and energy.

3.2.1 Tracking

CLEO has three tracking chambers providing a total of 71 layers of tracking. The innermost Precision Tracking Layer (PTL) is a 6 layer drift chamber. All 6 layers are axial and only provide $r - \phi$ measurements. The field shaping cages are aluminized mylar tubes which surround the gold-plated sense wires. The PTL has an inner radius of 4.5 cm and extends to 7.7 cm. Just outside the PTL is the vertex detector (VD) which is a 10 layer drift chamber. This chamber also gives z direction information. This comes from cathode strips, on the inner and outer radii, which have a segmentation of 5.85 mm (inner) and 6.85 mm (outer) in the z direction. The anode wires also have a higher resistance which allows charge division measurements. The VD extends from a radius of 7.5 to 17.5 cm. Tracks with a p_T greater than 40 MeV/c and a polar angle greater than 25° will pass through all the layers of the VD.

The main drift chamber (DR) is a 51 layer device which extends from 17.5 cm to 95 cm. There are 40 axial and 11 stereo layers. Each cell has 8 field wires arranged in a rectangular pattern, with a half-cell width of about 7 mm. There is a single hit resolution of 100 to 200 um depending on the position of the track within the cell. The single hit efficiency is around 85% for a cell. The loss of efficiency is at the edge of the cell where the electric field is weak and the large magnetic field distorts the drift path. There are also cathode strips at the inner and outer radii with a segmentation of 1 cm in the z direction. The inner radius has 8 cathodes in azimuth and the outer radius has 16. The drift gas used for all tracking devices is a mixture of 50% argon

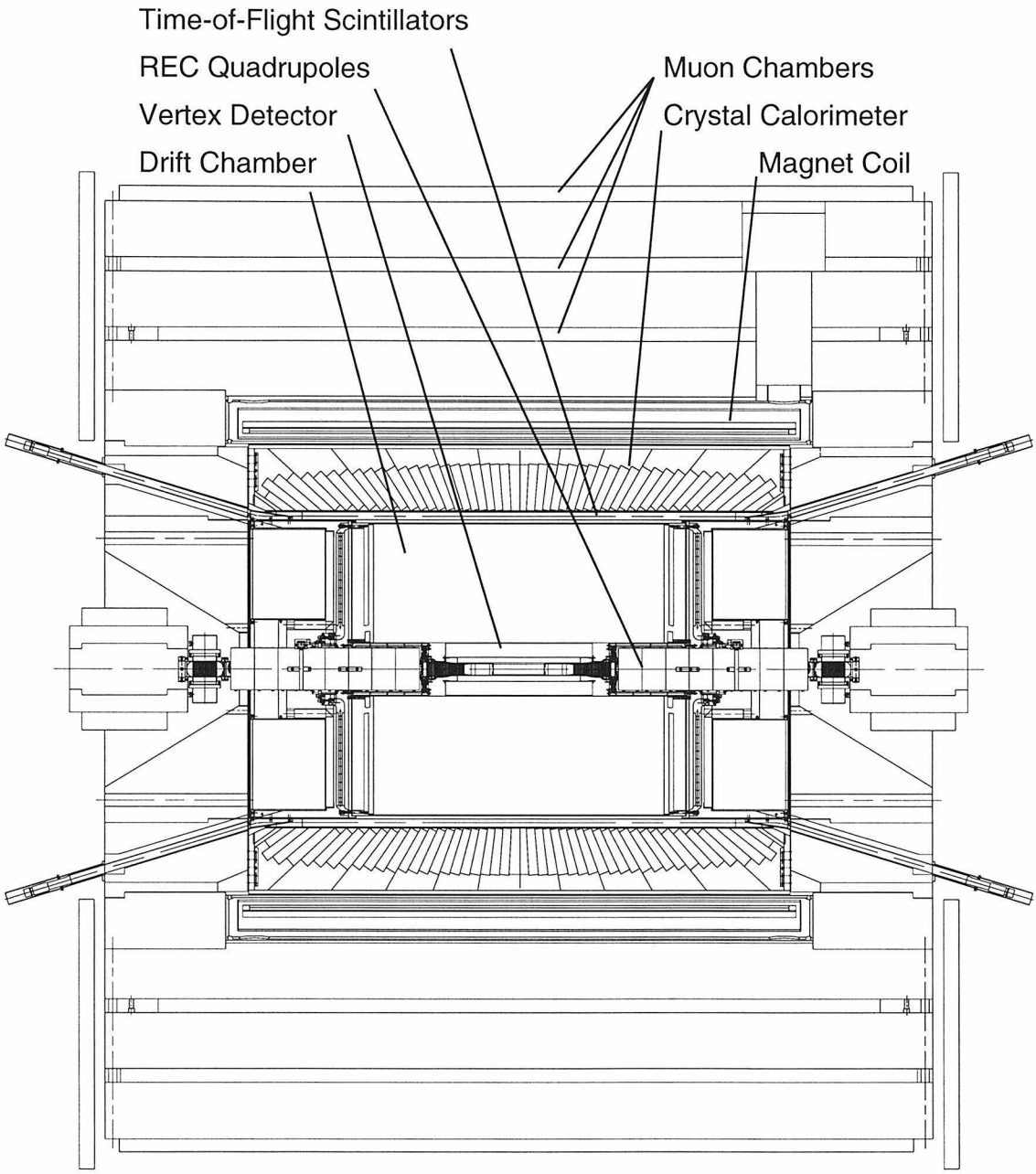


Figure 3.2: The Cleo Detector.

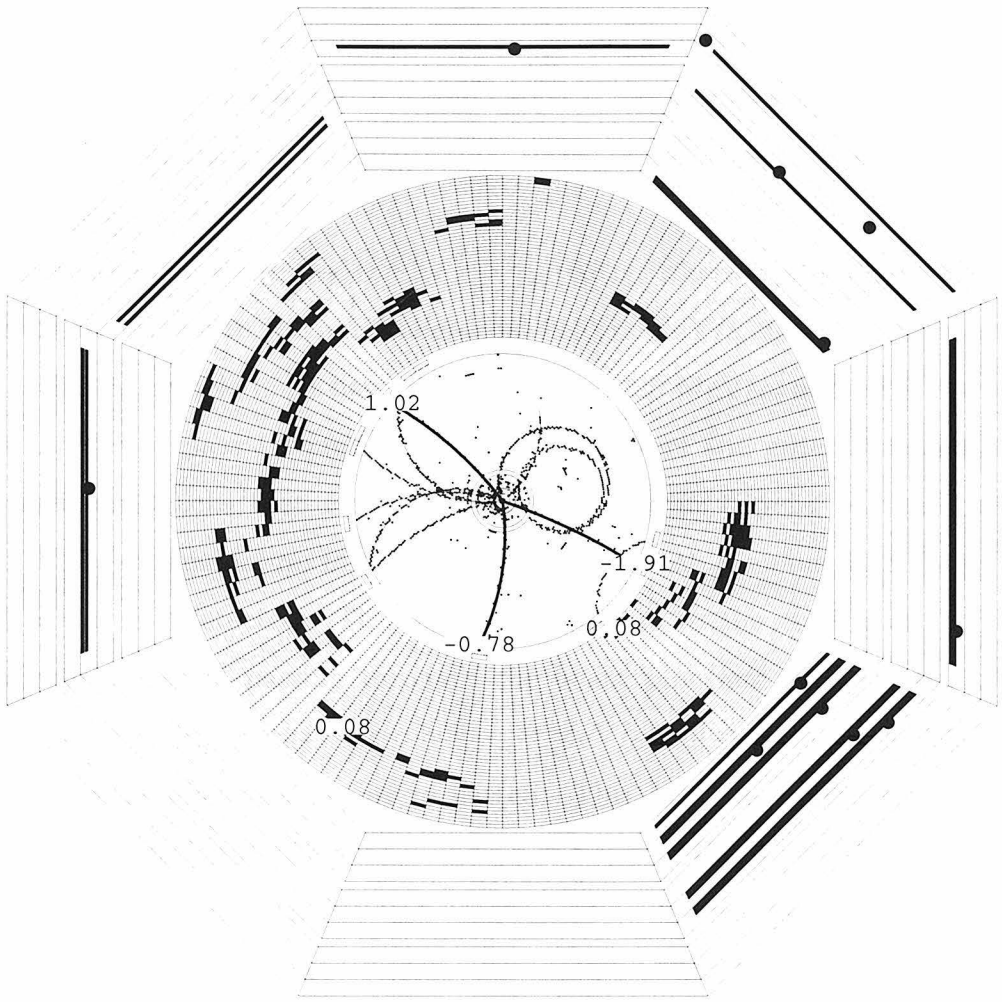


Figure 3.3: An event display for a candidate decay $B^- \to D^{*0}\mu^-\bar{\nu}_\mu$, $D^{*0} \to D^0\pi^\circ$, $D^0 \to K^-\pi^+$. The muon is well identified by hits in the muon counters. The thick lines are the candidate tracks. The two 80 MeV showers reconstruct to the π° mass.

and 50% ethane, and the same recirculation system is used for all devices.

Combining all three tracking devices, the charged particle tracking resolution is given by

$$(\frac{\delta p_t}{p_t})^2 = (0.0015 p_t)^2 + (0.005)^2, \tag{3.2}$$

where p_t is given in GeV/c. The constant term is due to multiple scattering and remains the largest contribution to the error for even the highest momentum tracks in $B\bar{B}$ events at CLEO. The measured angular resolutions, at high momentum, are $\delta\phi = 1$ mrad and $\delta\theta = 4$ mrad. The difference in the angular resolutions is due to there being a maximum of 15 longitudinal measurements as compared to 56 axial measurements.

The radius of curvature is given by $r = p_t/(0.3B)$ where r is in meters, p_t is the momentum transverse to the axial solenoidal field in GeV/c, and the magnetic field B is in tesla. A particle must have a p_t of at least 225 MeV/c, and be in the barrel region, in order to pass through all the tracking layers and enter the calorimeter. Low momentum tracks that curl up inside the detector depend primarily on the VD and PTL for momentum measurements. Tracks with a momentum of less than 50 MeV/c are not detected. This inefficiency is due to the curling of the tracks and the energy loss in passing throught the beam pipe and detector walls. The efficiency for detecting tracks is zero below 50 MeV/c and rises to above 90% at 120 MeV/c where the efficiency begins to flatten. This turn on in efficiency has been measured in the data and it agrees well with the Monte Carlo [39]. Figure 7.1 plots the detection efficiency as a function of momentum for the low momentum pions used in this analysis. The poor efficiency for reconstructing tracks below 100 MeV/c directly impacts the efficiency for reconstructing the decay $D^{*+} \rightarrow D^0\pi^+$, for which the average momentum of the pion is 110 MeV/c.

The pulse height measurements from the 51 layers of the drift chamber are used to calculate the $\mathrm{d}E/\mathrm{d}x$ energy loss of the track. Each measurement is corrected for effects such as the drift distance, entrance angle into the cell and whether it is an axial or stereo layer. The lowest 65% of the measurements are used to calculate a truncated

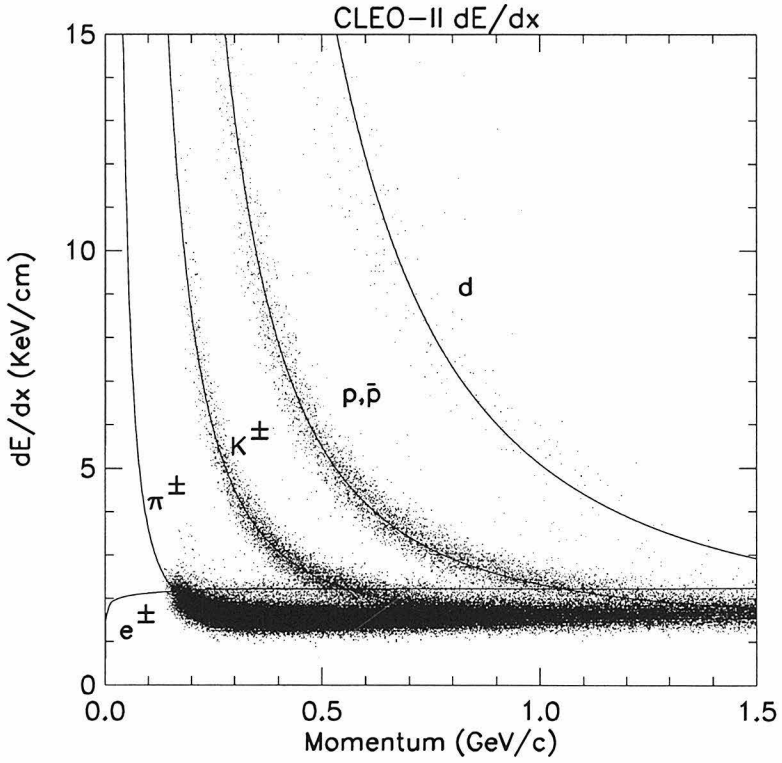


Figure 3.4: $\mathrm{d}E/\mathrm{d}x$ energy loss versus track momentum.

mean, because of the Landau tail. The measured energy loss is characterized as the number of sigma it is away from the energy loss expected for a given particle hypothesis, using the resolution of the measurement. We require a track to have more than 10 measurements for $\mathrm{d}E/\mathrm{d}x$ to be used in this analysis. With at least 40 measurements, the resolution on minimum ionizing pions is 7.1%. Figure 3.4 plots the mean energy loss as a function of momentum. Tracks used in the analysis are corrected for energy loss, using a parametrization based on the track momentum and angle. This correction is applied to the fitted track momentum for a given particle hypothesis.

3.2.2 Time of Flight

Outside of the drift chamber is the time of flight system (TOF). The barrel TOF consists of 64 plastic scintillators that are 5 cm thick, 10 cm wide and 2.8 m long. They provide angular coverage down to 36°. At both ends of the scintillator are lucite light guides which extend almost another 2 m to bring the light to phototubes

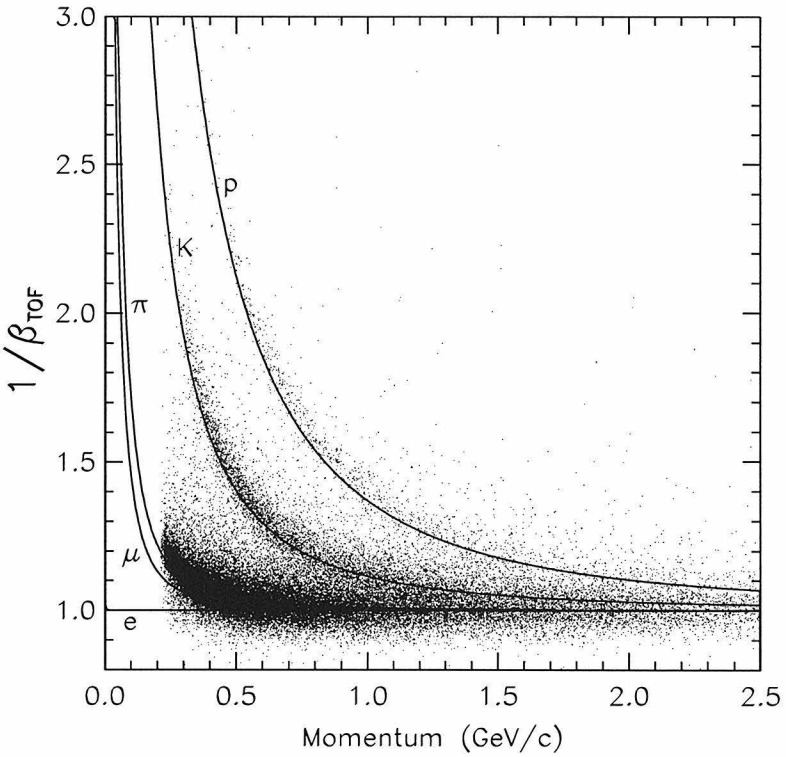


Figure 3.5: $1/\beta$ versus momentum, using the barrel TOF.

outside the detector. The endcap TOF consists of 28 wedges of scintillator which extend the angular coverage down to 15°. At the inner radius, the scintillator is a 45° prism to which the phototube is directly attached. These phototubes are directly inside, and parallel to, the 1.5 T magnetic field. The TOF is used for the L0 trigger and to provide particle identification. The timing resolution is 154 ps for pions in the barrel. This resolution provides greater than 2 σ separation for pions and kaons with momentum below 1 GeV/c. Figure 3.5 plots the measured β as a function of momentum.

3.2.3 Crystal Calorimeter

The barrel Crystal Calorimeter (CC) begins at an inner radius of 1.02 m. The calorimeter is composed of 7800 cesium iodide crystals which are thallium doped to increase light output. The crystals are approximately 5 cm square at the front end, with the barrel crystals tower shaped along the length. The crystals are 30 cm long which corresponds to 16 radiation lengths. The barrel region, with 6144 crystals,

provides coverage down to 32°. The barrel crystals are arranged to point to the vertex for improved angular resolution, but not exactly at the vertex to prevent photons from passing exactly between two crystals. The endcap crystals are all arranged parallel to the z-axis, and overlap with the barrel region to provide coverage from 36° down to 15°. Readout of the scintillation light is accomplished with four photodiodes, each with an active area of 1 cm^2, attached to a lucite window at the end of the crystal. The photodiodes are individually read out and amplified before being combined and shaped into a pulse for the ADC.

The reconstruction software clusters neighboring crystals around the most energetic crystal to define a shower cluster. The cluster is used to calculate the energy and position of a photon shower. The resolution for photons is parametrized as

$$\begin{aligned}
\text{Barrel}: \quad \frac{\sigma_E}{E}(\%) &= \frac{0.35}{E^{0.75}} + 1.9 - 0.1E, \\
\sigma_\phi(\text{mrad}) &= \frac{2.8}{\sqrt{E}} + 1.9, \\
\sigma_\theta(\text{mrad}) &= 0.8\sigma_\phi \sin\theta, \\
\text{Endcap}: \quad \frac{\sigma_E}{E}(\%) &= \frac{0.26}{E} + 2.5, \\
\sigma_\phi(\text{mrad}) &= \frac{3.7}{\sqrt{E}} + 7.3, \\
\sigma_\theta(\text{mrad}) &= \frac{1.4}{\sqrt{E}} + 5.6,
\end{aligned} \tag{3.3}$$

for photon energies in GeV. These correspond to barrel (endcap) energy resolutions of 3.8% (5.0%) at 100 MeV and 1.5% (2.6%) at 5 GeV. The endcap resolution is substantially worse because of the increased material in front of the crystals, due to the drift chamber endplate and readout electronics for the tracking chambers. As a result, this analysis only uses photons in the region $|\cos\theta| < 0.71$, which is the region with the least amount of material in front of the crystals.

For low energy showers, the resolution is dominated by the calibration uncertainty and noise in the readout electronics. At high energies the resolution is dominated by leakage out the back of the crystal. A shower's energy and position are calculated using the N crystals in the shower with the largest energy deposition. The number, N,

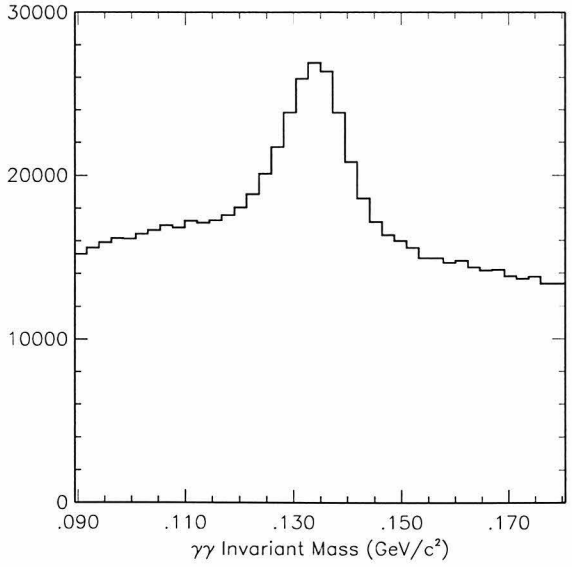


Figure 3.6: Invariant mass of photon pairs in the barrel calorimeter.

of crystals used depends on the shower energy. It increases logarithmically from 4 at 25 MeV to 17 for 4 GeV and greater. Using too many crystals at low energies worsens the resolution because of the electronics noise. At higher energies, more crystals are used in order to measure a larger fraction of the shower. The calorimeter is calibrated using radiative Bhabhas, π° decays, and $e^+e^- \to \gamma\gamma\gamma$ events. The absolute energy calibration is known to $\pm 1\%$ at 25 MeV, $\pm 0.5\%$ at 100 MeV and $\pm 0.2\%$ at 5 GeV.

This analysis uses photons to reconstruct π°'s. The π°'s of interest, for this analysis, are from the decay $D^{*0} \to D^0\pi^\circ$ and have momentum between 0 to 240 MeV/c, or are from the decay $D^0 \to K^-\pi^+\pi^\circ$ with a momentum up to 2 GeV/c. Figure 3.6 plots the two photon invariant mass distribution in the region of the π° mass. The π° mass resolution is typically between 5 and 8 MeV/c^2depending on the energy and angle of the photons. For a π° candidate, the photon energies and directions are kinematically fit to the known π° mass. This yields a π° momentum resolution around 3 MeV/c for low momentum π°'s, but with non-gaussian tails.

3.2.4 Muon Chambers

The return iron of the solenoid is instrumented with plastic proportional chambers to provide muon identification. There are three sets of muon chambers placed in the iron at depths of 36, 72, and 108 cm. These depths correspond to 3, 5, and 7 nuclear interaction lengths (for normal incidence) from the interaction region. There is also one set of muon chambers located at each end of the detector to provide partial coverage of the endcap. Each set has three layers of muon detectors to cover the geometrical efficiency in a single layer, and provide redundancy in the system. The total muon coverage extends down to 30° and covers 85% of the solid angle.

The muon detectors are proportional counters that are 8.3 cm wide, 1 cm thick and 5 m long. Each counter has eight anode wires that are ganged together. The anode wires are separated by the graphite coated plastic "comb-like" structure of the counter, which provides the cathode. External copper strips, perpendicular to the wires, pick up the charge induced on the cathode. The copper strips have an intrinsic space resolution of 5.3 cm. The orthogonal coordinate, from the anode wires, has a space resolution of 2.4 cm, which is due to the counter width. The resolution for matching hits in the muon counters to tracks in the drift chamber depends on the track error parameters, multiple scattering between the drift chamber and the muon chamber, and the intrinsic resolution of the muon chambers. For a 5.28 GeV muon, the resolutions for the layers at 3, 5 and 7 interaction lengths are 3.7, 4.6 and 5.7 cm for the anodes, and 5.5, 7.0, and 7.5 for the cathode strips.

3.2.5 Lepton Identification

Electrons are identified using the ratio E/p, where E is the energy measured in the calorimeter and p is the measured momentum; the shape of the shower; and $\mathrm{d}E/\mathrm{d}x$ energy loss. Figure 3.7 plots the E/p ratio for all tracks. The distributions in these variables are measured for electrons in the data by taking radiative Bhabhas and embedding them in hadronic events. The actual detector hits associated with the Bhabha track are embedded in the hadronic event, before event reconstruction. The

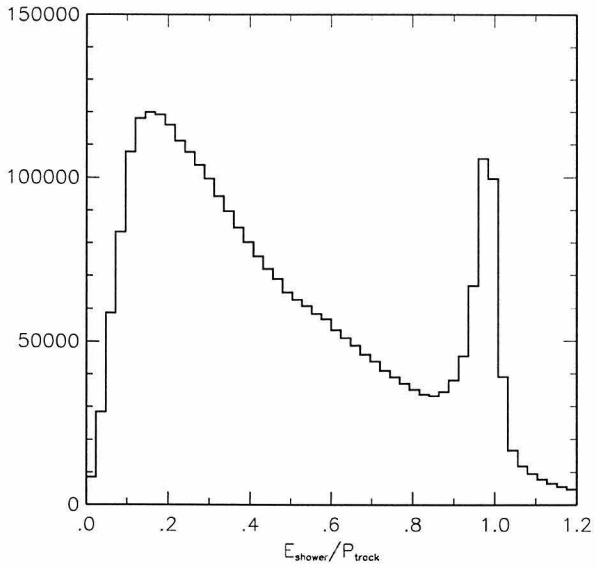


Figure 3.7: The ratio of shower energy to the matching track momentum. The peak at 1. is due to electrons.

distributions in these variables for hadronic tracks are made with tracks from the lepton poor $\Upsilon(1S)$, but with corrections for the small lepton contamination. These distributions are used to construct a log-likelihood defined by [40]

$$R2ELEC = \sum_{variables} \ln(P_e/P_{\not e}), \tag{3.4}$$

where P_e and $P_{\not e}$ are the distributions for electron and hadronic tracks respectively. The distributions are measured for five separate momentum regions, down to 0.4 GeV/c, and four different angular regions for the entire calorimeter.

A separate sample of embedded electrons and hadronic tracks are used to measure the efficiencies and fake rates as a function of $R2ELEC$ for separate momentum slices and angular regions. This analysis uses electrons down to 1.0 GeV/c in momentum and 45° in polar angle, and requires that $R2ELEC > 3$. With this selection criteria, the electron identification efficiency is over 92% [40] and the electron fake rate from pions is $0.30 \pm 0.04\%$ [41].

Muons are identified by matching hits in the muon counters to tracks measured in the drift chamber. Muon candidates are classified by the number of interaction

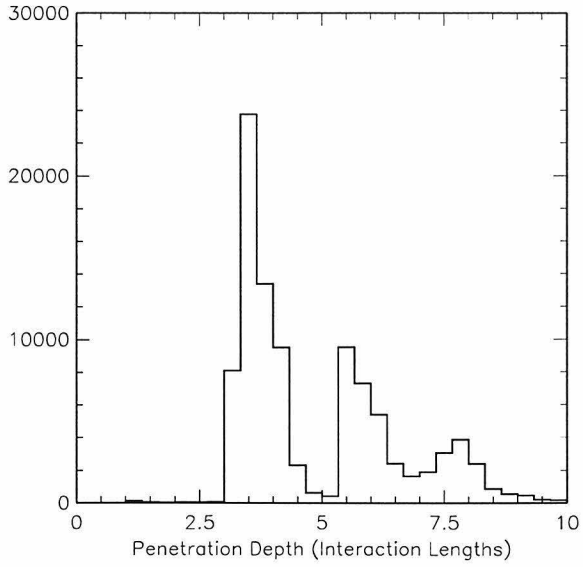


Figure 3.8: Penetration depth, in nuclear interaction lengths, for tracks projecting to hits in the muon chambers. The bin at 0 is suppressed.

lengths penetrated. The muon chamber units are at 3, 5 and 7 interaction lengths for normal incidence. For tracks at other angles, the number of interaction lengths to that unit is larger. Figure 3.8 plots the distribution in depth for tracks matched to muon hits. The depth assigned to a track is the maximum depth with at least two out of three layers hit. We also require hits at all depths which the muon penetrated. This analysis requires a depth greater than five interaction lengths for muon candidates, which imposes a minimum momentum cutoff of around 1.3 GeV/c. With this depth requirement, muon identification rises to 93% for high momentum tracks [42]. The probability that a hadron will fake a muon is 1.2% for pions and 1.6% for kaons [41].

3.2.6 Trigger and Data Acquisition

The CLEO trigger [43] consists of three trigger levels in hardware, and one level in software after the detector has been read out. The CLEO detector is gated with every beam crossing which occurs at a rate of 2.7 MHz. At that time the L0 trigger is formed which uses hits in the time of flight scintillators, crude track segments in the vertex detector, and showers in the crystal calorimeter. This trigger has an

output rate of around 11 kHz. After a successful L0 trigger, all detector gates are disabled. The L1 trigger adds drift chamber hits to the trigger and performs more sophisticated tracking, allowing the charge of the track to be determined. An L1 trigger is typically a combination of some tracking information, time of flight hits, and activity in the crystal calorimeter. L1 takes 1.0 μs and has an output rate near 35 Hz. The L2 hardware trigger provides more sophisticated tracking to help remove beam-wall, beam-gas and cosmic ray backgrounds. L2 requires 50 μs and has an output rate of 20-25 Hz.

The hadronic cross section at the $\Upsilon(4S)$ is 4.5 nb and the tau cross section is 0.91 nb. The Bhabha cross section in the barrel is 10.5 nb and radiative Bhabhas contribute another 5 nb (Endcap Bhabha triggers are prescaled by a factor of 20). μ-pairs and $\gamma\gamma$ events contribute another 2 nb. At an instantaneous luminosity of 2×10^{32} cm^{-2}s^{-1}, these cross sections correspond to a physics trigger rate of about 5 Hz. There is an additional contribution from two-photon events. Typically, CLEO records events with a trigger rate of 25 Hz. The additional non-physics triggers are beam-wall and beam-gas collisions, which depend on the beam conditions for that run, and cosmic ray events which have a trigger rate of roughly 10 Hz. The trigger efficiencies are over 99% for hadronic events.

After the L2 trigger accepts the event, the entire detector is read out. The data acquisition (DAQ) system [44] uses a parallel readout system and VME based CPU's for processing the data and shipping it to the host computer. The front-end digitizes the analog signals that are above threshold and places the output in an event buffer that is 32 events deep. When all the front-end crates have emptied their buffers, the detector is reenabled. This readout time is 2 ms and provides most of the detector dead time. The data are read from the event buffers into several parallel VME CPU boards which provide further sparsification. This sparsification takes between 10-20 ms, which sets the maximum trigger rate at 50 Hz. The event builder cpu assembles the data from the sparsifying cpu's and sends the event to the host computer. The DAQ system also provides monitoring, controls the run status, and interfaces with the trigger. The host computer runs the Level 3 software trigger to further remove

beam related background. About 40% of the events are thrown out by this trigger, with an efficiency of over 99% for hadronic events. The events passing Level 3 are written to disk and then transferred to tape for archival storage.

3.2.7 Offline Reconstruction

The final step in data collection is the offline reconstruction package which uses calibration constants to convert the measured detector information to physics quantities such as track momenta and shower energies. The tracking package reconstructs tracks from hits in the three tracking chambers and then fits the track to obtain the five track parameters, allowing for a hard scatter at the boundary of the VD and DR tracking devices. The track fitter does not correct for $\mathrm{d}E/\mathrm{d}x$ energy loss, which is corrected for in analysis code. The $\mathrm{d}E/\mathrm{d}x$ energy loss for each track is calculated from the drift chamber pulse heights, and track velocity is obtained using time of flight information. The shower reconstruction package sums the crystal energies in neighboring clusters to compute shower energies and centroids. Hits in the muon chambers are grouped to find muon candidates. Vertices are reconstructed for K_s decays and photon conversions, and π° candidates are found and kinematically fit. The reconstructed data is stored in a format accessible by user analysis code.

3.2.8 Monte Carlo Simulation

Several physics Monte Carlo programs for B decays are used in this analysis. The standard CLEO production and decay Monte Carlo, QQ, is used for producing generic B meson decays. This Monte Carlo is used for samples of inclusive B decays, and for generating most background physics processes. The QQ generator typically uses phase space for most hadronic B decays, and various models for semileptonic decays. However, for the signal decay $\bar{B} \to D^* \ell^- \bar{\nu}$ with $D^* \to D\pi$, a separate decay routine, called in QQ, was written by the author which includes the proper angular correlations for the $D\pi\ell\nu$ final state. The other B in the event is decayed using the full set of generic decay modes in QQ. For the $\bar{B} \to D^{**} \ell^- \bar{\nu}$ background decays, the EVT [45]

generator was used. This generator, which was only recently available, properly includes the angular correlations among all subsequent decay products in a decay chain; and contains a more recent set of semileptonic decay models. It has also been interfaced with QQ.

Two separate detector Monte Carlos are used to simulate the detector response to the particles generated in QQ. One Monte Carlo is a GEANT based simulation of the detector called CLEOG. CLEOG takes the produced particle list from QQ and propagates the tracks through the detectors, producing the raw hits in the detector elements. CLEOG has a detailed description of the material in the detector and simulates multiple scattering, photon conversions, bremsstrahlung and hadronic interactions. It also decays pions and kaons, including K_ss. This raw Monte Carlo data is then processed with the standard offline reconstruction code. Before reconstruction, noise hits, obtained from random trigger data, are added to the Monte Carlo data. The CLEOG Monte Carlo is used for signal Monte Carlo, where obtaining the correct efficiency is important. There is also a large sample of CLEOG generic $B\bar{B}$ decays that are useful for comparing data and Monte Carlo.

The time for CLEOG to simulate a $B\bar{B}$ event is typically several seconds. This drawback makes it impractical to simulate extremely large samples of Monte Carlo. As a result a second generator, called TRKSIM, is used. TRKSIM takes the generated Monte Carlo particles, and uses a parametrization of the detector response to produce output tracks and showers with gaussian smearing and efficiency losses. TRKSIM does not produce photon conversions, hadronic interactions in the calorimeter, or large tails in resolution functions. TRKSIM takes only tens of milliseconds to simulate the detector response to an event, and can be directly interfaced to analysis code, which avoids the problem of writing large MC samples to disk.

For the electron identification package used in this analysis, the efficiency and fake rates have been measured in the data, and stored in histograms for momentum slices and angular regions. These histograms are used both with the CLEOG and TRKSIM Monte Carlos so that MC efficiencies and fake rates match the data. Muon identification does not have a similar package, and is unreliable in the TRKSIM MC.

Chapter 4 Data Analysis

4.1 Event Selection

This analysis uses 2.36 fb^{-1} of data taken on the $\Upsilon(4S)$, corresponding to 2.52 million $B\bar{B}$ events, and 1.13 fb^{-1} of continuum data taken at a CM energy 30 MeV below the $\Upsilon(4S)$. The data was recorded between November, 1990 and February, 1994[1].

Events are selected for the decays $B^- \to D^{*0}\ell^-\bar{\nu}$ and $\bar{B}^0 \to D^{*+}\ell^-\bar{\nu}$, with the lepton being either an electron or muon. D^*'s are reconstructed through the decays

- $D^{*0} \to D^0\pi^\circ$ with $D^0 \to K^-\pi^+$ or $D^0 \to K^-\pi^+\pi^\circ$; and
- $D^{*+} \to D^0\pi^+$ with $D^0 \to K^-\pi^+$.

The form factors have previously been measured at CLEO in the decay $\bar{B}^0 \to D^{*+}\ell^-\bar{\nu}$ using both the $D^0 \to K^-\pi^+$ and $D^0 \to K^-\pi^+\pi^\circ$ modes [46]. This is an independent analysis of $\bar{B}^0 \to D^{*+}\ell^-\bar{\nu}$ that was used as a check of the other analysis, but the mode $D^0 \to K^-\pi^+\pi^\circ$ was not added once the other analysis had been completed.

All the backgrounds for $\bar{B} \to D^*\ell^-\bar{\nu}$ can be classified into the five general categories of

1. combinatoric, which are fake D^*'s;
2. correlated, when the D^* and lepton are from the same B meson such as $\bar{B} \to D^*X\ell^-\nu$;
3. uncorrelated, when the D^* comes from one B and the lepton comes from the other B in the event, and hence the momentum of the D^* and lepton are uncorrelated since the B's are produced nearly at rest;
4. $e^+e^- \to q\bar{q}$ continuum, are events not coming from $\Upsilon(4S)$ decays;

[1]The CLEO collaboration refers to this as the 4S2 through 4SA datasets.

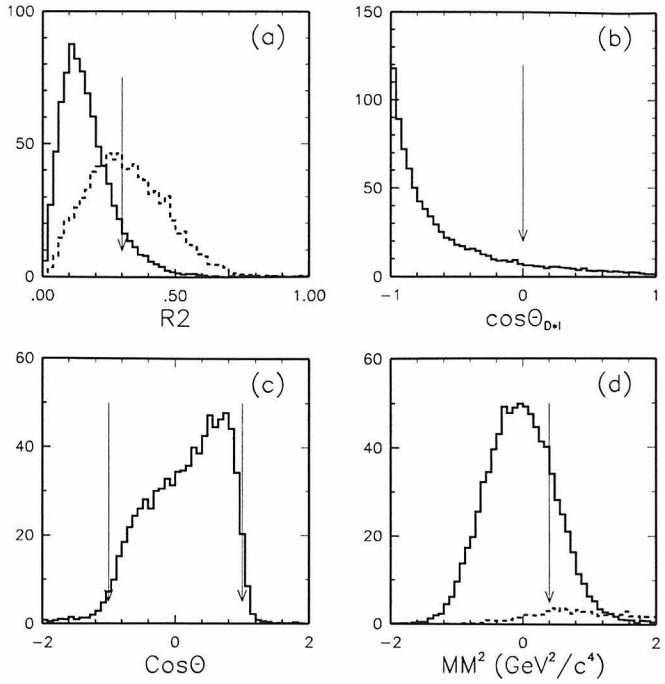


Figure 4.1: The solid line is signal Monte Carlo. All distributions are shown before cuts. a) R2. The dotted line is continuum data. b)$\cos\theta_{D^*l}$. c) $\cos\Theta$. d) MM^2. The dotted line is $D^{**}\ell\nu$ Monte Carlo.

5. and fake leptons.

Backgrounds are described in detail later, but are mentioned here to motivate the selection cuts.

The events are first selected with a hadronic selection criteria that requires three charged tracks originating near the interaction point, and the total visible energy greater than 15% of the center-of-mass energy. This reduces the size of the data sample by removing tau and two photon events, as well as cosmic ray, beam gas and beam wall backgrounds. We make a cut on the total event shape using the ratio, $R2$, of the second and zeroth Fox-Wolfram moments [47]. $B\bar{B}$ events have isotropic or "spherical" decay products since the B mesons are produced nearly at rest. Continuum events have decay products that are more back-to-back or "jet-like" because of the Lorentz boost of the parent quarks. Perfectly spherical events have an $R2$ value of 0, and perfectly back-to-back events have an $R2$ value of 1. We require that $R2 < 0.3$. Figure 4.1a illustrates this cut for signal MC and continuum data.

Tracks used for the decay reconstruction must satisfy track quality criteria. A program called TRKMAN [48] is run on fitted tracks to identify spurious tracks such as "ghosts" which are made from unused hits along a real track, or "curlers" where a second track is found using the hits from a particle curling up inside the drift chamber. If $\mathrm{d}E/\mathrm{d}x$ information exists, then K and π candidate tracks must have energy loss consistent with the particle hypothesis at the 3 σ level. The kaon from $D^0 \to K^-\pi^+\pi^\circ$ has a tighter cut of $\sigma_K > -2$.

As described in section 3.2.5, electron candidates are selected according to a likelihood, R2ELEC, based on the ratio of their energy, as measured in the calorimeter, to their momentum as measured by the tracking chambers; and their $\mathrm{d}E/\mathrm{d}x$ energy loss. Muon candidates must penetrate greater than five nuclear interaction lengths of material, which corresponds to producing hits in at least the second layer of muon counters. This requirement is used to reduce the number of hadrons faking muon candidates but necessitates a minimum momentum requirement of 1.4 GeV/c. Electrons have a minimum momentum cut of 1.0 GeV/c to reduce the correlated $\bar{B} \to D^{**}\ell^-\bar{\nu}$ background, even though electrons are well identified down to 0.8 GeV/c. Leptons have a maximum momentum requirement of 2.45 GeV/c, and must be in the angular region $|\cos\theta| < 0.707$, where θ is defined with respect to the beam direction. Electrons are identified with an efficiency of 95% and a 0.3% probability for a hadron to fake an electron. The muon identification is 93% efficient and has a 1.4% hadron fake rate. Figure 4.2 plots the lepton momentum spectrum for electrons and muons, as well as the likelihood variable for electron identification and the penetration depth used for muon identification.

Reconstructed π°'s use electromagnetic showers that are not associated with a charged track and which lie in the angular region $|\cos\theta_\gamma| < 0.71$. This requires the shower to be in the barrel part of the calorimeter which has the best energy resolution. The showers must have an energy profile consistent with being a photon. This profile is based on the ratio of the sum of the energy in the nine crystals around the highest energy crystal in the shower to the sum of the energy in the 25 crystals around the highest. The π° candidate must be within 2σ of the known π° mass,

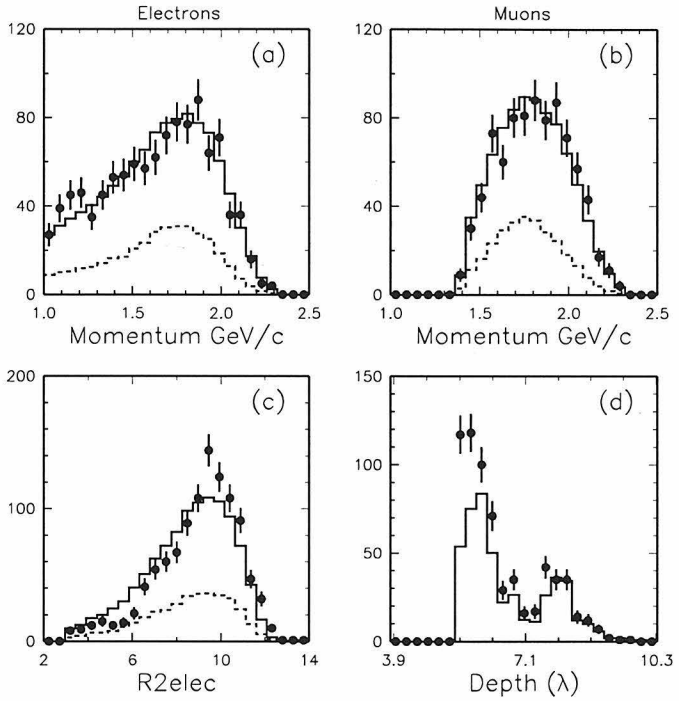


Figure 4.2: The lepton momentum for a) electrons, and b) muons. c) is the likelihood used for electron identification. d) is the penetration depth, in interaction lengths, for muon candidates. The points are the data, the solid line is signal + background MC and the dashed line is the MC background. Because the background is modeled with TRKSIM MC which does not model well muon identification, the last plot only shows data and MC signal.

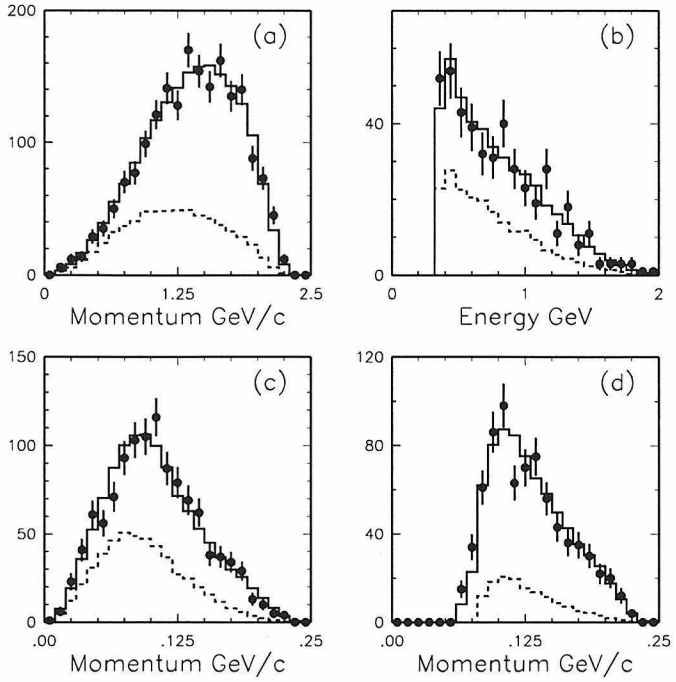


Figure 4.3: a) The D^0 momentum. b) The π° energy for $D^0 \to K^-\pi^+\pi^\circ$. (A cut at 250 MeV has already been applied.) c) The momentum of π°'s from $D^{*0} \to D^0\pi^\circ$. d) The momentum of π^+'s from $D^{*+} \to D^0\pi^+$. The points are the data, the solid line is signal + background MC and the dashed line is the MC background.

where the resolution on the π° mass is between 5 to 8 MeV/c^2 depending on the shower energy and angle. The π°'s are kinematically fit to improve the energy and momentum resolution of the π° candidate and the fitted π° must have a chi-squared less than 8.

The reconstructed D^0 mass must be within 25 MeV/c^2 of the known D^0 mass for both $K\pi$ and $K\pi\pi^\circ$ final states. Figure 4.10 plots the reconstructed D^0 mass for each mode. The D^0 candidate has a maximum momentum requirement of 2.45 GeV/c, which is near the kinematic limit for D's from B decays. The D^0 momentum is plotted in Figure 4.3a.

$D^0 \to K^-\pi^+\pi^\circ$ actually decays through several resonant states as illustrated in the Dalitz plot in Figure 4.4. For the Monte Carlo we use the amplitudes measured by E691 [49]. The combinatoric background for this decay is more widely distributed across the Dalitz plot. To reduce the combinatoric background, a cut is made on the Dalitz amplitude that requires the amplitude to be at least 12% of the peak amplitude.

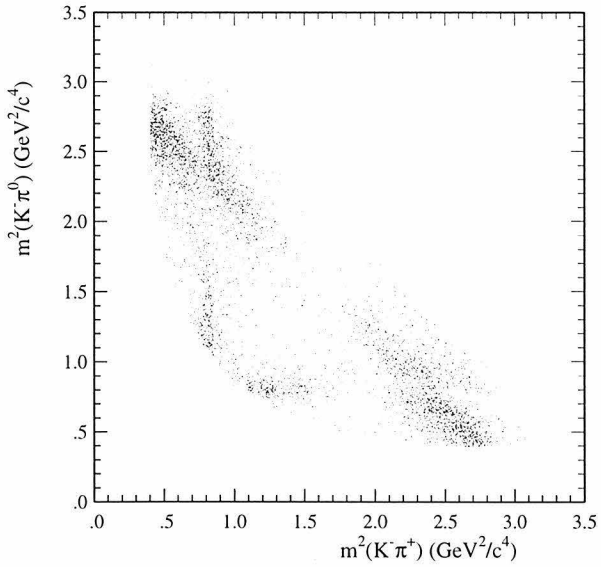


Figure 4.4: The Dalitz plot for the decay $D^0 \to K^-\pi^+\pi^\circ$. The points are from signal Monte Carlo.

This corresponds to a value greater than 45 for the units shown in Figure 4.5. π°'s from $D^0 \to K^-\pi^+\pi^\circ$ must have an energy greater than 350 MeV, and their showers must have energy greater than 50 MeV. Figure 4.3b plots the energy of these π°'s.

D^*'s are reconstructed in the decays $D^{*0} \to D^0\pi^\circ$ and $D^{*+} \to D^0\pi^+$. We make a cut on the reconstructed D^*– D^0 mass difference, δm, and require that it is within 2.0 MeV/c^2 of the known mass difference. Figures 4.7, 4.8, and 4.9 plot the δm distribution for each of the modes. The slow π° has a minimum shower energy requirement of 30 MeV. The slow π^+ has a minimum momentum cut of 65 MeV/c and a minimum p_T cut of 60 MeV/c to exclude the region of low efficiency due to soft tracks curling up. The slow pion momentum is shown in Figure 4.3c,d. Slow pions have a maximum momentum cut of 240 MeV/c which is the kinematic endpoint.

The D^* and lepton are usually produced in opposite hemispheres for signal events, as shown in Figure 4.1b. The uncorrelated background where the D^* and lepton come from different B's in the decay have a distribution that is almost flat in $\cos\theta_{D^*\ell}$. By requiring that $\cos\theta_{D^*\ell} < 0$, we remove half of the uncorrelated background while losing only 1 – 3% of the signal, depending on the mode.

To suppress the correlated background, we use the kinematic constraint that the

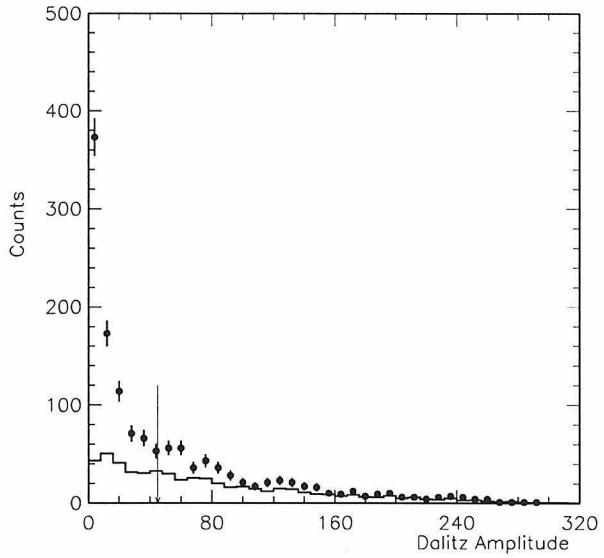


Figure 4.5: The Dalitz amplitude for the decay $D^0 \to K^-\pi^+\pi^\circ$. The points are the data and the solid histogram is signal MC. The arrow indicates the cut value.

neutrino is the only missing particle in the decay. The missing mass squared of the decay, which is the mass squared of the undetected neutrino, is given by

$$m_\nu^2 = (E_B - E_{D^*\ell})^2 - |\vec{p}_B|^2 - |\vec{p}_{D^*\ell}|^2 + 2|\vec{p}_B||\vec{p}_{D^*\ell}|\cos\Theta_{BY}, \qquad (4.1)$$

where $(E_{D^*\ell}, \vec{p}_{D^*\ell})$ is the sum of the measured four momenta of the D^* and the lepton, E_B is the run averaged beam energy and $|\vec{p}_B|$ is the magnitude of the B momentum which is about 340 MeV/c. By setting $m_\nu^2 = 0$ one can solve for the unknown quantity $\cos\Theta_{BY}$. Figure 4.6 illustrates this kinematic constraint. The physically allowed signal region for $\bar{B} \to D^*\ell^-\bar{\nu}$ events is $|\cos\Theta_{BY}| < 1$ which is where we make our cut. This quantity is plotted for signal Monte Carlo in Figure 4.1c. The events outside the physically allowed region are due to measurement errors and lepton bremsstrahlung.

By setting to zero the last term in the above equation, the missing mass squared variable, MM^2, is defined. We require it to be in the region $MM^2 < 0.3$ GeV$^2/c^4$ for the electron modes and $MM^2 < 0.7$ GeV$^2/c^4$ for the muon modes. This variable is shown in Figure 4.1d. This cut is highly correlated with the $|\cos\Theta_{BY}|$ cut, but is

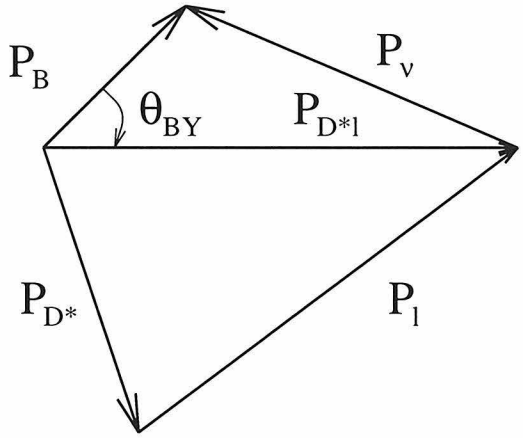


Figure 4.6: The kinematic constraint if the neutrino is the only missing particle in the decay. The B direction lies on a cone, of angle θ_{BY}, around the $D^*\ell$ direction.

used to further reduce the correlated backround. Electrons have a tighter MM^2 cut, since their looser lepton momentum cut accepts more correlated background.

After all cuts, 6% of the $D^{*0}(K\pi)$ and 8.5% of the $D^{*0}(K\pi\pi^\circ)$ events have two or more entries. In this case a χ^2 is constructed for each entry using the π° mass and δm, and the entry with the smallest χ^2 is kept. Signal MC shows that 72% of the time for $K\pi$ and 76% of the time for $K\pi\pi^\circ$, the correct combination is kept. Only 0.8% of D^{*+} events have two entries, and both entries are kept.

4.2 Backgrounds

4.2.1 Combinatoric Background

The combinatoric background comes from reconstruction of fake D^*'s. These fakes come from combining a true D^0 with a random or fake π; or from a fake D^0 and the correct slow π, or from both being fakes. This background is studied using the δm sideband which is defined as $.148 < \delta m < .163$ GeV/c^2 for D^{*0} and $.155 < \delta m < .17$ GeV/c^2 for D^{*+}. The D^{*+} sideband is at larger δm values because the δm peak for

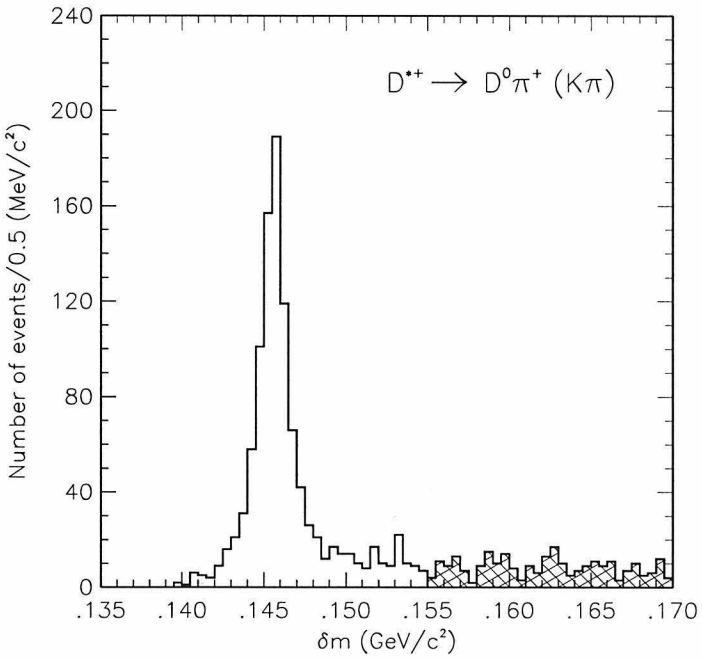


Figure 4.7: The D^*–D^0 mass difference for $D^{*+}(K\pi)$ after all cuts. The hatched region defines the δm sideband.

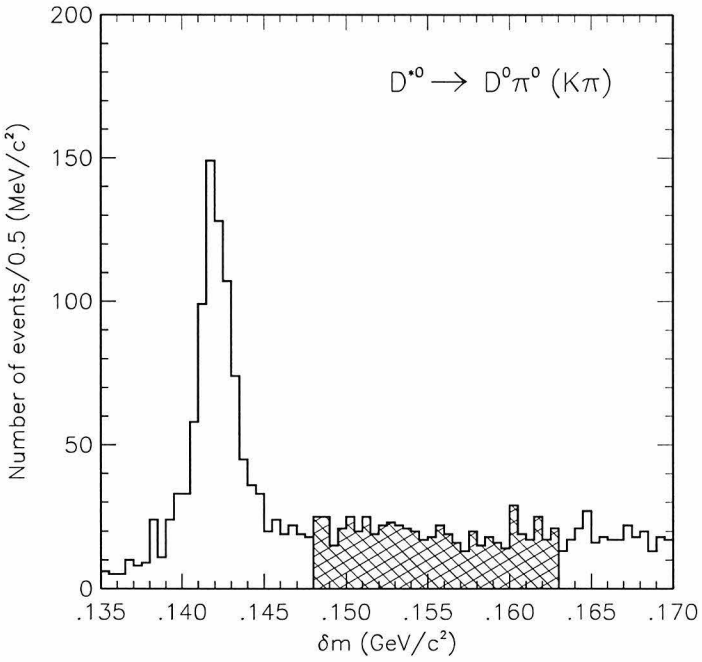


Figure 4.8: The D^*–D^0 mass difference for $D^{*0}(K\pi)$ after all cuts. The hatched region defines the δm sideband.

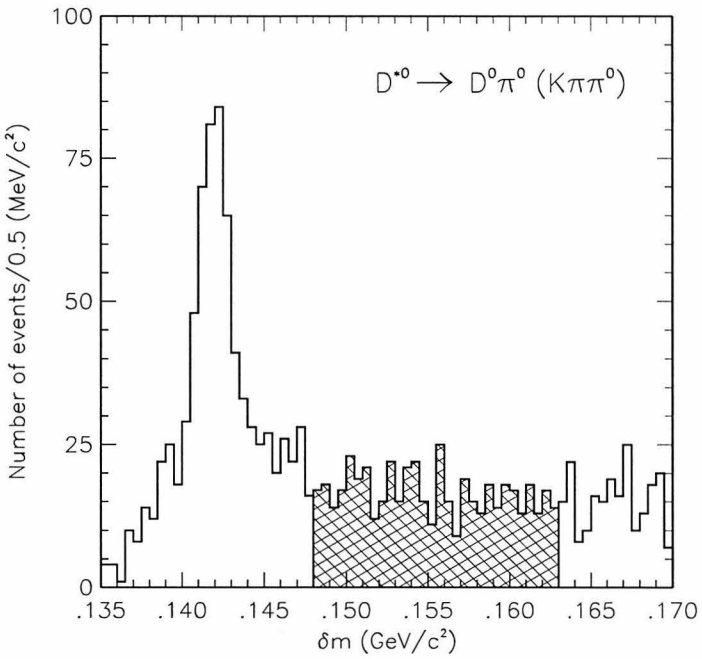


Figure 4.9: The D^*–D^0 mass difference for $D^{*0}(K\pi\pi^\circ)$ after all cuts. The hatched region defines the δm sideband.

signal events has a long non-Gaussian tail for signal events due to systematic errors in slow track reconstruction. Figures 4.7, 4.8, and 4.9 show the δm distribution for each mode.

We measure the combinatoric background by fitting the D^0 mass distribution for both the δm signal and sideband regions, and then subtracting the scaled D^0 yield in the δm sideband region from the D^0 yield in the signal region. In this way the fake D^0 contribution to the background is measured in the signal region and the real D^0 contribution is measured in the δm sideband. The D^0 mass peak is fit to a double gaussian for the signal and a first order chebyshev polynomial for the background [50]. The double gaussian is first fit to signal Monte Carlo and the parameters for the second gaussian, relative to the first, are then fixed when fitting the data. Figure 4.10 shows the fit of the D^0 mass distributions.

Because fakes may contain some of the correct daughter particles, the combinatoric background is not flat across the δm peak and sidebands. Furthermore, for events with multiple entries, a single entry is chosen using information from the δm distribution

which causes some backgrounds to peak in the δm signal region. Therefore, the scale factor between the δm signal and sideband regions, for the combinatoric background containing real D^0's, is obtained from Monte Carlo. Figure 5.5 illustrates the Monte Carlo shape of the combinatoric background for the $D^{*0}(K\pi)$ δm distribution. Figure 4.10 shows the fit of the D^0 mass distributions. Table 4.1 gives the fit yields and scale factors for the combinatoric background. The amount of combinatoric background is given by

$$\text{N(combinatoric)} = \text{N(fake } D^0 \text{ in signal)} + \alpha \times \text{N(real } D^0 \text{ in sideband)}, \qquad (4.2)$$

where α is the scale factor determined from Monte Carlo. We assume the same combinatoric background fraction for electrons and muons.

Because of the non-gaussian tail for the D^{*+} signal δm distribution, some fraction of the real D^0 events in the sideband are actually signal events. The ratio of D^{*+} signal events in the sideband to those in the signal region is 0.03 as determined from Monte Carlo. We use this to correct the yield of D^0's in the sideband region.

We find the combinatoric background to be 12%, 34%, and 46% of the total yield for the $D^{*+}(K\pi)$, $D^{*0}(K\pi)$, and $D^{*0}(K\pi\pi^\circ)$ modes respectively. When measuring real D^* backgrounds in the data, such as continuum and uncorrelated backgrounds, we correct for the combinatoric contribution to those samples. Those samples are quite small, so the combinatoric contribution to those backgrounds is obtained by scaling the number of events in the δm sideband. We obtain this scale factor using the ratio of combinatoric events in the signal region to the number of events in the δm sideband region that we have measured in this section. We determine this ratio to be 0.36 for $D^{*+}(K\pi)$, 0.40 for $D^{*0}(K\pi)$, and 0.41 for $D^{*0}(K\pi\pi^\circ)$.

4.2.2 Correlated Background

Correlated background events are when the D^* and lepton come from the same B meson and so are correlated in energy and momentum. This can happen through channels such as

Mode	$D^{*+}(K\pi)$	$D^{*0}(K\pi)$	$D^{*0}(K\pi\pi^{\circ})$
Events in Signal	763	693	451
Events in Sideband	259	599	500
D^0 yield in Signal	703	562	318
Fake D^0 in Signal	60	131	133
D^0 yield in Sideband	127	321	213
Scale Factor α	0.29	0.34	0.35
Total Fake D^* Background	92	239	207

Table 4.1: The fit yields and scale factors used for determining the combinatoric background.

- $\bar{B} \to D^{**}\ell^-\nu$ with $D^{**} \to D^*\pi$,
- $\bar{B} \to (D^*\pi)_{non-resonant}\ell^-\nu$,
- $\bar{B} \to D^*\tau^-\bar{\nu}$ with $\tau^- \to \ell^-\bar{\nu}\nu$,
- $\bar{B} \to D^*D_s^-X$ and $D_s^- \to X\ell^-$,
- $\bar{B} \to D^*\bar{D}X$ and $\bar{D} \to X\ell^-$,
- $\bar{B} \to D^*K(\pi)$ and $K(\pi) \to X\mu^-$,
- $\bar{B} \to D^*X\gamma(\pi^{\circ})$ and $\gamma \to e^+e^-$ $(\pi^{\circ} \to e^+e^-\gamma)$.

The D^{**} modes, including $D^*\pi$ non-resonant, are a significant source of background with a non-trivial distribution over the four-dimensional fit space. The other correlated modes are a negligible source of background, as predicted by MC simulations and estimated branching ratios.

For signal events the MM^2 distribution is a broad peak centered near zero. For D^{**} events, the MM^2 distribution is shifted to positive MM^2 values because of the missing pions as shown in Figure 4.1d. Furthermore, these modes have a softer lepton spectrum due to less available q^2 in the decay, and extend to non-physical values of $\cos\Theta_{BY}$.

The D^{**} states are orbitally excited ($L = 1$) charm mesons. In HQET the relevant quantum numbers for the states are the total angular momentum, J, and the total

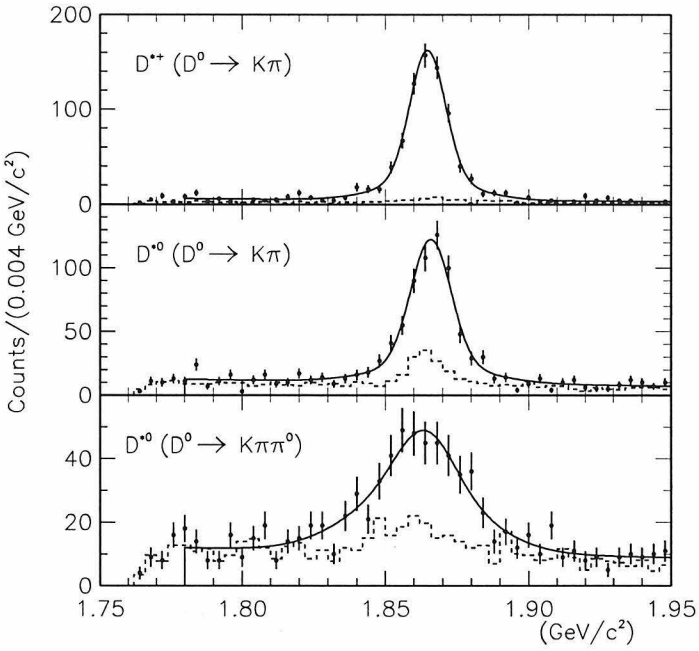


Figure 4.10: The points are the D^0 candidate mass distribution for events from the δm signal region. The solid line is a fit to a (double) Gaussian signal and a linear polynomial for the background. The dashed line is the scaled mass distribution for events from the δm sideband region.

angular momentum of the light degrees of freedom, $j_\ell = \ell + s_\ell$; and the states are denoted by $P_J^{j_\ell}$. These states are the $P_0^{(1/2)}$, $P_2^{(3/2)}$, $P_1^{(3/2)}$ and the $P_1^{(1/2)}$ resonances predicted by HQET [51]. The $P_0^{(1/2)}$ only decays to the $D\pi$ final state via an S-wave, and is expected to be a broad resonance. The $P_2^{(3/2)}$ and $P_1^{(3/2)}$ are the $D_2^*(2460)$ and the $D_1(2420)$ which have been observed by CLEO [52, 53]. The $P_1^{(1/2)}$ is expected to be a broad resonance since it decays to $D^*\pi$ via S-wave. We determine the size of this background using recent measurements from the ALEPH and CLEO experiments [54, 55]. ALEPH has measured $\mathcal{B}(b \to \bar{B})\mathcal{B}(\bar{B} \to D_1^0 \ell^- \bar{\nu} X)\mathcal{B}(D_1^0 \to D^{*+}\pi^-) = (2.04 \pm 0.58 \pm 0.34) \times 10^{-3}$. Using $\mathcal{B}(b \to \bar{B}) = (0.378 \pm 0.022)\%$, we obtain $\mathcal{B}(\bar{B} \to D_1^0 \ell^- \bar{\nu} X)\mathcal{B}(D_1^0 \to D^{*+}\pi^-) = (0.52 \pm 0.17)\%$, assuming X to be nothing. CLEO has measured $\mathcal{B}(B^- \to D_1^0 e^- \bar{\nu})\mathcal{B}(D_1^0 \to D^{*+}\pi^-) = (0.33 \pm 0.09 \pm 0.04)\%$. We combine the ALEPH and CLEO results to obtain $\mathcal{B}(B \to D_1^0 \ell \bar{\nu} X)\mathcal{B}(D_1 \to D^{*+}\pi^-) = (0.40 \pm 0.07)\%$. In order to apply these results to the D^{*0} mode, we assume that they are produced at the same rate.

The ISGW2 model predicts $\mathcal{B}(B^- \to D_1^0 \ell^- \bar{\nu}) = 0.45\%$. Assuming $\mathcal{B}(D_1^0 \to D^{*+}\pi^-) = 2/3$ using isospin, we obtain the prediction $\mathcal{B}(B \to D_1^0 \ell \bar{\nu} X)\mathcal{B}(D_1 \to D^{*+}\pi^-) = 0.30\%$, which is consistent with the measured result. ISGW2 predicts the rate for $\bar{B} \to D_2^* \ell^- \bar{\nu}$ to be half of the rate to $D_1 \ell \bar{\nu}$, and the rate to the $P_1^{(1/2)}$ state to be 1/6 the rate to the D_1.

We use the measured branching ratio to estimate the amount of background from $B \to D_1^0 \ell \bar{\nu} X$. For the other D^{**} states we take the semileptonic widths from the ISGW2 model and normalize to the D_1 state. We place an uncertainty on the ISGW2 prediction for the rate to D_2^* to match the upper limit $\mathcal{B}(B^- \to D_2^{*0} e^- \bar{\nu})\mathcal{B}(D_2^{*0} \to D^{*+}\pi^-) < 0.19\%$ as measured by CLEO. For D_2^*'s, we also use the ratio $\mathcal{B}(D_2 \to D\pi)/\mathcal{B}(D_2 \to D^*\pi) \approx 2$ as predicted by HQET and measured by CLEO as 2.2 ± 0.9 [52]. We assign a 100% error to the $P_1^{(1/2)}$ mode to cover the theoretical error.

ALEPH reports the inclusive branching ratio of $\mathcal{B}(b \to \bar{B})\mathcal{B}(\bar{B} \to D^{*+}\pi^-\ell^-\bar{\nu}X) = (4.73 \pm 0.77 \pm 0.55) \times 10^{-3}$. This converts to $\mathcal{B}(\bar{B} \to D^{*+}\pi^-\ell^-\bar{\nu}X) = (1.25 \pm 0.25)\%$. Subtracting the rates to the resonant modes determined above, gives an estimate of the rate to $D^*\pi\ell\bar{\nu}$ non-resonant. We take it to be $\mathcal{B}(\bar{B} \to (D^*\pi)_{nonres}\ell^-\bar{\nu}) = (0.71 \pm 0.30)\%$.

We use Monte Carlo to determine the efficiency, with the ISGW2 model for the D^{**} modes and the model of Goity and Roberts [56] for the non-resonant state. Table 4.2 lists the branching ratio estimates, efficiencies from MC and the expected number of events. We assume that $\mathcal{B}B^- \to D^{**0}\ell^-\bar{\nu}$ equals $\mathcal{B}\bar{B}^0 \to D^{**+}\ell^-\bar{\nu}$. Using the isospin relation that $\mathcal{B}(D^{**0} \to D^{*+}\pi^-) = 2\mathcal{B}(D^{**+} \to D^{*+}\pi^\circ)$, there will be twice as many events from B^-'s as from $\bar{B}^0$'s; and vice versa for D^{*0}. The expected number of events is thus

$$N = 1.5 N_{B\bar{B}} \mathcal{B}(\bar{B} \to D^{**}\ell^-\bar{\nu})\mathcal{B}(D^{**} \to D^*\pi^+)\mathcal{B}(D^* \to D\pi)\mathcal{B}(D^0 \to K^-\pi^+)\epsilon. \quad (4.3)$$

The efficiency, ϵ, has been obtained from Monte Carlo only for the $D^{*+}(K\pi)$ and $D^{*0}(K\pi)$ modes. For the $D^{*0}(K\pi\pi^\circ)$ mode we scale the $D^{*0}(K\pi)$ number by the ratio of real D^{*0} yields in the data for the two modes. This scale factor is 0.54.

For the other correlated backgrounds, we use TRKSIM Monte Carlo, which overestimates the efficiency, to determine the number of events passing our cuts. Table 4.3 gives the branching ratios and efficiencies used for determining the size of these backgrounds. These backgrounds tend to be suppressed because of their soft lepton momentum spectrum and large missing mass squared due to other particles in the decay. The mode $\bar{B} \to D^* D_s^-$ with $D_s^- \to \mu^- \bar{\nu}$ has the same final state and almost the same distribution as the longitudinal component of the signal decay with $q^2 = m_{D_s}^2$. As a result the efficiency for this background is comparable to that for a signal event. However, the branching ratios, $\mathcal{B}(D_s^- \to \mu^- \bar{\nu}) = (9 \pm 4) \times 10^{-3}$ and $\mathcal{B}(\bar{B}^0 \to D^{*+} D_s^-) = 1.2 \pm 0.6\%$ [3], reduce the size of this background.

Mode	$\mathcal{B}(\bar{B} \to D^{**} \ell^- \bar{\nu}) \times$ $\mathcal{B}(D^{**} \to D^* \pi)$	efficiency(%)		# expected	
		D^{*+}	D^{*0}	D^{*+}	D^{*0}
$D_1\ e$	0.40 ± 0.07	3.20 ± 0.12	2.30 ± 0.16	12.7 ± 2.3	8.6 ± 1.6
$D_1\ \mu$	0.40 ± 0.07	3.33 ± 0.13	2.65 ± 0.15	13.2 ± 2.4	7.9 ± 1.5
$D_2\ e$	0.07 ± 0.12	2.79 ± 0.12	2.21 ± 0.12	1.9 ± 3.3	1.4 ± 2.5
$D_2\ \mu$	0.07 ± 0.12	3.16 ± 0.12	2.30 ± 0.14	2.2 ± 3.8	1.4 ± 2.5
$P_1^{(1/2)}\ e$	0.07 ± 0.07	2.93 ± 0.12	2.40 ± 0.13	2.0 ± 2.0	1.4 ± 1.4
$P_1^{(1/2)}\ \mu$	0.07 ± 0.07	3.80 ± 0.12	2.20 ± 0.14	2.6 ± 2.6	1.7 ± 1.7
Non-res e	0.71 ± 0.30	0.69 ± 0.06	0.89 ± 0.06	4.9 ± 2.1	5.7 ± 2.5
Non-res μ	0.71 ± 0.30	0.92 ± 0.06	0.81 ± 0.08	6.5 ± 2.8	5.2 ± 2.3

Table 4.2: The estimated amount of D^{**} background in the $K\pi$ channels.

4.2.3 Uncorrelated Background

Uncorrelated backgrounds are events where the D^* and right sign lepton do not come from the same B. Examples of these include events such as:

- $\bar{B} \to D^* X$ with the other B producing a right sign lepton via a cascade decay such as $B \to \bar{D} X, \bar{D} \to X \ell^-$ or $B \to \psi X, \psi \to \ell^+ \ell^-$;
- mixed events where $\bar{B}^0 \to D^* X$ and $B^0 \to \bar{B}^0 \to X \ell^- \bar{\nu}$;
- and upper vertex charm with $\bar{B} \to X \ell^-$ and $B \to \bar{D} D^* X$.

Mode	$\mathcal{B}(\bar{B} \to D^* X) \times$ $\mathcal{B}(X \to Y\ell^-)$	efficiency(%)	#expected
$\bar{B} \to D^* \tau^- \bar{\nu}$ $\tau^- \to e^- \bar{\nu} \nu$	$(0.027 \pm 0.004) \times$ (0.1783 ± 0.08)	0.36 ± 0.06	1.0 ± 0.2
$\bar{B} \to D^* D_s^-$ $D_s^- \to \mu^- \bar{\nu}$	$(0.012 \pm 0.006) \times$ (0.009 ± 0.004)	11.4 ± 0.3	0.7 ± 0.5
$\bar{B} \to D^* D_s^{*-}$ $D_s^* \to D_s \gamma (D_s^- \to \mu^- \bar{\nu})$	$(0.019 \pm 0.012) \times$ (0.009 ± 0.004)	10.6 ± 0.3	1.1 ± 0.8
$\bar{B} \to D^* D_s^-$ $D_s^- \to X \ell \bar{\nu}$	$(0.012 \pm 0.006) \times$ (0.079 ± 0.03)	0.24 ± 0.05	0.14 ± 0.09
$\bar{B} \to D^* \bar{D} K$ $\bar{D}^0 \to X e^-$	$(0.10 \pm 0.05) \times$ (0.077 ± 0.012)	0.0025 ± 0.0025	0.01 ± 0.01

Table 4.3: The estimated amount of correlated background for modes not included in the fit. The efficiency is obtained from MC using just the $D^{*0}(K\pi)$ channel, but the backgrounds will be comparable or less for the other modes. The efficiency error is just due to MC statistics. The $D^{*0} \to D^0 \pi^\circ$ and $D^0 \to K^- \pi^+$ branching ratios have also been used in obtaining the number of expected events.

Since both B's are almost at rest and decay isotropically, the angle between the D^* and lepton is uncorrelated and the D^* and lepton will equally likely be in the same or opposite hemisphere. In contrast, signal events usually have the D^* and lepton going into opposite hemispheres. The size of this background is estimated from the data using the flipped lepton technique [57]. This technique takes same hemisphere $D^* l$ pairs, where $\cos\theta_{D^*\ell} > 0$, and flips the lepton direction. Variables which depend on the lepton direction, such as MM^2 and $\cos\Theta_{BY}$, are calculated before applying the analysis cuts.

Figure 4.11 shows the δm distribution of the flipped events after all cuts. The combinatoric background contribution is removed by subtracting the scaled δm sidebands, where the scale factor comes from the fraction of combinatoric background for signal events as determined earlier. Of the real D^*–lepton events, after the combinatoric subtraction, some fraction are actually signal events with the D^* and lepton in the same hemisphere. We use signal Monte Carlo to estimate the ratio for signal events to end up in the flipped sample relative to the signal region. This ratio is different for electrons and muons because of the different lepton energy cuts. This

ratio times the number of observed signal events (after all background subtractions) gives the estimate of how many flipped events are actually signal events. This requires solving for the amount of uncorrelated background at the same time as solving for the number of signal events. We solve the following equation for the number of signal events, N_{signal},

$$N_{signal} = N_{events} - N_{background} - (N_{fl} - \beta N_{signal}). \tag{4.4}$$

N_{events} is the total number of events in the signal region, N_{fl} is the number of real D^*–lepton flipped events, $N_{background}$ is the sum of all the backgrounds except for N_{fl}, and β is the ratio for a signal event to be in the flipped sample relative to being in the signal region. The ratio is different for electrons and muons because of the difference in lepton energy cuts. This ratio is also smaller for the D^{*+} mode, because it has a lower efficiency at high q^2 where the D^* and lepton are more likely to be produced in the same hemisphere. Table 4.4 lists the numbers relevant to determining the uncorrelated background level, and the estimated uncorrelated background is given in Tables 4.5, 4.6 and 4.7.

Mode	Flipped Events	Scaled Sideband	Ratio β
$D^{*+}(K\pi)$ e's	23	10.3 ± 2.3	0.0177 ± 0.0007
$D^{*+}(K\pi)$ μ's	8	7.8 ± 1.9	0.0059 ± 0.0005
$D^{*0}(K\pi)$ e's	45	31.4 ± 4.0	0.0358 ± 0.0008
$D^{*0}(K\pi)$ μ's	44	37.8 ± 4.5	0.0272 ± 0.0009
$D^{*0}(K\pi\pi^0)$ e's	29	25.2 ± 4.2	0.0290 ± 0.0012
$D^{*0}(K\pi\pi^0)$ μ's	27	21.5 ± 3.8	0.0218 ± 0.0013

Table 4.4: The Number of events and the ratio used for determining the uncorrelated background. The error on β is just due to MC statistics.

4.2.4 Continuum Background

Continuum background sources of real D^*–lepton pairs are measured using the data taken at energies below the $\Upsilon(4S)$ resonance. The requirements on R2 and the mo-

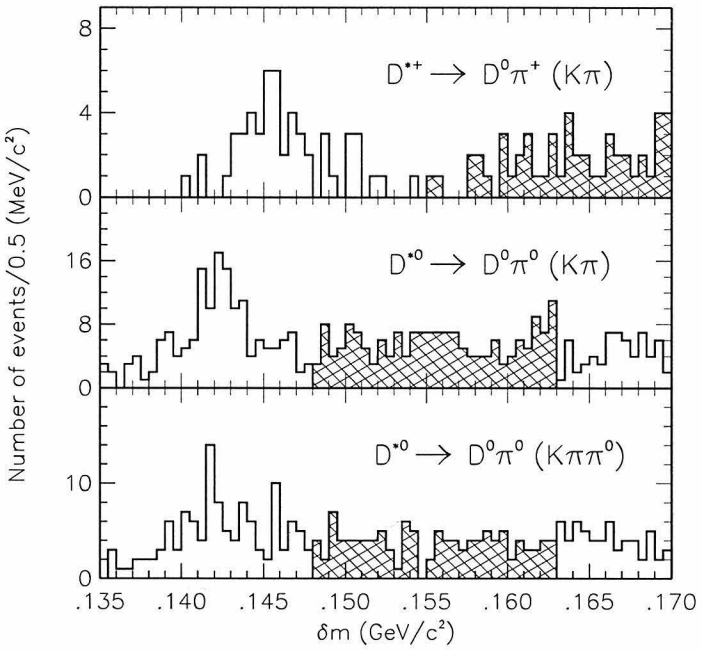


Figure 4.11: The δm distribution for flipped events after all cuts. The hatched region defines the δm sideband.

mentum of the D^* daughters are used to reduce this background. Applying all cuts to the continuum sample, subtracting combinatoric and uncorrelated backgrounds, and scaling according to luminosity and cross section, gives the estimate of the continuum background. The combinatoric background is subtracted by scaling the δm sideband regions by the scale factor determined in section 4.2.1. The amount of continuum background as measured in the off-resonance sample, must be scaled to obtain the number of events expected in the on-resonance sample. The scale factor is $\frac{\mathcal{L}(\text{on})E^2_{CM}(\text{off})}{\mathcal{L}(\text{off})E^2_{CM}(\text{on})} = 2.06$, where $\mathcal{L}$ is the luminosity of the data samples, and we have used the fact that the cross section for continuum quark production falls as the square of the CM energy. The size of this background is small.

4.2.5 Lepton Fakes

Fake leptons come from charged pions and kaons which pass our lepton selection criteria. Since fake leptons that come from a different B than the D^* are included in the uncorrelated background estimate, we only need to know the number of correlated

fake leptons.

We measure the fake lepton backround directly in the data using hadrons identified as not being leptons, and the known lepton fake rates. We make our analysis cuts in selecting D^* plus hadron combinations, where the hadron has been selected to not be a lepton. We multiply the yield of real D^*'s by the lepton fake rates of $(0.3 \pm 0.1)\%$ for electrons and $(1.4 \pm 0.2)\%$ for muons. This background is small and the amount of background is given in Tables 4.5, 4.6 and 4.7.

Event Type	Electron	Muon	Combined
Signal Region	428	335	763
Combinatoric	48 ± 7	44 ± 7	92 ± 11
Correlated Background	22 ± 5	25 ± 6	46 ± 11
Uncorrelated Background	6 ± 5	0 ± 3	6 ± 6
Continuum	0 ± 2	3 ± 3	3 ± 3
Correlated Fake Leptons	1 ± 1	3 ± 1	3 ± 1
Signal Events	352 ± 23	262 ± 21	614 ± 32
Efficiency	10.61%	8.12%	

Table 4.5: The yield of $D^{*+}(K\pi)$ signal events and estimated backgrounds in the signal region.

Event Type	Electron	Muon	Combined
Signal Region	376	317	693
Combinatoric	125 ± 8	114 ± 8	239 ± 11
Correlated Background	17 ± 4	16 ± 4	33 ± 8
Uncorrelated Background	5 ± 8	1 ± 8	7 ± 11
Continuum	0 ± 4	0 ± 8	0 ± 5
Correlated Fake Leptons	1 ± 1	0 ± 1	1 ± 1
Signal Events	227 ± 23	185 ± 23	413 ± 32
Efficiency	7.92%	6.56%	

Table 4.6: The yield of $D^{*0}(K\pi)$ signal events and estimated backgrounds in the signal region.

Event Type	Electron	Muon	Combined
Signal Region	266	185	451
Combinatoric	113 ± 14	94 ± 12	207 ± 20
Correlated Background	9 ± 3	9 ± 3	18 ± 5
Uncorrelated Background	0 ± 7	4 ± 6	4 ± 9
Continuum	0 ± 4	7 ± 5	3 ± 6
Correlated Fake Leptons	1 ± 1	3 ± 1	3 ± 1
Signal Events	143 ± 23	70 ± 20	216 ± 32
Efficiency	1.05%	0.87%	

Table 4.7: The yield of $D^{*0}(K\pi\pi^0)$ signal events and estimated backgrounds in the signal region.

4.3 Branching Ratio

Although the purpose of this analysis is not a measurement of a branching ratio, it is useful to calculate the branching ratio obtained as a general check on the background and efficiency estimations. The number of $B\bar{B}$ pairs is obtained from the reported luminosity, $(2.36 \pm .02)$ fb^{-1}, and the cross section $\sigma_{B\bar{B}} = (1.07 \pm .02)$ nb. We also make the assumption that B^+B^- and $B^0\bar{B}^0$ pairs are produced in equal numbers, and that $f_{+-} = f_{00} = 0.5$. The efficiency used is obtained from Monte Carlo which has been generated with the ISGW model. The error quoted for the efficiency is due to Monte Carlo statistics only and hence ignores a theoretical model dependence. The efficiency and other numbers relevant for calculating the branching ratio are given in Tables 4.8 and 4.9.

	$D^{*+}(K\pi)$
Signal Events	614± 32
Efficiency	$(9.37 \pm 0.03)\%$
$\mathcal{B}(D^{*+} \to D^0\pi^+)$	0.683 ± 0.014
$\mathcal{B}(D^0 \to K^-\pi^+)$	0.0383 ± 0.0012
$\mathcal{B}(\bar{B}^0 \to D^{*+}\ell^-\bar{\nu})$	$(4.97 \pm 0.26 \pm 0.21)\%$

Table 4.8: $\bar{B}^0 \to D^{*+}\ell^-\bar{\nu}$ branching ratio numbers.

	$D^{*0}(K\pi)$	$D^{*0}(K\pi\pi^\circ)$
Signal Events	413 ± 32	216 ± 32
Efficiency	$(7.24 \pm 0.0002)\%$	$(0.96 \pm 0.005)\%$
$\mathcal{B}(D^{*0} \to D^0\pi^\circ)$	0.619 ± 0.029	0.619 ± 0.029
$\mathcal{B}(D^0 \to K^-\pi^+(\pi^\circ))$	0.0383 ± 0.0012	0.139 ± 0.009
$\mathcal{B}(B^- \to D^{*0}\ell^-\bar{\nu})$	$(4.78 \pm 0.37 \pm 0.29)\%$	$(5.18 \pm 0.76 \pm 0.43)\%$

Table 4.9: $B^- \to D^{*0}\ell^-\bar{\nu}$ branching ratio numbers.

The branching ratios we measure are

$$\begin{aligned} \mathcal{B}(\bar{B}^0 \to D^{*+}\ell^-\bar{\nu}) &= (4.97 \pm 0.26 \pm 0.21)\%, \text{and} \\ \mathcal{B}(B^- \to D^{*0}\ell^-\bar{\nu}) &= (4.85 \pm 0.33 \pm 0.28)\%. \end{aligned} \tag{4.5}$$

The systematic error does not contain any contribution from the uncertainty in the detector modeling of the absolute efficiency. These results compare to the published CLEO values $\mathcal{B}(\bar{B}^0 \to D^{*+}\ell^-\bar{\nu}) = (4.57 \pm 0.33 \pm 0.40)\%$ and $\mathcal{B}(B^- \to D^{*0}\ell^-\bar{\nu}) = (5.38 \pm 0.57 \pm 0.67)\%$[9], where the central values have been scaled by the change in D^* and D^0 branching ratios used. These measurements are partially statistically correlated with our measurements.

These previous CLEO measurements had a 7.2% and 9.8% systematic error, for D^{*+} and D^{*0} modes respectively, due to uncertainties in the MC simulation of the detector efficiency. These include the absolute efficiency for lepton identification, slow pion finding and D^0 reconstruction, among others. We add that uncertainty to our branching ratio measurement, when calculating the quantities below.

We use the measured B lifetimes to convert the measured branching ratio to a decay width. The measured branching ratio, $\mathcal{B}$(Measured), is related to the true branching ratio, $\mathcal{B}$(True), by the ratio $f_{+-(00)}/0.5$. This gives the relation

$$\Gamma(\bar{B} \to D^*\ell^-\bar{\nu}) = \frac{\mathcal{B}(\text{True})}{\tau_B} = \frac{\mathcal{B}(\text{Measured})0.5}{f_{+-(00)}\tau_B}. \tag{4.6}$$

If we assume that the decay width $\Gamma(\bar{B} \to D^*\ell\nu)$ is the same for charged and neutral

B mesons, we can measure it for both modes combined, by using

$$\Gamma(\bar{B}^0 \to D^{*+}\ell^-\bar{\nu})f_{00} + \Gamma(B^- \to D^{*0}\ell^-\bar{\nu})f_{+-} = \Gamma(\bar{B} \to D^*\ell^-\bar{\nu}). \tag{4.7}$$

We obtain the result

$$\begin{aligned} \Gamma(\bar{B} \to D^*\ell\nu) &= \frac{1}{2}\left[\frac{\mathcal{B}(\bar{B}^0 \to D^{*+}\ell^-\bar{\nu})}{\tau_{\bar{B}^0}} + \frac{\mathcal{B}(B^- \to D^{*0}\ell^-\bar{\nu})}{\tau_{B^-}}\right] \\ &= (30.7 \pm 3.0)\text{ns}^{-1}, \end{aligned} \tag{4.8}$$

using $\tau_{B^-} = (1.65 \pm 0.04)$ ps and $\tau_{\bar{B}^0} = (1.55 \pm 0.04)$ ps [10]. This gives the width independent of the production ratio f_{+-}/f_{00}, although we do assume that $f_{+-} + f_{00} = 1$.

Again assuming equal partial widths, we can obtain a measurement of f_{+-}/f_{00} using the ratio of B lifetimes $\tau_{B^-}/\tau_{\bar{B}^0} = 1.06 \pm 0.04$. We obtain

$$\frac{f_{+-}\tau_{B^-}}{f_{00}\tau_{\bar{B}^0}} = \frac{\mathcal{B}(B^- \to D^{*0}\ell^-\bar{\nu})}{\mathcal{B}(\bar{B}^0 \to D^{*+}\ell^-\bar{\nu})} = 0.976 \pm 0.12, \tag{4.9}$$

which leads to the result

$$\frac{f_{+-}}{f_{00}} = 0.92 \pm 0.12. \tag{4.10}$$

Chapter 5 Fitting Method

5.1 Fit Variables

To measure the form factors, we use the full four-dimensional distribution given in Equation 2.9 to make use of all the information in the decay. We fit over the four independent variables q^2, $\cos\theta_\ell$, $\cos\theta^*$, and χ which describe the decay. These variables have been defined in Figure 2.1.

The variables q^2, $\cos\theta_\ell$, $\cos\theta^*$, and χ used in Equation 2.9 are defined in the B rest frame. These variables are measured in the lab frame where the B has a momentum of approximately 340 MeV/c which corresponds to $\beta \approx 0.06$. As a result, the measured variables have a loss of resolution due to the motion of the B, as well as measurement error. For example, $q^2 = (P_B - P_{D^*})^2 = m_B^2 + m_{D^*}^2 - 2E_B E_{D*} + 2|\vec{p}_B||\vec{p}_{D^*}|\cos\theta_{BD^*}$. With the B direction unknown, the loss of resolution on q^2 is given by $2|\vec{p}_B||\vec{p}_{D^*}|\cos\theta_{BD^*}$. For $q^2 = 0$, this can be as much as $\pm$ 1.5 GeV$^2/c^4$, and can result in negative values of q^2.

Although the direction of the B is unknown, the angle between the B and the D^*l system is known, as shown in Figure 4.6 and Equation 4.1. Thus the B direction lies on a cone about the D^*l system direction and only the azimuthal angle is unknown. By choosing an azimuthal angle, one fixes the B direction and can then use that direction to boost into the B rest frame to calculate the variables of the decay. By doing this for two azimuthal angles that are 180 degrees apart, one can average the results obtained for the variables in the two B rest frames. The azimuthal angles chosen are the two which place the B direction closest to and furthest from the D^* direction. These two configurations give the largest and smallest q^2 values, as can be seen in the above formula. Using this average B direction method produces an unphysical peak at $\chi = 0$. As a result, the χ variable is only calculated in one configuration, the one in which the chosen B direction is furthest from the D^* direction. This "average B rest

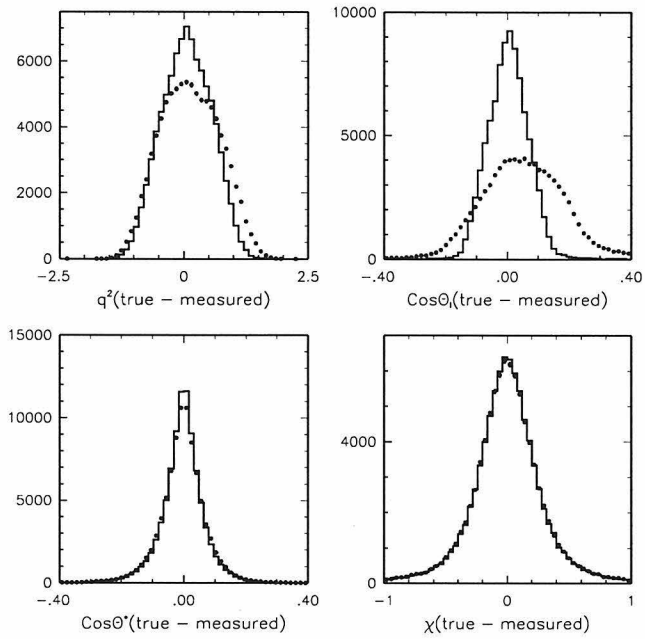


Figure 5.1: The solid line is the resolution on the kinematic variables using the "average B rest frame." The points show the resolution obtained assuming the B is at rest.

frame" method of calculating the variables for $\bar{B} \to D^* \ell^- \bar{\nu}$ decays was first described in [46]. Since the B mesons are produced with a $\sin^2\theta$ distribution with respect to the beam direction, one could reweight the chosen azimuthal angle according to this production angle. However, this procedure does not provide any further improvement in the resolution.

The improvement in resolution using the "average B rest frame," as compared to using the lab frame, is shown in Figure 5.1. There is a modest improvement in q^2, a significant improvement in $\cos\theta_\ell$, and no real difference for $\cos\theta^*$ or χ. For the $D^{*0}(K\pi)$ mode, the RMS resolutions are 0.44 GeV$^2/c^4$ for q^2, 0.06 for $\cos\theta_\ell$, 0.07 for $\cos\theta^*$, and 0.24 for χ. The part of the resolution just due to detector measurement error are 0.16 GeV$^2/c^4$ for q^2, 0.014 for $\cos\theta_\ell$, 0.07 for $\cos\theta^*$, and 0.15 for χ. The resolutions are not constant but depend on the measured value. Figure 5.2 plots the difference between the true and measured values as a function of the measured value.

The efficiency of the fit variables is best understood in terms of the D^* reconstruction and lepton selection efficiencies. Figure 5.3 plots the efficiency for each variable

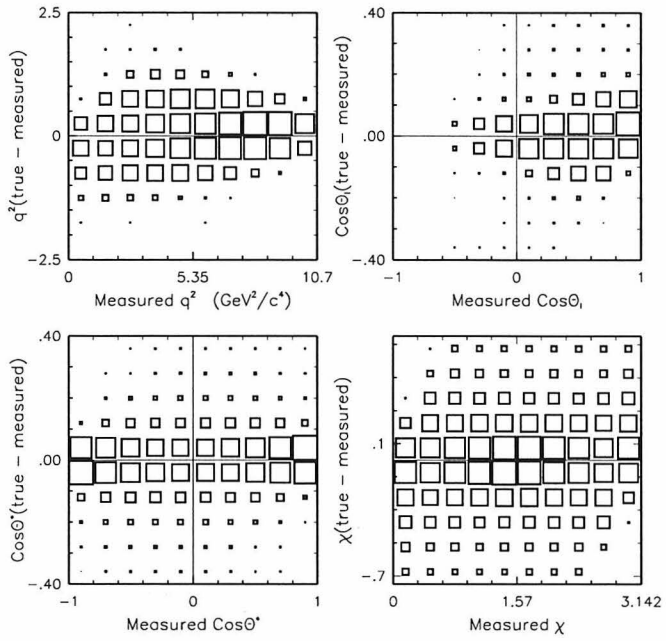


Figure 5.2: The difference between generated and measured values versus the measured value for each of the four kinematic variables. The distributions are from signal Monte Carlo for the mode $D^{*0}(K\pi)$.

for the different modes. The efficiency at large q^2 drops off significantly for D^{*+}'s, in contrast to D^{*0}'s. That is because large q^2 corresponds to low D^* momentum and as a result, a low momentum for the slow pion from the D^* decay. The charged slow pion curls up inside the large magnetic field of the detector and is not detected below approximately 50 MeV/c. In contrast, a π° at rest produces two photons with energies of 67 MeV, which are well above the minimum photon energy requirement of 30 MeV. The efficiency of the muon modes at smaller q^2 values is lower than for electrons. This is a result of the higher cut on the lepton momentum for muons, which preferentially selects the part of phase space with higher q^2.

The efficiency shape for $\cos\theta_\ell$ and the difference in efficiency for electrons and muons is simply understood in terms of the lepton momentum cut. The lepton energy, in the B rest frame, is given by

$$E_\ell = \frac{P_{D^*}\cos\theta_\ell}{2} + \frac{m_B^2 + q^2 - m_{D^*}^2}{4m_B}. \tag{5.1}$$

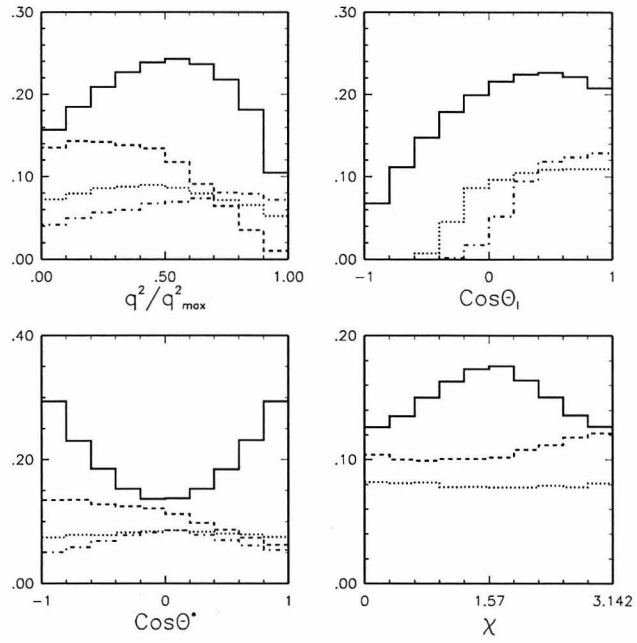


Figure 5.3: We plot the efficiency as a function of the kinematic variables, and compare different modes. The solid line is the generated MC distribution before any efficiency effects, which we plot with an arbitrary normalization. The other lines are the efficiency which is given on the vertical axis. The dashed line is $D^{*+}(K\pi)$ electrons, the dotted line $D^{*0}(K\pi)$ electrons, and the dashed-dotted line is $D^{*0}(K\pi)$ muons.

Negative values of $\cos\theta_\ell$ directly correspond to low lepton energy, and the lower lepton momentum cut for electrons accepts lower values of $\cos\theta_\ell$.

Figure 5.3c shows a dropoff in efficiency for large values of $\cos\theta^*$ for D^{*+}'s, which is again due to the slow pion. Positive values of $\cos\theta^*$ correspond to the D^0 being boosted along the D^* direction, and thus the slow pion, which is in the opposite direction, is boosted to a lower momentum in the lab frame. This scenario is especially true for small values of q^2 where the D^* has maximum momentum. This creates an asymmetry for the measured decay angle. The $\cos\theta^*$ efficiency for D^{*0}'s, which does not have low momentum charged tracks, is symmetric. The muon modes show a larger dropoff in efficiency, than electrons, for both large positive and negative values of $\cos\theta^*$. This again is due to the difference in lepton momentum cuts selecting phase space differently. The efficiency for the variable χ is approximately flat.

5.2 Fit Technique

The measured four-dimensional distribution can be written as the generated distribution, given by Equation 2.9, times an efficiency function and convoluted with a smearing function.

$$F(\vec{x}', \vec{\alpha}) = \int dx F(\vec{x}, \vec{\alpha}) G(\vec{x}, \vec{x}') \epsilon(\vec{x}) \tag{5.2}$$

where $\vec{x}$ and $\vec{x}'$ are the generated and measured kinematic variables, $\vec{\alpha}$ are the parameters we are fitting for, and $G(\vec{x}, \vec{x}')$ and $\epsilon(\vec{x})$ are the smearing and efficiency functions. $G(\vec{x}, \vec{x}')$ describes the smearing due to both the B motion and the detector response.

Since it would be difficult to obtain analytic forms for $G(\vec{x}, \vec{x}')$ and $\epsilon(\vec{x})$, we use the weighted Monte Carlo technique to perform an unbinned maximum likelihood fit [19, 58]. With this technique we generate a large number of signal Monte Carlo events with the full detector simulation and apply the data analysis to them. This gives a distribution of events with the correct smearing and efficiency and for which we know $\vec{x}$, $\vec{x}'$, and $\vec{\alpha}$. For each Monte Carlo event we compute a weight, $W_{MC}(\vec{\alpha}) = d\Gamma(\vec{x}, \vec{\alpha})/d\Gamma(\vec{x}, \vec{\alpha}_0)$, for any value of $\vec{\alpha}$, where $\vec{\alpha}_0$ are the values used to generate the Monte Carlo and $d\Gamma(\vec{x}, \vec{\alpha})$ is the distribution as given in Equation 2.9. We compute the likelihood for a given data event by adding up the weights of the Monte Carlo events which are inside some volume, V, centered on the data event in the four-dimensional space. Background events do not depend on the parameters $\vec{\alpha}$ and so always have a constant weight, W_{Bkgd_i}. In principle, for a given type of background, we can set $W_{Bkgd_i} = 1$ for each background MC event. However, as described in section 5.3, each category of background may be composed of several MC samples for several different modes. In this case, the value of the background weight is chosen according to the number of MC events generated for each specific decay mode. For example, there are four modes for the D^{**} class of background, and the relative weights between the modes depends on their branching ratios and the number of events generated for that mode. We define $W_{Bkgd_i} = \mathcal{B}(Mode)/N_{MC}$, where B(Mode) is the branching ratio for that mode, and N_{MC} is the number of MC events generated for that mode.

The background weight can also be a function of a kinematic variable, in order to change, for example, the efficiency distribution for that background. This type of reweighting is used for studying systematic effects. The determination of the number of background events in the data is described in section 4.2 and the relative fraction of a background type is $f_{Bkgd_i} = N_{Bkgd_i}/N_{events}$. The likelihood function is written as

$$\mathcal{L}(\vec{\alpha}) = \prod_{events} \left\{ (1 - f_{Bkgd}) \frac{\sum_{vol} W_{MC}(\vec{\alpha})}{V \times \sum_{MC} W_{MC}(\vec{\alpha})} + \sum_i [f_{Bkgd_i} \frac{\sum_{vol} W_{Bkgd_i}}{V \times \sum_{Bkgd_i} W_{Bkgd_i}}] \right\}, \tag{5.3}$$

and the parameters are estimated by minimizing $-\log \mathcal{L}$. As shown, the likelihood is normalized for the MC events by dividing by the sum of all the MC events. For the signal MC, this sum is performed each iteration of the fit since the parameter values change. We normalize the total of the signal MC plus all the background MC samples by setting $f_{Bkgd} = \sum_i f_{Bkgd_i}$. The volume size, V, is calculated for each data point. In general, the same volume size is used for each data point, although points near the boundary of phase space will have a smaller volume.

The parameters $\vec{\alpha}$ we actually fit for are the ratio of form factors R_1 and R_2 as given in equations 2.27 and 2.28, as well as the parameter $\rho^2_{A_1}$ of equation 2.24 which characterizes the q^2 dependence of the form factors. We also fit for these parameters using alternative forms for the q^2 dependence.

The volume is a cube in four dimensions, centered around each data point. The length of the volume sides are 1.2 GeV$^2/c^4$for q^2, 0.4 for $\cos\theta_\ell$, 0.24 for $\cos\theta^*$ and 0.94 for χ. This gives a volume that is 0.08% of the total kinematic space. In cases where the data point is closer to a phase space boundary than a distance of half a bin size, the volume, V, is reduced by the difference in length between half a bin size and the distance to the boundary. In these cases the data point is no longer centered inside the volume. In general, if the function is non-linear across the volume, the function is not evaluated at the center of the bin which can lead to systematic offsets in the fit results. This effect is described in greater detail in section 7.2.1. However, too small a volume results in too few Monte Carlo events inside the volume leading to an increased uncertainty in the value of the function. We choose an intermediate

size volume and evaluate the systematic error for both the volume size and Monte Carlo statistics.

5.3 Fit Backgrounds

Of the backgrounds discussed in section 4.2 those included in the fit are the combinatoric, correlated(D^{**}), and uncorrelated backgrounds. Continuum and fake lepton backgrounds are negligible as shown in Tables 4.5 – 4.7. The sizes of the backgrounds are determined from the data as described in section 4.2. However, there are not enough events in the data, such as in the δm sideband for combinatoric background, to describe the shape of the background in the four-dimensional kinematic space. We rely on background Monte Carlo events to determine the shape of the background in the fit.

The analysis was run on a sample of "generic" $B\bar{B}$ MC (which contains B decays to all expected modes), with statistics comparable to that in the data, and the background sources were classified. For the $D^{*0}(K\pi)$ mode, the combinatoric background is predominantly from $b \to cl\nu$ decays, with less than 4% of the total combinatoric background coming from events where the lepton does not come directly from a b quark decay, e.g., $b \to c \to s\ell\nu$. Each source of $b \to cl\nu$ background was generated separately in order to improve the efficiency of selecting background events. In the fit each combinatoric background source is weighted, relative to the others, according to the ratio of the known or estimated branching fraction to the number of events generated. The total normalization of the combinatoric background in the fit is that determined from the data in section 4.2.1.

For the mode $D^{*0}(K\pi)$, we find from MC that 40% of the combinatoric background is from $\bar{B}^0 \to D^{*+}\ell^-\bar{\nu}$ and $B^- \to D^{*0}\ell^-\bar{\nu}$ events where the D^0 is correctly reconstructed, but the π° candidate is not from the D^*, which is either a D^{*+} or a D^{*0}. The π° candidate can be a true π° from another source, or a random combination of two photons that pass the π° selection criteria. This background is most like the signal, since its source is signal events. These decays depend on the parameters

we are fitting for; however, their weights in the fit are not taken to be functions of the parameters. This class of background is modeled using the large samples of GEANT based CLEOG Monte Carlo that were already generated for signal events. I refer to this sample as the CLEOG combinatoric background and it is treated independently of the other combinatoric backgrounds in the fit. The last two plots in Figure 5.4 show the δm distribution for these two background modes. For $B^- \to D^{*0}\ell^-\bar{\nu}$, there are cases where the π° candidate has one photon which is from the right π°. In this case the background will peak in the δm signal region. However, the peaking in Figure 5.4 is primarily due to the δm variable being used in the χ^2 which selects one entry per event for these plots.

The other 60% of the combinatoric background is from fake D^0's or real D^0's from sources other than the two mentioned above. This class of background is modeled using a sample of fast TRKSIM Monte Carlo electron events, where each major B semileptonic decay mode has been generated. The TRKSIM Monte Carlo does not give accurate absolute efficiencies, but the relative efficiency between modes is consistent. We compare the shape of the MC distributions with data in section 7.3.2, and find good agreement. The first nine plots of Figure 5.4 show the δm distribution for modes generated using TRKSIM. This sample of electron MC events is also used to model the muon background by reweighting the events according to the relative lepton id efficiency between electrons and muons. This ratio of efficiencies is obtained using the lepton identification efficiencies from the CLEOG Monte Carlo, and is evaluated as a function of lepton momentum. Figure 7.2 plots the electron and muon efficiencies as a function of momentum. Only MC events from the δm signal region are used to model the background in the fit. Figure 5.5 shows the contribution of the CLEOG and TRKSIM Monte Carlo samples to the δm distribution of the combinatoric background.

The combinatoric background for the mode $D^{*0}(K\pi\pi^\circ)$ is quite large due to the presence of 2 π°'s in the decay. For this mode, there is only a CLEOG MC sample for the mode $B^- \to D^{*0}\ell^-\bar{\nu}$ with $D^0 \to K^-\pi^+\pi^\circ$, where the D^0 is correctly reconstructed. This constitutes 18% of the combinatoric background. The other combinatoric back-

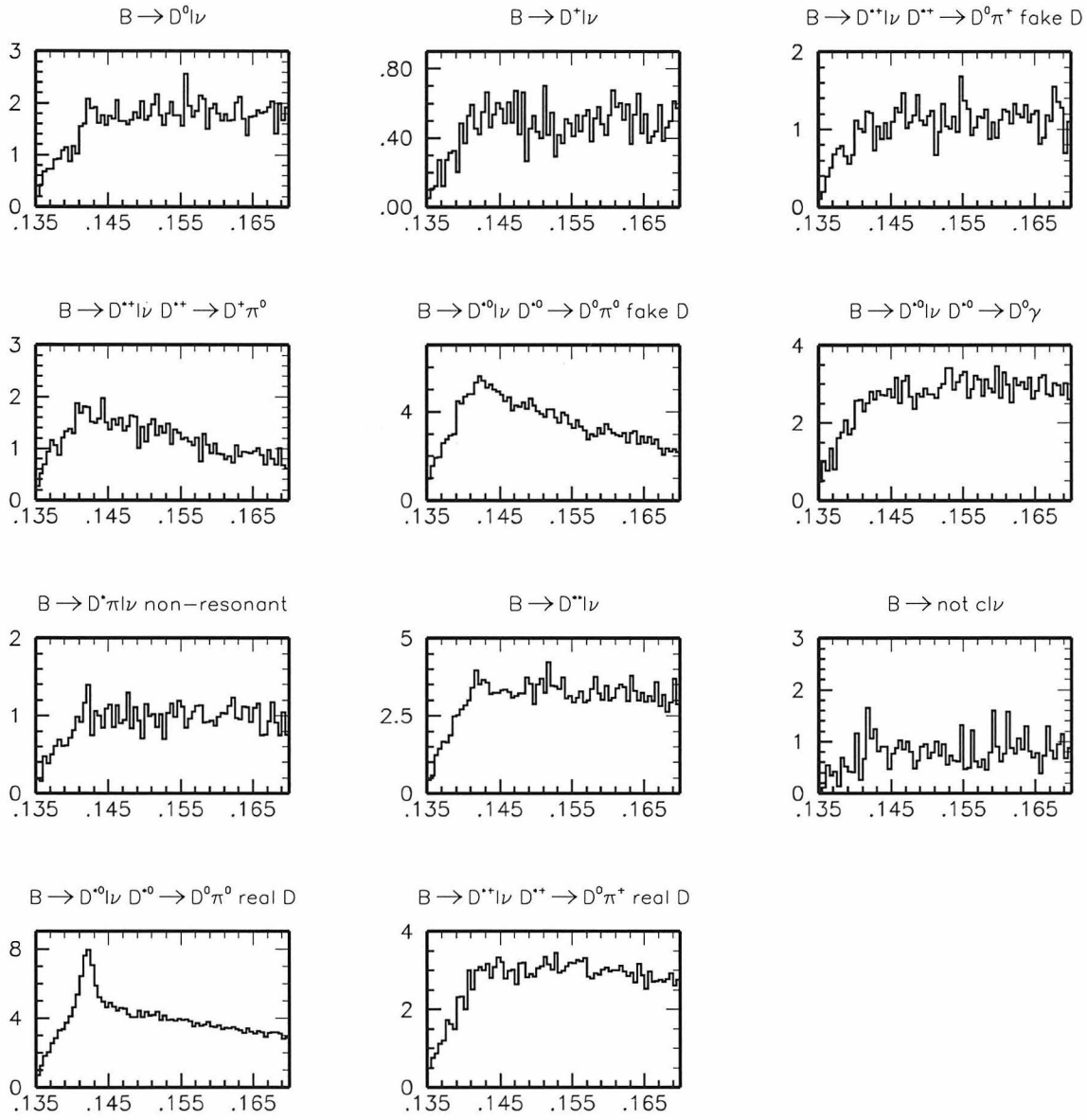


Figure 5.4: $D^{*0}(K\pi)$: The distributions in δm for the MC samples of combinatoric background. The normalization is that predicted from branching ratios. The first nine samples are TRKSIM MC and the last two are CLEOG MC.

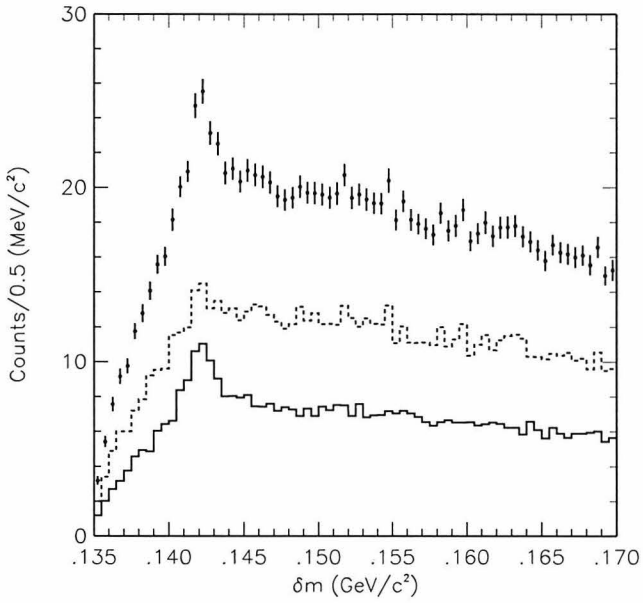


Figure 5.5: $D^{*0}(K\pi)$: The distribution in δm for the MC sample of combinatoric background. The solid line is the CLEOG sample of real D^0events and the dashed is the contribution from the TRKSIM sample. The points are the sum of the two.

ground is modeled using TRKSIM MC samples, where again the electron MC is reweighted in the fit for muons. The δm distribution for each of these background modes is shown in Figure 5.6.

The $D^{*+}(K\pi)$ combinatoric background is significantly less than in the other two modes, because there is no contribution due to combinatoric fake π^0's. This background is modeled using a sample of TRKSIM Monte Carlo, without a separate CLEOG sample for backgrounds from signal decays. The contributions from each source are shown in Figure 5.7.

The correlated background is modeled using a sample of TRKSIM MC events for each D^{**} mode plus a $D^*\pi$ non-resonant sample. The normalization of this background in the fit is that given in Table 5.2. We use the ISGW2 model for generating the resonant states and the Goity-Roberts model for the non-resonant. The same MC events are used for both the $D^0 \to K^-\pi^+$ and $D^0 \to K^-\pi^+\pi^0$ modes for $B^- \to D^{*0}\ell^-\bar{\nu}$. The same sample of events is also used for the correlated muon background, but the events are reweighted as a function of lepton energy, according to the ratio of muon to electron efficiencies.

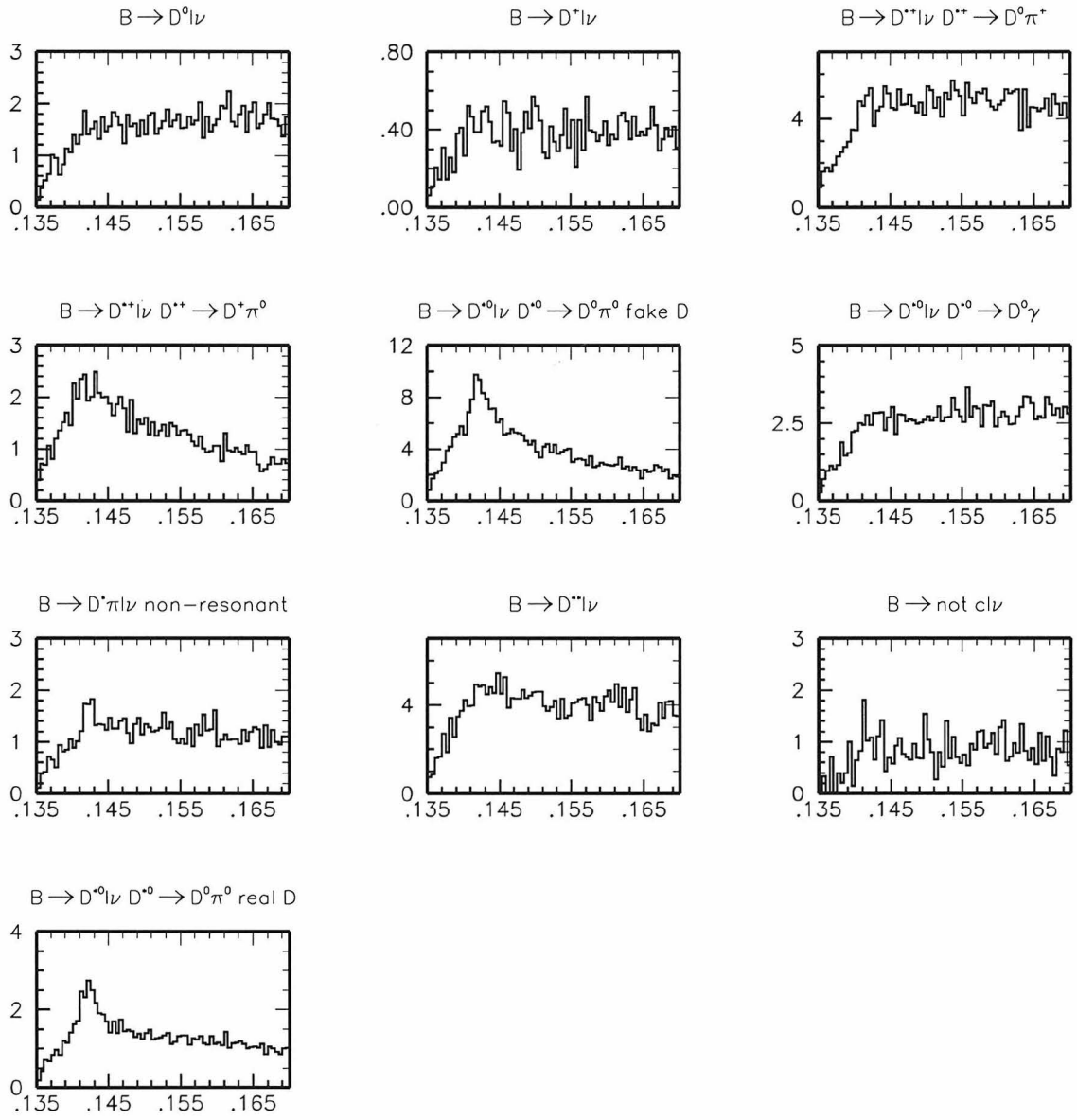


Figure 5.6: $D^{*0}(K\pi\pi^{\circ})$: The distributions in δm for the MC samples of combinatoric background. The normalization is that predicted from branching ratios. The last histogram is the CLEOG sample.

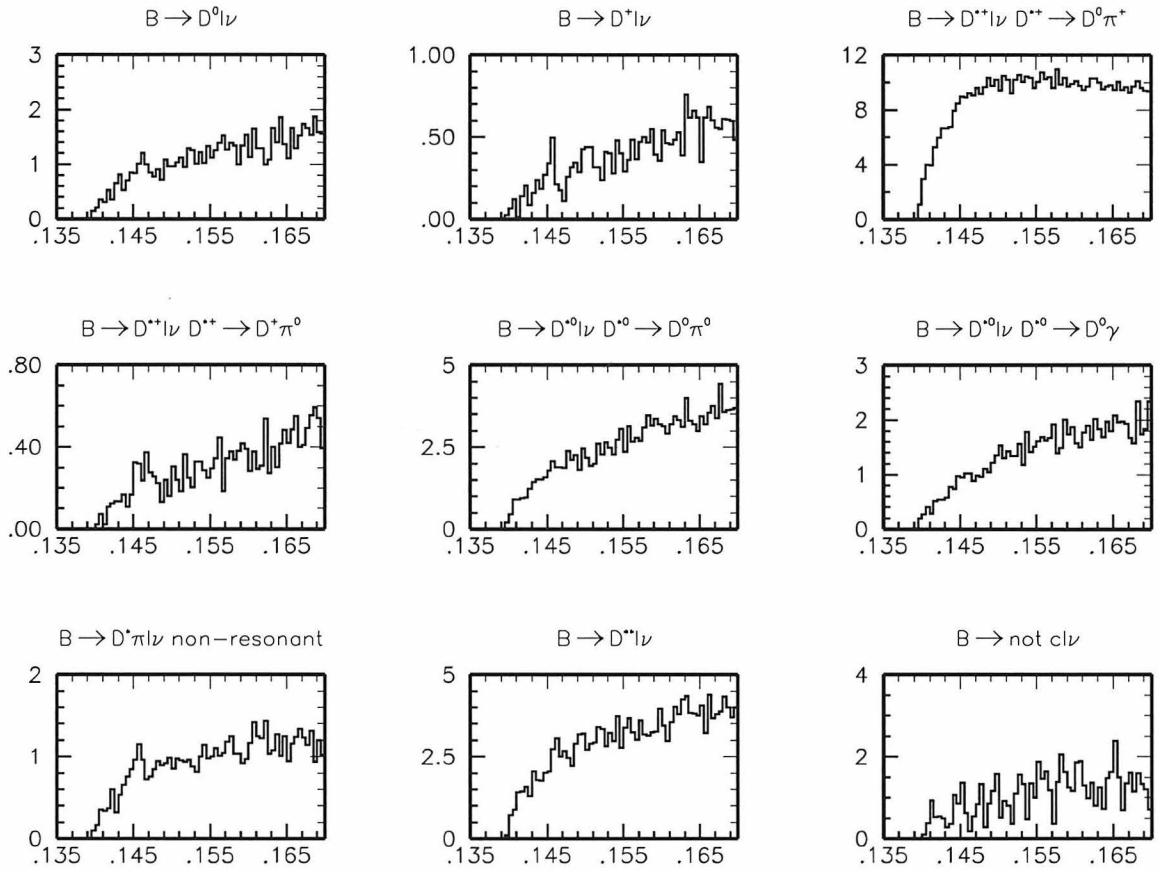


Figure 5.7: $D^{*+}(K\pi)$: The distributions in δm for the MC samples of combinatoric background. The normalization is that predicted from branching ratios.

Mode	Branching Ratio
$B^- \to D^0 \ell\nu$	1.8%
$\bar{B}^0 \to D^+ \ell\nu$	1.8%
$\bar{B}^0 \to D^{*+} \ell\nu (D^{*+} \to D^0 \pi^+)$	$4.49\% \times 68.1\%$
$\bar{B}^0 \to D^{*+} \ell\nu (D^{*+} \to D^+ \pi^\circ)$	$4.49\% \times 30.8\%$
$B^- \to D^{*0} \ell\nu (D^{*0} \to D^0 \pi^\circ)$	$5.13\% \times 63.6\%$
$B^- \to D^{*0} \ell\nu (D^{*0} \to D^0 \gamma)$	$5.13\% \times 36.4\%$
$B \to D\pi\ell\nu$ non-resonant	$2 \times 1.3\%$
$B \to D^{**} \ell\nu$	$2 \times 2.4\%$

Table 5.1: The branching ratios used for weighting the individual combinatoric background modes in the fit. These are only for combinatoric MC events, where there is not a reconstructed D^*.

The uncorrelated background is modeled with a sample of TRKSIM generic $B\bar{B}$ electron Monte Carlo where the D^* and electron are tagged as coming from opposite B's. The normalization of the background is that obtained from the data, as discussed in section 4.2.3 and is different for electrons and muons. The same events are used for both the $D^0 \to K^-\pi^+$ and $D^0 \to K^-\pi^+\pi^\circ$ modes for $B^- \to D^{*0}\ell^-\bar{\nu}$. This background fraction for the $D^{*0}(K\pi\pi^\circ)$ mode is obtained by scaling the background fraction for the $D^{*0}(K\pi)$ mode. That is because the large combinatoric background and low efficiency make it difficult to reliably measure this background in the data. Table 5.2 gives the background fractions used in the fit.

Figure 5.8 plots the number of MC events of each type in the volume around a data point. If there is less than three total MC events in the volume, the event is not used in the fit. This condition is only met for four events.

Mode	Combinatoric	Correlated	Uncorrelated	Total Fraction
$D^{*+}(K\pi)$ e	0.12	0.050	0.013	0.183
$D^{*+}(K\pi)$ μ	0.12	0.073	0.0	0.193
$D^{*0}(K\pi)$ e	0.34	0.045	0.014	0.399
$D^{*0}(K\pi)$ μ	0.34	0.051	0.0	0.391
$D^{*0}(K\pi\pi^\circ)$ e	0.46	0.035	0.012	0.507
$D^{*0}(K\pi\pi^\circ)$ μ	0.46	0.047	0.0	0.507

Table 5.2: The background fractions in the fit.

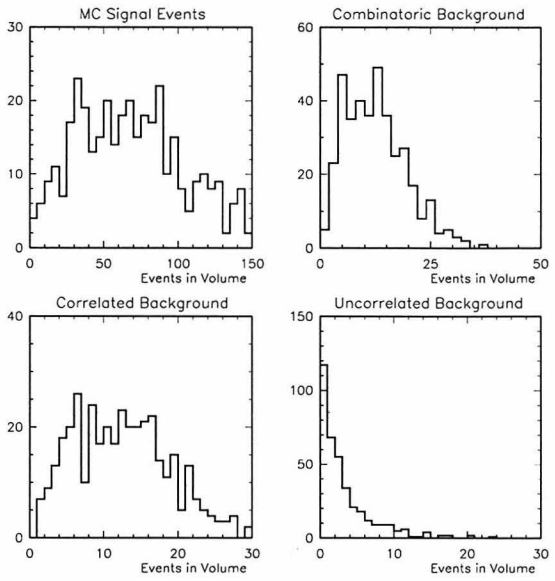


Figure 5.8: $D^{*0}(K\pi)$: The number of MC signal and background events inside the volume around each data point. The other modes have similar distributions.

5.4 Information and Minimum Error

For a normalized probability distribution $P(x, \alpha)$ with random variable x and parameter α, one can define the Fisher information number I for the parameter α as [59]

$$\begin{aligned} I(\alpha) &= \text{Variance}\left(\frac{\partial}{\partial\alpha}\ln P(x,\alpha)\right) \\ &= \int\left(\frac{\partial P}{\partial\alpha}\right)^2\frac{1}{P}d\vec{x}. \end{aligned} \tag{5.4}$$

This is the information for one event, and the information for n events is simply $nI(\alpha)$, assuming each event is independent and identically distributed.

For an estimator $\hat{\alpha}$ for α, the variance of $\hat{\alpha}$ has a lower bound given by

$$\sigma^2(\hat{\alpha}) \geq \frac{[1+\frac{\partial b_{\hat{\alpha}}(\alpha)}{\partial\alpha}]^2}{nI(\alpha)}, \tag{5.5}$$

where $b_{\hat{\alpha}}(\alpha)$ is the bias for $\hat{\alpha}$, and n is the number of events. This inequality is referred to as the Rao-Cramer-Frechet bound [59]. The bias is unknown a priori, and we will asssume that the estimators are unbiased.

For a probability distribution $P(\vec{x},\vec{\alpha})$ of several parameters, there is an information matrix

$$I_{ij}(\vec{\alpha}) = \int \left(\frac{\partial P}{\partial \alpha_i}\frac{\partial P}{\partial \alpha_j}\right)\frac{1}{P}d\vec{x}. \tag{5.6}$$

The bound is now a covariance matrix given by

$$\sigma_{ij}^2 \geq \frac{|I(\alpha)|_{ij}^{-1}}{n}, \tag{5.7}$$

which includes the correlations between the parameters.

Calculating the information gives the smallest error expected, assuming the estimator is efficient. Plotting the function inside the integral of Equation 5.4 shows which parts of phase space contain the most information. For the function $F(\vec{x},\vec{\alpha})$ given in Equation 2.9, we calculate the probability function

$$P(\vec{x},\vec{\alpha}) = \frac{F(\vec{x},\vec{\alpha})}{\int F(\vec{x},\vec{\alpha})d\vec{x}}. \tag{5.8}$$

We calculate the information matrix for this probability distribution for the three parameters R_1, R_2 and $\rho^2_{A_1}$. Table 5.3 gives the minimum error and correlations for the three parameter values measured in this thesis. We also show the actual error results from the fit of the data. The actual error and correlations are substantially larger, due to the presence of background and the loss of efficiency in sensitive areas of phase space, as discussed below.

We plot the one-dimensional projections of $(\frac{\partial P}{\partial \alpha})^2\frac{1}{P}$ for the three parameters in Figure 5.9. Figures 5.11 and 5.12 plot the two-dimensional information projections for the R_1 and R_2 parameters. It is instructive to compare where the information is maximum for a parameter, with the differential distributions in Figures 2.2 and 2.3, which show where the events are most likely to be. The maximum information on R_1 is at intermediate q^2 values, and peaks at large positive and negative values of $\cos\theta_\ell$. The large peak in information at negative values of $\cos\theta_\ell$ is significant, because the lower lepton momentum cut removes the events in that region as shown in Figure 5.3. This leads to a larger error on R_1. The information on R_2 is maximum for small q^2

values and large positive and negative values of $\cos\theta^*$. The slope parameter $\rho^2_{A_1}$ is only measured by the q^2 distribution, and its information is maximum for small and large values of q^2.

The loss due to acceptance and cuts not only reduces the total number of events, but can give a larger error depending on where the loss of efficiency results. However, since cuts are usually determined by the detector response and backgrounds, the placement of a cut may be unavoidable. The presence of backgrounds has the effect of increasing the size of the denominator in Equation 5.4, while not contributing to the numerator which depends on the physics parameters. This results in a smaller information number and a larger error. However, cutting to remove background may remove a sensitive part of phase space. Although the information gives the minimum statistical error, it does not determine the systematic error, which may determine the measurement precision.

As shown in Equation 5.6, the error on the parameter estimation depends on the value of the parameter. Figure 5.10 illustrates this point by plotting the minimum error expected as a function of the three parameters. This dependence has important implications for comparing the results of different experiments.

	Generated Function	Fit Result
$\sqrt{n}\sigma_{R_1}$	3.51	11.6
$\sqrt{n}\sigma_{R_2}$	3.90	8.17
$\sqrt{n}\sigma_{\rho^2}$	3.63	6.20
$C_{R_1R_2}$	-0.40	-0.79
$C_{R_1\rho^2}$	0.32	0.60
$C_{R_2\rho^2}$	-0.79	-0.82

Table 5.3: The minimum error and correlations expected for the decay distribution, and the measured errors.

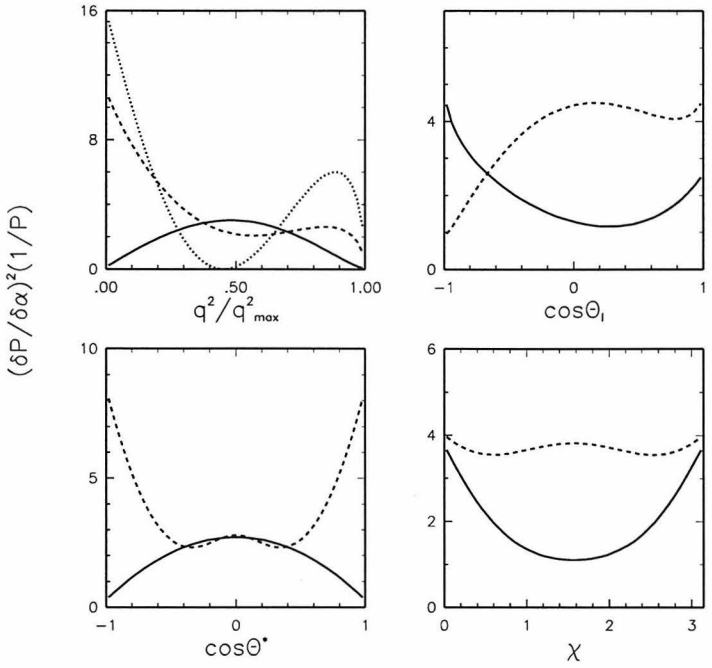


Figure 5.9: The information projected onto the fit variables, for the fit parameters. The solid line is for R_1, the dashed line is for R_2, and the dotted line is for $\rho^2_{A_1}$.

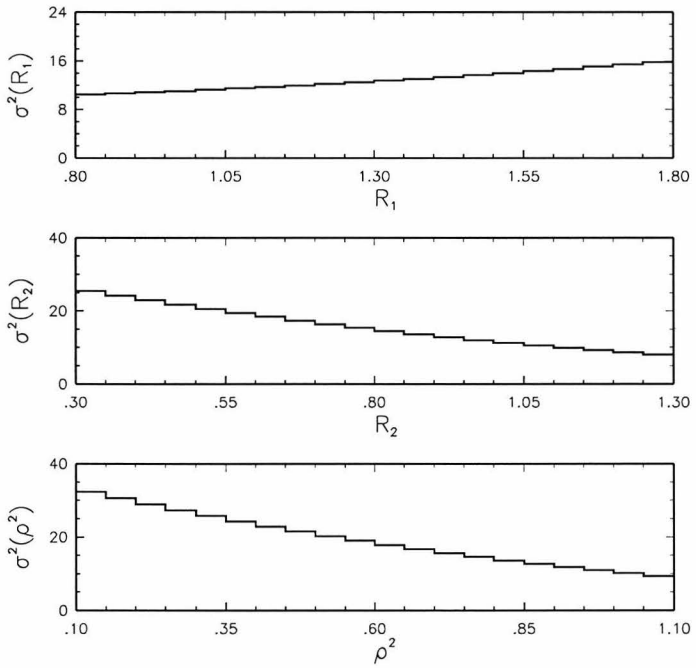


Figure 5.10: The minimum error expected is plotted as a function of the fit parameter for an arbitrary parameter range.

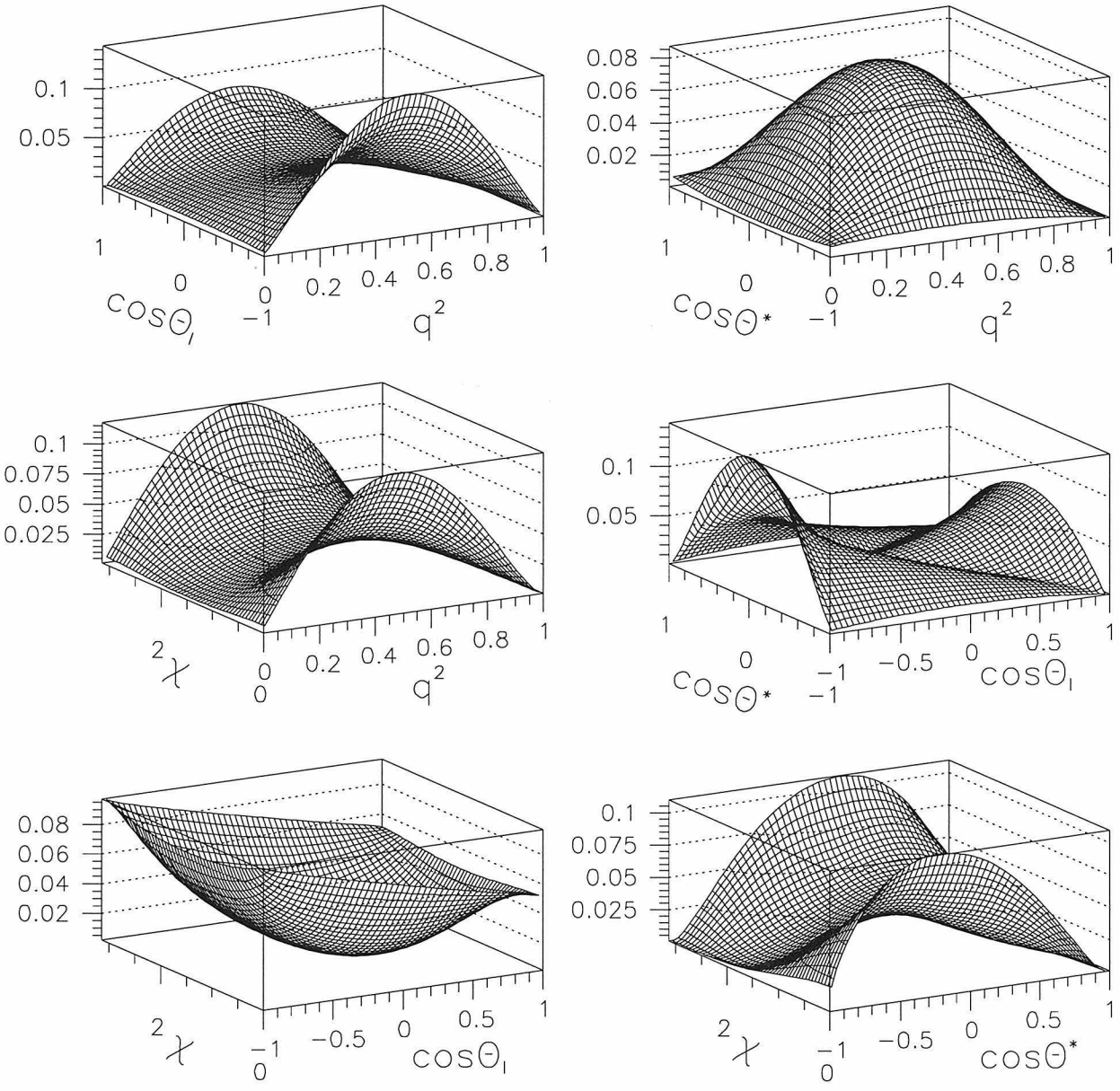


Figure 5.11: The information on R_1 for two-dimensional projections of the kinematic variables.

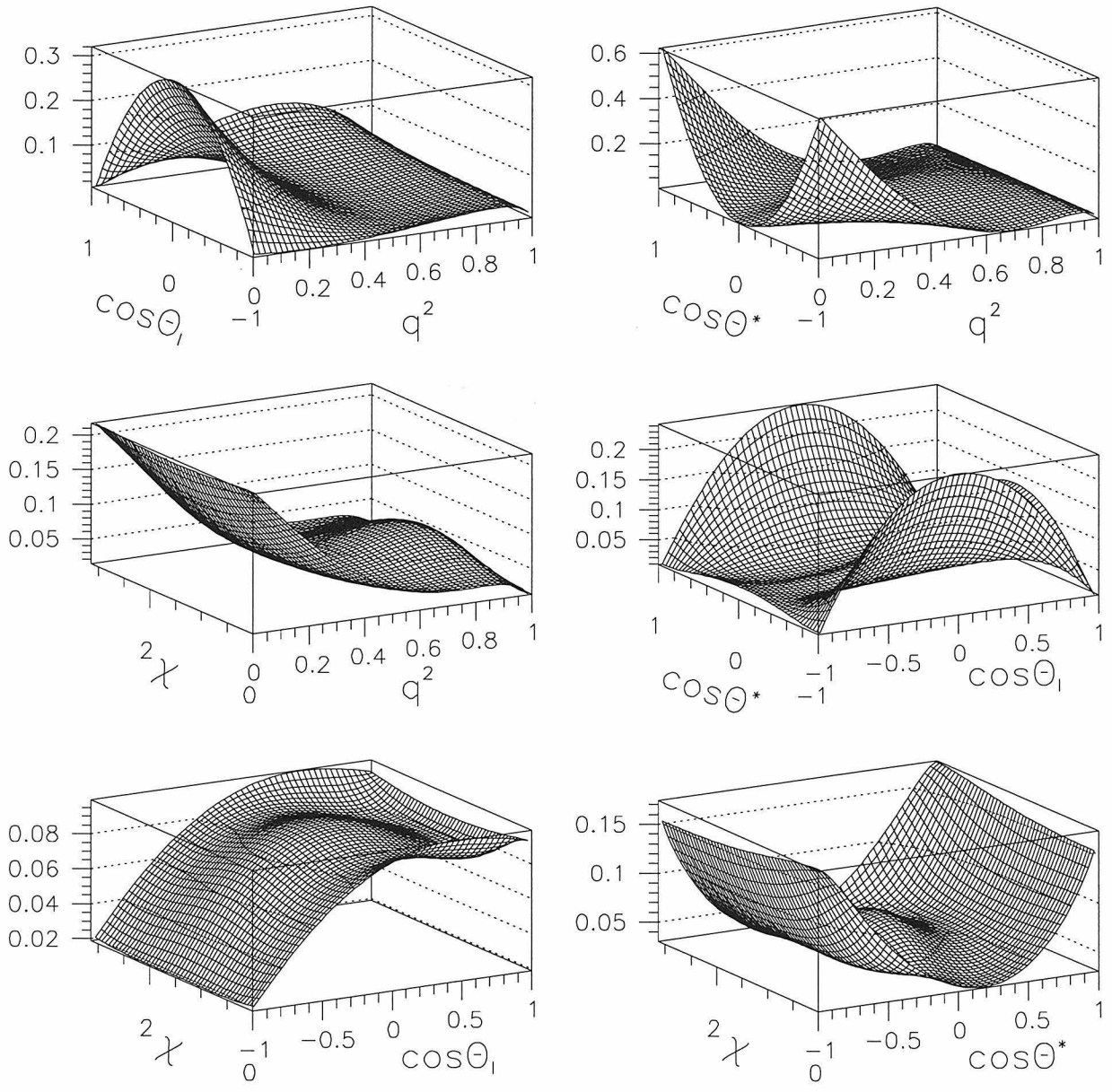


Figure 5.12: The information on R_2 for two-dimensional projections of the kinematic variables.

Chapter 6 Fit Results

6.1 Standard Fit Results

We fit for the ratio of form factors R_1 and R_2 and the slope, $\rho^2_{A_1}$, of the A_1 form factor. We fit the modes $B^- \to D^{*0}\ell^-\bar{\nu}$ with $D^{*0}(K\pi)$ and $D^{*0}(K\pi\pi^\circ)$, and $\bar{B}^0 \to D^{*+}\ell^-\bar{\nu}$ with $D^{*+}(K\pi)$, both separately and combined. Since electrons and muons are treated separately in the fit, the combined fit is a simultaneous fit to six different modes. The results for these fits are given in Tables 6.1 and 6.2, including the correlations between the parameters which are quite large. The combined fit result is $R_1 = 1.29 \pm 0.27$, $R_2 = 0.76 \pm 0.19$, and $\rho^2_{A_1} = 0.84 \pm 0.14$. The HQET expectations for these parameters are $R_1 \approx 1.3$ and $R_2 \approx 0.8$. The slope $\rho^2_{A_1}$ is not predicted by HQET but is expected to be in the range $0.4 < \rho^2_{A_1} < 1.3$ [32]. These predictions are supported by the fit results. Unless stated otherwise, subsequent discussions of fit results, and quantities derived from them will be for the combined fit result.

	$B^- \to D^{*0}\ell^-\bar{\nu}$	$\bar{B}^0 \to D^{*+}\ell^-\bar{\nu}$	Combined
R_1	1.48 ± 0.42	1.16 ± 0.35	1.29 ± 0.27
R_2	0.88 ± 0.26	0.65 ± 0.27	0.76 ± 0.19
$\rho^2_{A_1}$	0.72 ± 0.22	0.94 ± 0.18	0.84 ± 0.14
$C_{R_1R_2}$	-0.787	-0.769	-0.790
$C_{R_1\rho^2}$	0.610	0.566	0.599
$C_{R_2\rho^2}$	-0.812	-0.791	-0.820

Table 6.1: The fit results for the individual and combined fits. We also give the correlation coefficients for the fit parameters.

The data is compared with the fit in one-dimensional projections in Figures 6.1, 6.2, 6.3, and 6.4. Figures 6.5 and 6.6 show the two-dimensional projections of the combined fit and data. Figures 6.7 and 6.8 show plots of the shapes of the individual backgrounds in the electron modes.

	$D^{*0}(K\pi)$	$D^{*0}(K\pi\pi^0)$	Combined D^{*0}
R_1	1.49 ± 0.53	1.47 ± 0.70	1.48 ± 0.42
R_2	0.87 ± 0.33	0.89 ± 0.42	0.88 ± 0.26
$\rho^2_{A_1}$	0.83 ± 0.26	0.48 ± 0.44	0.72 ± 0.22
$C_{R_1 R_2}$	-0.800	-0.769	-0.787
$C_{R_1 \rho^2}$	0.635	0.566	0.610
$C_{R_2 \rho^2}$	-0.824	-0.791	-0.812

Table 6.2: The fit results for the individual D^{*0} fits. We also give the correlation coefficients for the fit parameters.

The two-dimensional projections illustrate the physics discussed in section 2.1.4, but it is more easily seen in one-dimensional projections of slices of the 2-d plots. Figure 6.9 shows plots of the $\cos\theta^*$ projection for small and large values of q^2. At small values of q^2, the distribution is more like a $\cos^2\theta$ distribution. This is expected since the H_0 amplitude dominates at low q^2. At high q^2, all three helicity amplitudes contribute more equally, as shown in Figure 2.4, and the $\cos\theta^*$ distribution is approximately flat. The asymmetry in the $\cos\theta^*$ distribution in Figure 6.9 is due to a decrease in efficiency for the D^{*+} mode at large $\cos\theta^*$. The plot of $\cos\theta^*$ versus χ also has an interesting structure, which we discuss in section 8.3.

6.2 Alternative Fitting Forms

The linear q^2 dependence given in Equation 2.22 is just the simplest way of parametrizing the q^2 dependence. The form of the q^2 dependence is unknown, but other forms suggested are given in Equation 2.23 and shown in Figure 2.6. The form factor ratios are also predicted to have a small q^2 dependence as discussed in section 2.3. Table 6.3 lists the fit results obtained using these alternative set of parametrizations. The fit results for the ratio of form factors do not change much when the q^2 dependence is changed. Similarly, the values of $R_1(q^2_{max})$ and $R_2(q^2_{max})$ do not change significantly when a slight q^2 dependence for the ratios of form factors is introduced. The log likelihoods are close for the different fits, with the largest change in log likelihood,

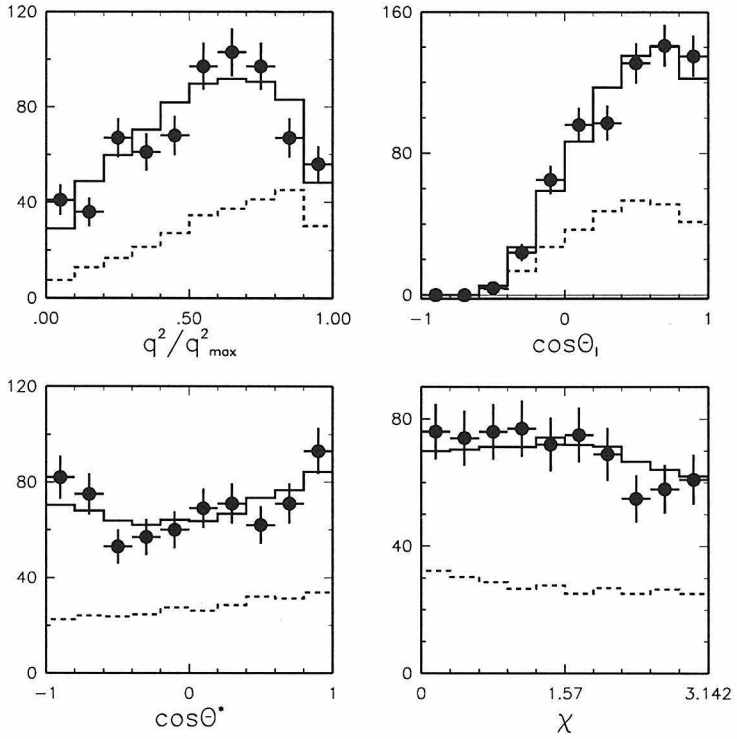


Figure 6.1: $D^{*0}(K\pi)$: Projections in each of the 4 fit variables. The points are the data, the solid line is the fit and the dashed line is the contribution from backgrounds.

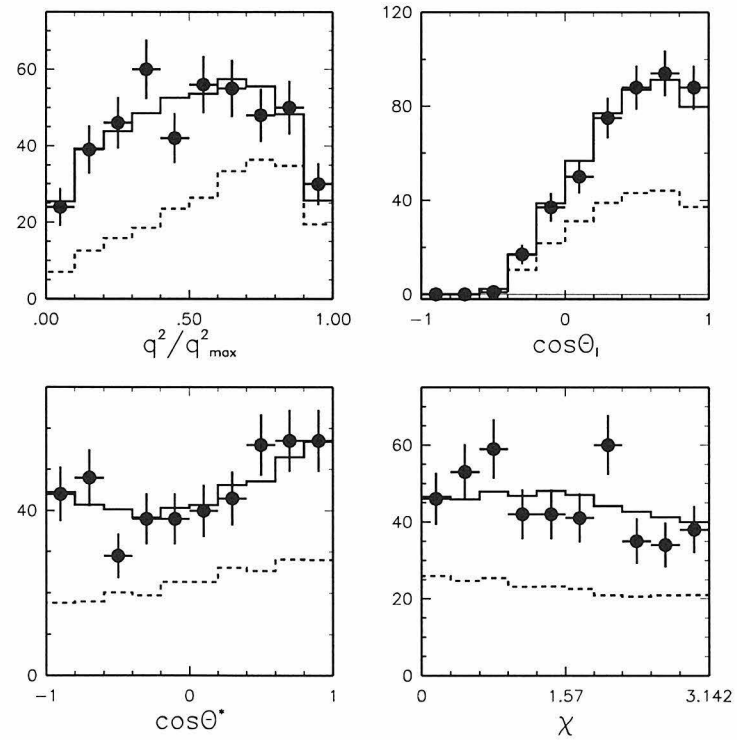


Figure 6.2: $D^{*0}(K\pi\pi^0)$: Projections in each of the 4 fit variables. The points are the data, the solid line is the fit, and the dashed line is the contribution from backgrounds.

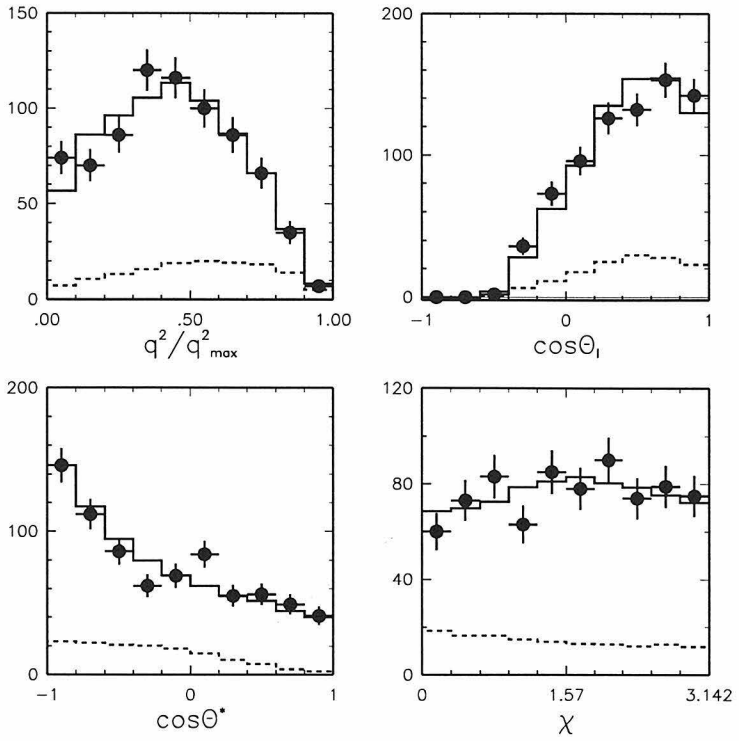


Figure 6.3: $D^{*+}(K\pi)$: Projections in each of the 4 fit variables. The points are the data, the solid line is the fit, and the dashed line is the contribution from backgrounds.

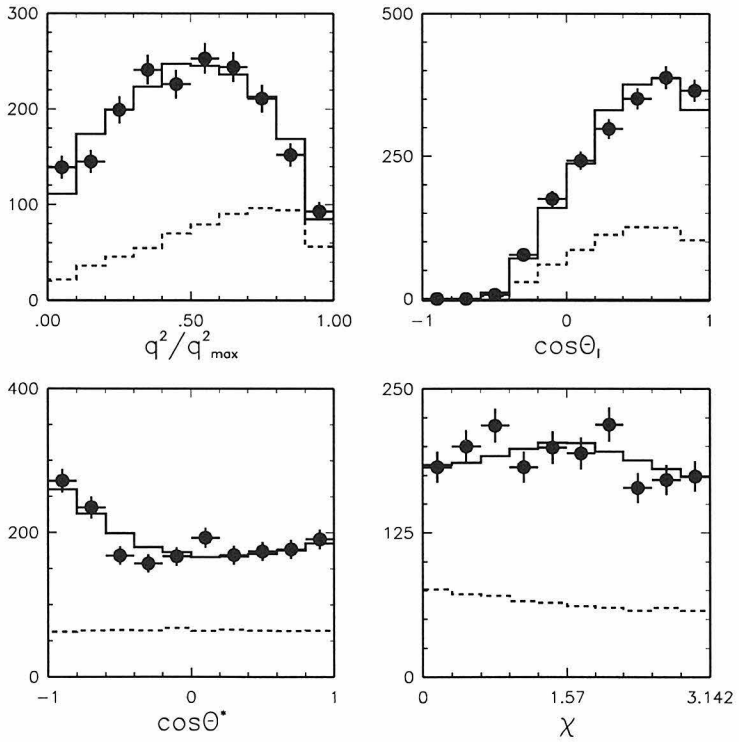


Figure 6.4: Combined: Projections in each of the 4 fit variables. The points are the data, the solid line is the fit and the dashed line is the contribution from backgrounds.

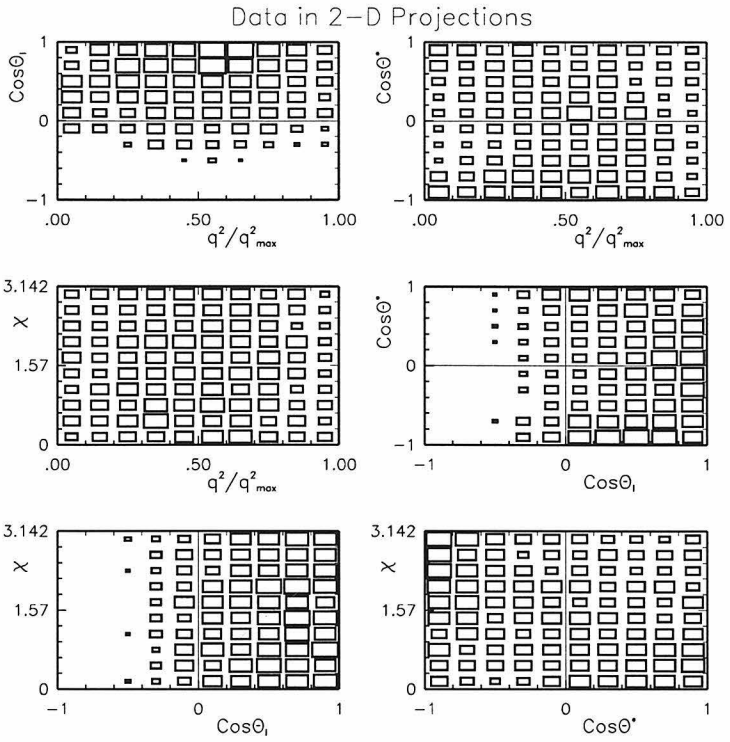


Figure 6.5: Two-dimensional projections of the the data.

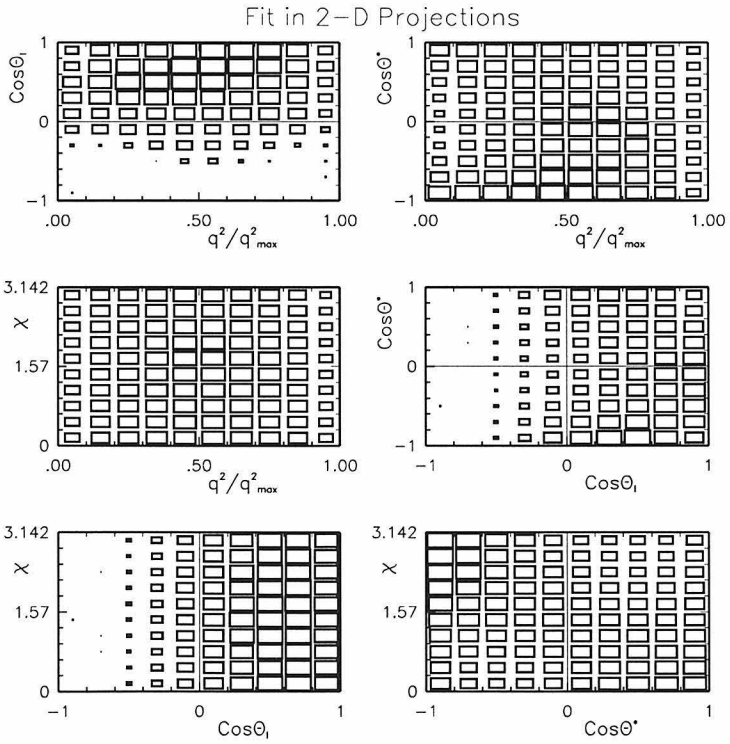


Figure 6.6: Two-dimensional projections of the fit result.

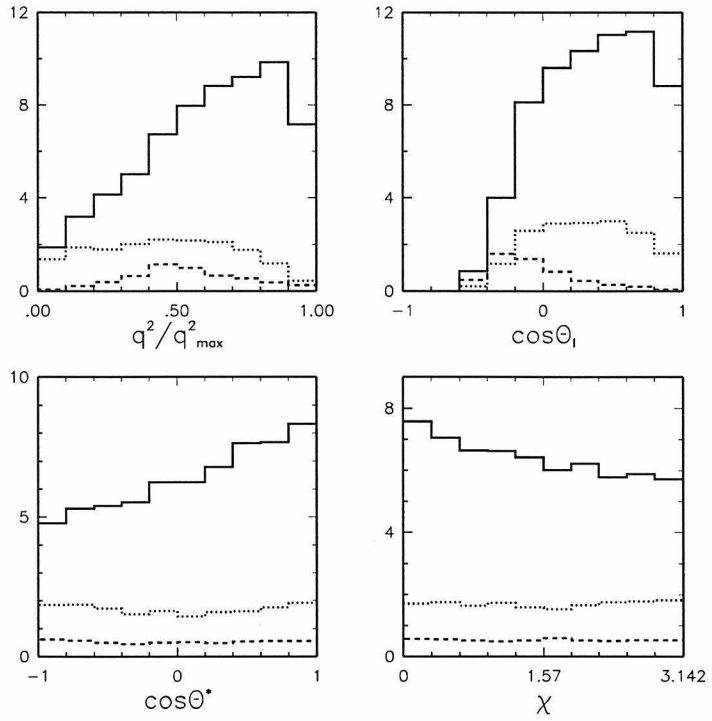


Figure 6.7: $D^{*0}(K\pi)$: Projections of each of the backgrounds. The solid line is the combinatoric background scaled by 0.5, the dotted line is the correlated background and the dashed line is the uncorrelated background.

relative to the usual fit, being only +0.262.

Section 2.4 gives the predictions of various models for the form factor ratios and the overall slope. Because the errors from the fit are not gaussian, one cannot simply compare the difference between the predicted and measured form factors. Instead we compare the log of the likelihood for the fit result, and when the model prediction is used for the form factors. For a 3 parameter fit, a change in $\ln\mathcal{L}$ of 0.5, which defines the 1σ errors, corresponds to a confidence level of 20%. The 95% confidence level is defined by the region for which $\Delta\ln\mathcal{L} \leq 3.91$. Table 6.4 gives the change in $\ln\mathcal{L}$ and corresponding confidence level for the different models. The $\Delta\ln\mathcal{L}$ is the difference between the $\ln\mathcal{L}$ which has been minimized in the standard HQET fit and the calculated $\ln\mathcal{L}$ when the parameters are fixed to the model predictions. Figures 6.10 and 6.11 show the 1σ and 95% confidence level contours for R_1 versus R_2, and R_2 versus $\rho^2_{A_1}$, when the third parameter is allowed to float in the fit.

Since HQET does not predict the q^2 dependence of the form factors, it is useful

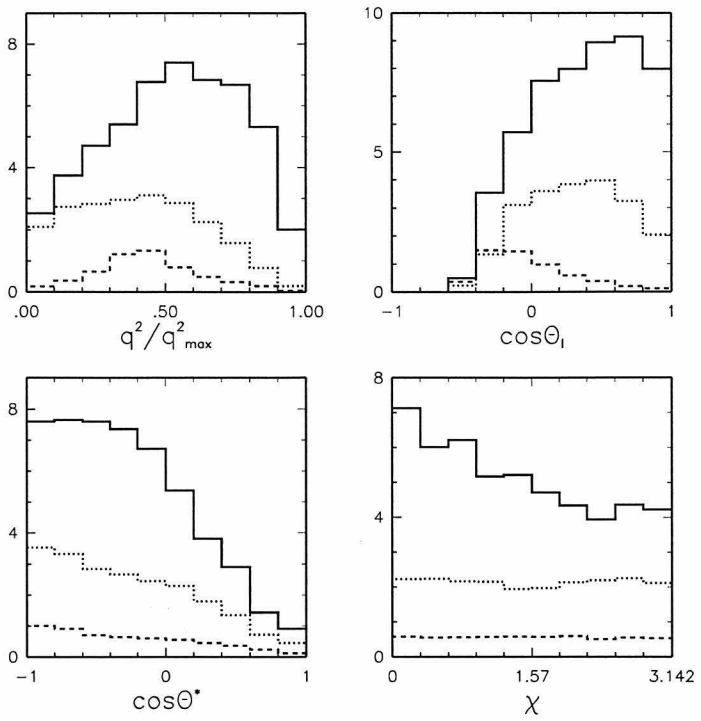


Figure 6.8: $D^{*+}(K\pi)$: Projections of each of the backgrounds. The solid line is the combinatoric background, the dotted line is the correlated background and the dashed line is the uncorrelated background.

to fix R_1 and R_2 to the values predicted by HQET and fit for their q^2 dependence. Fixing $R_1 = 1.3$, and $R_2 = 0.8$, we measure $\rho^2_{A_1} = 0.81 \pm 0.08$ for all modes combined, $\rho^2_{A_1} = 0.82 \pm 0.11$ for $\bar{B}^0 \to D^{*+}\ell^-\bar{\nu}$, $\rho^2_{A_1} = 0.79 \pm 0.12$ for $B^- \to D^{*0}\ell^-\bar{\nu}$ with $\rho^2_{A_1}$ $= 0.88 \pm 0.14$ and $\rho^2_{A_1} = 0.58 \pm 0.25$ for separate $D^{*0}(K\pi)$ and $D^{*0}(K\pi\pi^\circ)$ fits respectively. Only the statistical error is quoted for these fits. These fits also show how consistent the fit results are between the different modes. The fit results with one or more parameters fixed are not generally useful, but do show the precision one could attain, if the other parameters were known.

6.3 Goodness of Fit

As a measure of goodness of fit, a χ^2 can be constructed for the fit and its projections in several dimensions. We convert four dimensions into one dimension by binning each dimension into three bins. This gives 81 bins which we order into a one-dimensional

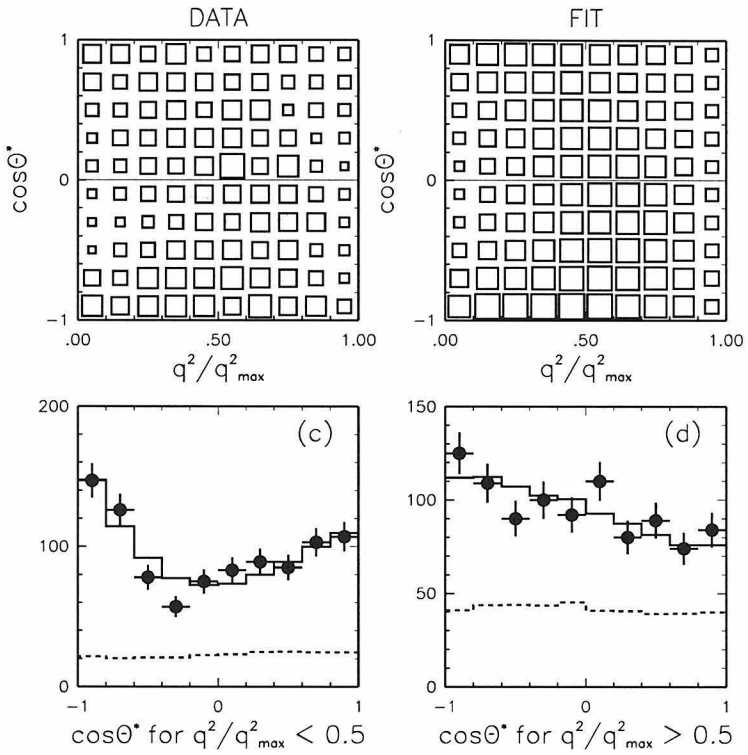


Figure 6.9: q^2 versus $\cos\theta^*$. For low values of q^2, a $\cos^2\theta^*$ distribution dominates. In c) and d), the points are the data, the solid line is the fit, and the dashed line is the background.

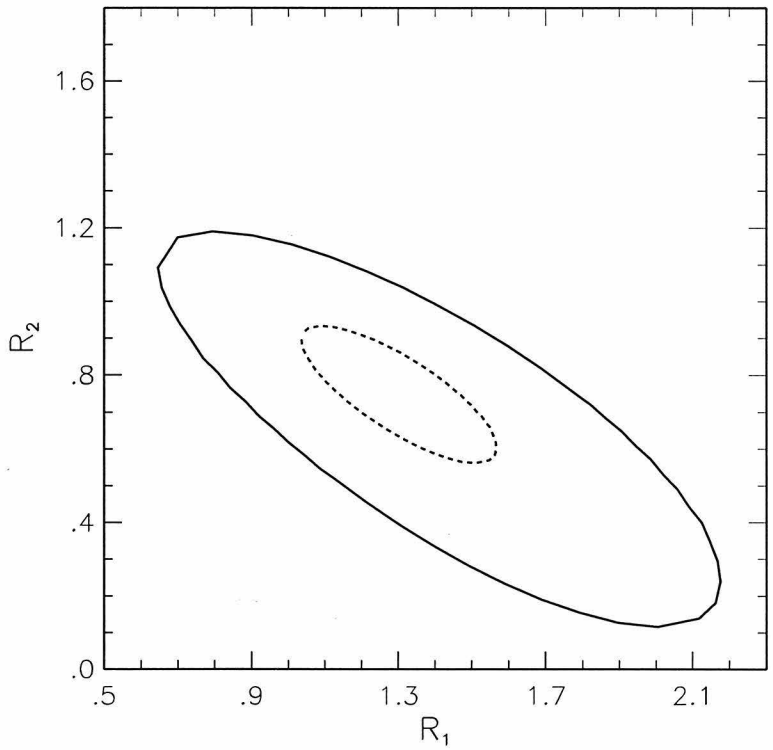


Figure 6.10: Contour of R_1 versus R_2. The solid line is the 95% C.L. region, and the dashed line is the 1σ contour. $\rho^2_{A_1}$ is also treated as a free parameter.

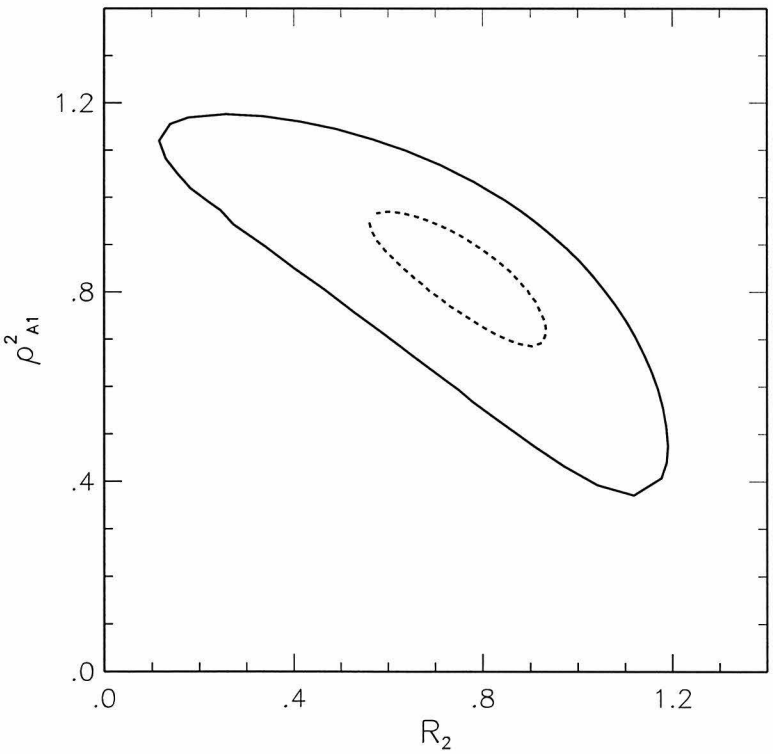


Figure 6.11: Contour of R_2 versus $\rho^2_{A_1}$. The solid line is the 95% C.L. region, and the dashed line is the 1σ contour. R_1 is also treated as a free parameter.

Fit Type	R_1	R_2	$\rho^2_{A_1}$	$\Delta \ln \mathcal{L}$
$1-\rho^2_{A_1}(w-1)$	1.29 ± 0.27	0.76 ± 0.19	0.84 ± 0.14	
$\exp[-\rho^2_{A_1}(w-1)]$	1.29 ± 0.27	0.77 ± 0.18	1.09 ± 0.25	0.054
$\frac{2}{w+1}\exp[(1-2\rho^2_{A_1})\frac{w-1}{w+1}]$	1.28 ± 0.27	0.79 ± 0.18	1.30 ± 0.32	0.262
$(\frac{2}{w+1})^{2\rho^2_{A_1}}$	1.28 ± 0.27	0.78 ± 0.18	1.22 ± 0.28	0.172
Neubert	1.34 ± 0.27	0.72 ± 0.17	0.82 ± 0.15	0.059
Close & Wambach	1.31 ± 0.27	0.75 ± 0.18	0.83 ± 0.14	0.010

Table 6.3: Combined fits using alternative parameterizations for the overall q^2 dependence, and including a q^2 dependence in the ratio of form factors. The Neubert and Close entries use the linear form for the overall q^2 dependence, and predict a small q^2 dependence for R_1 and R_2 as given in Equations 2.29 and 2.30.

Model	$\Delta \ln \mathcal{L}$	C.L. (%)
ISGW	7.74	0.1
ISGW2	3.31	8.5
BSW	4.16	4.0
KS	2.51	17.0

Table 6.4: Comparison of models with data using the change in likelihood relative to the HQET fit.

histogram. We calculate the χ^2 between the data and the fit, using the number of data events in the bin as the σ^2 in the denominator of the χ^2. We use the Cern routine PROB [60] to calculate the confidence level. We also calculate the χ^2 for the one-dimensional projections shown in Figures 6.1, 6.2, 6.3, and 6.4 which have 10 bins, and the two-dimensional projections using 25 bins. The χ^2 confidence levels are shown in Table 6.5

The goodness of fit in two-dimensional projections can be seen by plotting the difference between the data and the fit for the two-dimensional projections shown in Figures 6.5 and 6.6. Figure 6.12 shows $(N_{data} - N_{fit})$ for the two-dimensional projections of the combined fit. We do not find any obvious region where there is an excess of the data or the fit. We have also looked at the one-dimensional projections for slices of the other dimensions. This gives the ease of comparing data and MC in a one-dimensional distribution, while still allowing a look at the higher dimensionality

Projection	$B^- \to D^{*0}\ell^-\bar{\nu}$	$\bar{B}^0 \to D^{*+}\ell^-\bar{\nu}$	Combined
4 dimensions	77	75	89
q^2	12	28	6
$\cos\theta_\ell$	83	27	27
$\cos\theta^*$	45	24	17
χ	33	56	24
q^2 vs $\cos\theta_\ell$	96	78	61
q^2 vs $\cos\theta^*$	5	72	16
q^2 vs χ	82	71	99
$\cos\theta_\ell$ vs $\cos\theta^*$	68	9	11
$\cos\theta_\ell$ vs χ	30	52	55
$\cos\theta^*$ vs χ	6	23	39

Table 6.5: χ^2 confidence levels (%) of the fit projections for 3 parameter fits.

of the problem. All of these plots show good agreement between data and the fit.

The Kolmogorov statistic [61] tests whether there is a region where one distribution is consistently higher or lower than another, although the difference between individual bins may be small. It is designed to compare unbinned data in one dimension; however, in this case we use the one-dimensional projections placed in histograms of 100 bins. The Cern library routine HDIFF provides the Kolmogorov statistic between two histograms [62]. This test gives a high probability that the fit and data projections match each other. The lowest probability using this test is 1.4% for the χ projection for electrons in the $B^- \to D^{*0}\ell^-\bar{\nu}$ fit.

Another test is comparing the likelihood distribution of data events, with the likelihood distribution of the Monte Carlo events used to calculate the likelihood. We split each set of Monte Carlo signal and background events into two samples, and use one of them to fit the data. For each data event we plot the negative log of the likelihood. We then take the second set of Monte Carlo events and calculate the log likelihood for each MC event using the parameter values obtained from the fit of the data. Each signal MC event is weighted according to the fit parameters, and the background MC events are weighted according to their normalization. Figure 6.13 compares the shape of the log likelihood for data events, with that of MC events.

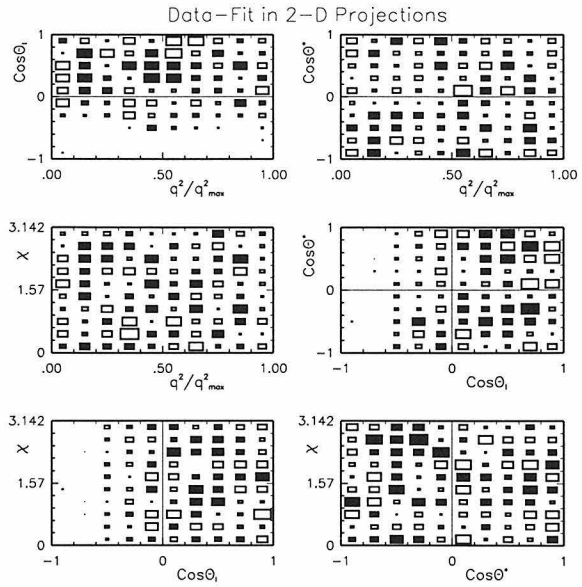


Figure 6.12: Combined fit: Two-dimensional projections of the difference between the data and the fit. White squares are where the data is in excess of the fit.

The mean of the data distribution is 4.170 ± 0.013 which agrees well with the mean of 4.168 from the MC distribution. The RMS width of the distributions are 0.5832 for both the data and MC. The χ^2 confidence level of the two histograms is 67%.

The comparison between the mean and the shape of the $-\ln \mathcal{L}$ distributions provides two ways of showing the goodness of fit. Comparing the mean of the data and MC distributions is comparable to running many MC experiments with the same number of events as the data and seeing where the likelihood of the data falls in the distribution of likelihoods from the MC experiments. The error on the mean is given by the RMS of the $-\ln \mathcal{L}$ per event distribution, divided by the square root of the number of data events. For many MC experiments, the distribution of likelihoods will be gaussian and we can estimate the gaussian sigma using the error on the mean. Comparing the shapes gives information on whether the function described by the MC matches the data. Since the negative log likelihood is minimized, points with low values tend to be signal events and points with large values tend to be background. For the signal MC, the mean of the $-\ln \mathcal{L}$ per event distribution is 4.094 versus a mean of 4.311 for the background MC, with approximate errors on the means of 0.004 and 0.005 respectively. This difference shows that the fitter can distinguish between

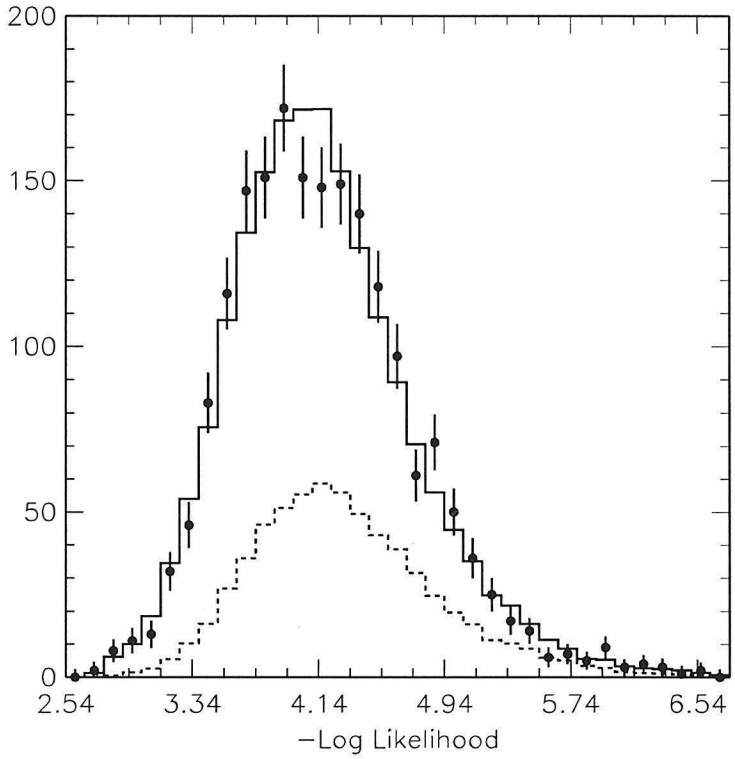


Figure 6.13: $-\ln \mathcal{L}$ for each event. The points are the data and the solid histogram is the sum of signal and background MC events using the same likelihood function as the data. The dashed line is the likelihood distribution of the background MC events.

signal and background event distributions. In general one can roughly say whether it is the signal or background that is being poorly modeled, depending on where the disagreement with the data is. We find good agreement between the data and our fitting function.

Chapter 7 Systematic Errors

The systematic errors for the fit results are categorized as being due to uncertainties in the detector efficiency for signal events; possible systematic biases with the fitting method; and the amount and shape of the backgrounds in the fit. Most systematic errors are simply evaluated by varying the quantity in question and measuring the change in the fit result.

7.1 Efficiency

For this measurement the efficiency shape across the four-dimensional kinematic space is needed, but not the absolute efficiency. The efficiency distribution predicted by the Monte Carlo can be changed, by reweighting the Monte Carlo events used in the fit. By varying the weight by the uncertainty in the efficiency, we obtain an estimate of the systematic error. Since the efficiency shape of a kinematic variable used in the fit is not easily understood or measured, we use the underlying kinematic variables such as the slow pion or lepton momenta that contribute to the kinematic quantities used in the fit.

The efficiency shape for charged slow pions has been measured with data [39]. The shape is parametrized by an exponential function that turns on at about 50 MeV/c. Figure 7.1 shows the efficiency shape for slow charged pions. We reweight the signal MC in the fit by the difference between the efficiency shape for data and MC as a function of the pion momentum. This change has the biggest effect on the q^2 distribution and thus the $\rho^2_{A_1}$ parameter in the fit, as shown in Table 7.4.

The efficiency shape for neutral slow pions has not been measured with the data. However, the integrated efficiency, over the momentum range of 60–225 MeV/c, shows agreement between Monte Carlo and data at the measured precision of 8% [63]. As seen in Figure 7.1, the π° efficiency does not have strong dependence on momentum.

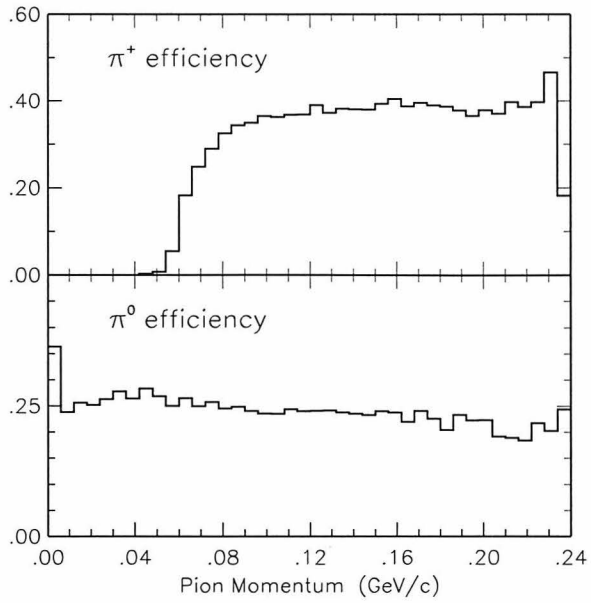


Figure 7.1: Slow pion efficiency from Monte Carlo for charged and neutral pions. Large bin fluctuations are due to statistics.

To obtain an estimate of the systematic error due to this uncertainty, we reweight the Monte Carlo events as a function of the pion momentum. We simply multiply the weights by a linear function which has a difference of 10% between the lowest and highest momentum pions.

This same technique is applied to reweight the signal Monte Carlo as a function of the lepton energy. The efficiency predicted by the signal Monte Carlo is varied by a linear function with a 3% difference at the extremes. The effect of this variation on the fit parameters is given in Table 7.4.

As discussed in section 5.3, the TRKSIM MC backgrounds are just generated for electrons, and reweighted as a function of momentum when used for muons. We vary this background reweighting for the fit using a linear reweighting that gives a variation of 10% between the lowest and highest momentum leptons. The sensitivity to this variation is small and the results of the variations on the fit parameters are shown in Table 7.4. Figure 7.2 plots the efficiency and efficiency ratio for electrons and muons.

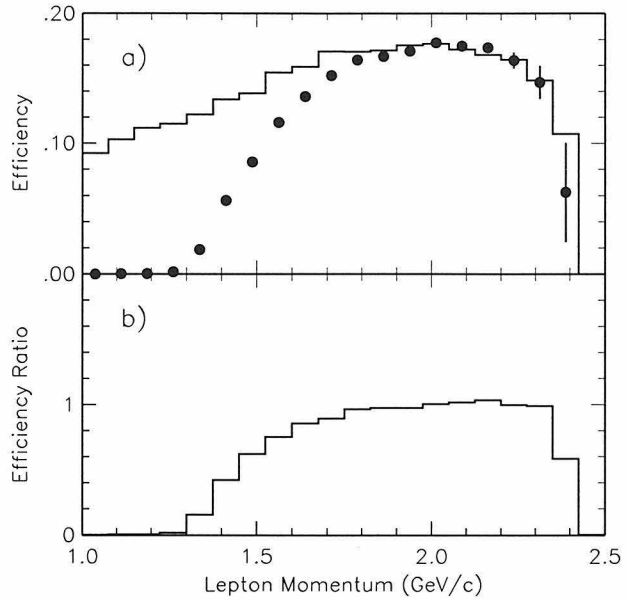


Figure 7.2: a) Lepton efficiency shape as a function of lepton momentum, as determined from Monte Carlo. The solid line is electrons and the points are muons. The vertical scale is arbitrary. b) The efficiency ratio between electrons and muons.

7.2 Systematics of Fitter

The fitting method has systematic errors associated with the size of the volume around each data point in the four-dimensional space and the sample size of MC events used for the fit.

7.2.1 Fit Volume Size

As a test of the fitting method, a high statistics sample of TRKSIM signal Monte Carlo was fit using another TRKSIM MC sample. The parameters used to generate the MC were $R_1 = 1.72$, $R_2 = 0.52$ and $\rho^2_{A_1} = 1.29$. Additional samples of MC were generated with only one of the parameter values changed. The resulting fits showed a bias in the measured parameter values. This is illustrated in Figures 7.3, 7.4, and 7.5. The size of the shift depends on the central value in the fit. We also note that there are large correlations between the fit parameters.

This systematic shift is due to the large bin size used. If the function across the bin is non-linear, then the average value of the function will not be at the center of

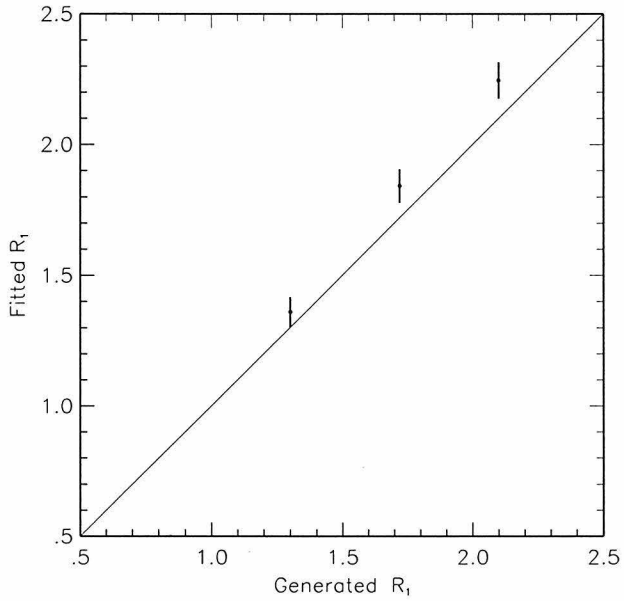


Figure 7.3: Fitted R_1 versus generated R_1 for high statistics signal Monte Carlo samples.

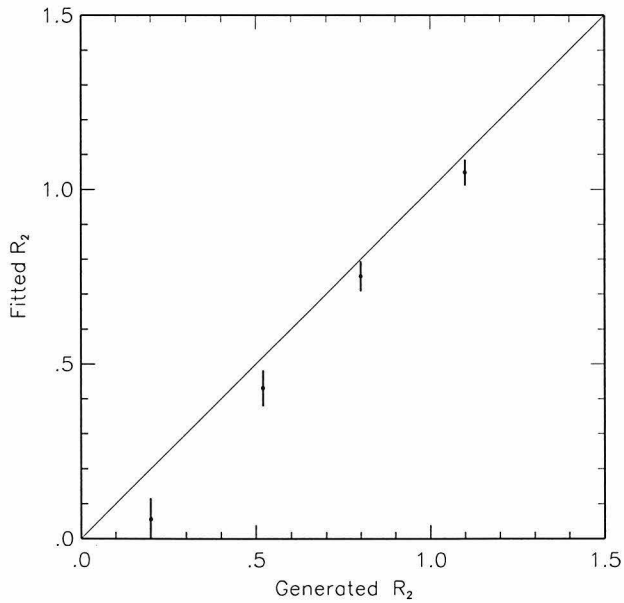


Figure 7.4: Fitted R_2 versus generated R_2 for high statistics signal Monte Carlo samples.

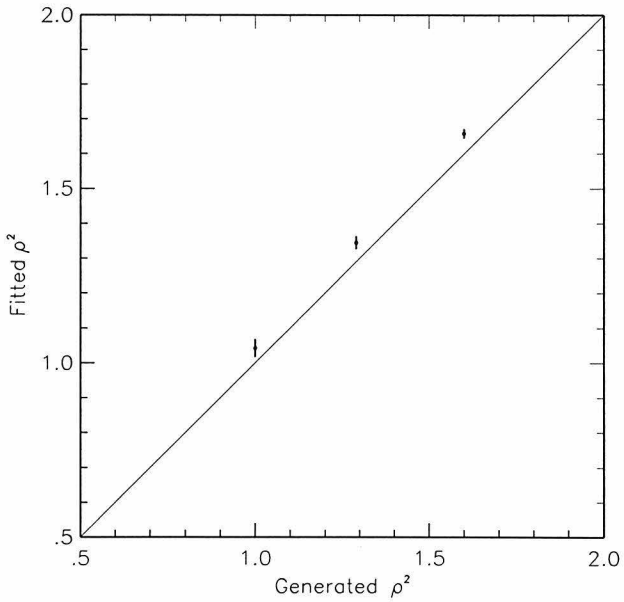


Figure 7.5: Fitted $\rho^2_{A_1}$ versus generated $\rho^2_{A_1}$ for high statistics signal Monte Carlo samples.

the bin where the data point lies. We verify that this is due to the volume size by changing the bin size in one dimension to half of its original value, and observing the change in the parameter value. Figure 7.6 shows that the systematic offset is corrected by reducing the q^2 bin size, and that reducing the bin size in the other dimensions has almost no effect. This effect was observed for other values of the generated parameters as well.

The original bins used for this test had half bin sizes of $\Delta q^2 = 1.22$, $\Delta\cos\theta_\ell = 0.2$, $\Delta\cos\theta^* = 0.1$, and $\Delta\chi = 0.314$. After observing the systematic correction possible by reducing the q^2 bin size, we chose new half bin sizes of $\Delta q^2 = 0.6$, $\Delta\cos\theta_\ell = 0.2$, $\Delta\cos\theta^* = 0.12$, and $\Delta\chi = 0.47$. It should be noted that the numbers quoted are for half the length of a bin. The fit values obtained in the MC study with the new bin sizes are shown in Figure 7.6.

The systematic error due to the finite bin size is evaluated by taking 10 different CLEOG signal MC samples, with approximately 10 times the data statistics, and fitting them to an independent CLEOG MC sample. The CLEOG MC "data" is weighted according to the parameters measured in the fit. The average of the 10 fits agrees with the input parameters to within the statistical error on the mean. The

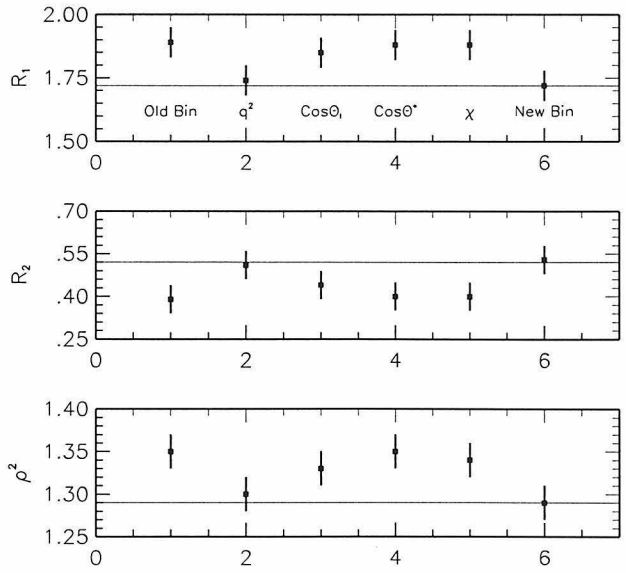


Figure 7.6: The change in the fit parameters for a MC fit, due to changing the volume size in the various dimensions. Old Bin refers to the original bin sizes chosen. The points labeled with the kinematic variable refers to fits where the bin was reduced to half its size in that dimension. New Bin gives the fit result using the new bin sizes chosen. The line indicates the generated parameter value.

systematic error quoted is the statistical error on the mean. Although we quote this systematic error as the bin size error in Table 7.4, this is really a check of any bias for the fit procedure.

To study the background volume size systematic, we vary the size of the background volume in the fit. We reduce the background volume by 0.5 for one dimension and redo the fit. This is repeated for each dimension, and the same procedure is done for increasing the background volume by a factor of 2. For the $D^{*0}(K\pi)$ mode we obtain shifts in the fit parameters as large as 0.5σ when reducing the volume size. However, this shift is not really a volume size effect, but a result of background MC statistics. Reducing the volume size by 0.5 greatly increases the number of data events without any background MC inside the volume surrounding that point. Since the combinatoric background fraction is on average about 1/3, removing that background can have a large effect on the fit results.

To account for this MC statistics effect, we redo the study but with a larger sample of background MC for the combinatoric background. We obtain this larger

sample by including the MC events in the δm sideband region, as opposed to just the signal region. These sideband events are not normally used in the fit since they do not correctly describe the shape of the background in the four kinematic variables. Figure 7.7 compares the shape of the background in the signal and sideband regions. We can improve the shape of the sideband events by constraining the $D\pi$ mass to the known D^* mass. This lowers the energy of the D^* candidate and improves the calculation of the angle $\cos\theta^*$ which has the largest discrepancy.

By using combinatoric MC events in the region $0.14 < \delta m < 0.152$, we increase the size of the combinatoric background MC by a factor of 2.5. Fitting with this larger sample of combinatoric background gives fit results of $R_1 = 1.48$, $R_2 = 0.91$ and $\rho^2_{A_1} = 0.81$. These parameter values agree almost exactly with the usual $D^{*0}(K\pi)$ fit results of $R_1 = 1.49$, $R_2 = 0.87$ and $\rho^2_{A_1} = 0.83$. Changing the background volume size in fits with this larger set of background MC, lessens the effect of MC statistics. Table 7.1 shows the change in fit results for the change in volume in each dimension. The change in fit results are not all in the same direction. As a result, for the systematic error we quote the single largest change for each parameter. For the $D^{*+}(K\pi)$ mode, the combinatoric background is not as large a fraction. Hence, changing the background volume size for the usual fit, does not give large changes in the fit results. Although the changes, given in Table 7.1, are partly a statistical effect, we quote the largest change for each parameter as the background volume systematic error.

7.2.2 Monte Carlo Statistics

The other systematic due to the fitting technique is the statistical error for the number of MC events used in the fit. To evaluate this error, the MC sample used for the fit is divided into four subsamples which are each used to fit the data. The rms of the four fit results determines the systematic error due to Monte Carlo statistics. Since our MC sample is four times larger, the rms value is divided by $\sqrt{4}$ to obtain the systematic error associated with our MC sample. The same procedure is independently applied to each of the background MC samples. For the $B^- \to D^{*0}\ell^-\bar{\nu}$ mode, the systematic

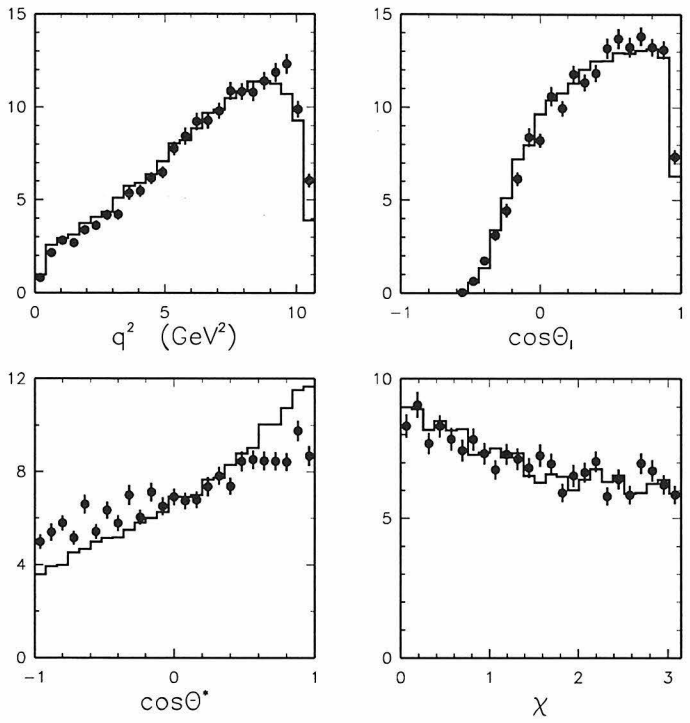


Figure 7.7: Comparison of kinematic distributions for fake D^{*0}'s from Monte Carlo. The points are events from the δm signal region. The solid line is events from the δm sideband region normalized to the same area. The $\cos\theta^*$ distributions show a difference in shape between the two regions.

Volume Change	$D^{*0}(K\pi)$			$D^{*+}(K\pi)$		
	δR_1	δR_2	$\delta\rho^2_{A_1}$	δR_1	δR_2	$\delta\rho^2_{A_1}$
0.5 q^2	–0.02	0.005	–0.009	–0.04	0.05	–0.02
0.5 $\cos\theta_\ell$	–0.01	0.01	0.003	0.008	–0.02	0.02
0.5 $\cos\theta^*$	0.05	–0.04	0.03	–0.02	0.01	–0.01
0.5 χ	–0.06	0.04	–0.04	0.01	–0.02	0.02
2.0 q^2	0.02	–0.02	0.01	0.03	–0.02	0.02
2.0 $\cos\theta_\ell$	–0.04	–0.005	0.01	0.006	–0.006	0.005
2.0 $\cos\theta^*$	0.02	–0.03	0.03	0.07	–0.04	0.02
2.0 χ	0.07	–0.03	0.03	0.02	–0.02	0.01

Table 7.1: The change in fit result after changing the background volume size in each dimension. This is for fits including the δm sideband for the background MC.

errors due to the $K\pi$ and $K\pi\pi^\circ$ modes are added in quadrature. Table 7.4 lists these contributions to the systematic error.

7.3 Fit Backgrounds

The background contributions to the systematic error are due to uncertainties in the amount of background and the shape of the background in the four-dimensional space. The uncertainty in the amount of a background is the error quoted for that background in Tables 4.5, 4.6 and 4.7. The shape of the background is due to the composition of the background from different physics sources, and the modeling of the detector response. The fake lepton and continuum backgrounds are negligible and do not contribute to the systematic error.

7.3.1 Correlated Background

The correlated, or D^{**}, backgrounds are from the D_1, D_2^*, $P_1^{(1/2)}$ and non-resonant modes. The EVT MC used to generate this background sample correctly handles the angular distribution of the D^* decay for each D^{**} state. The contribution of each mode, and its uncertainty, is given in Table 4.2. We independently vary the contribution of each D^{**} state in the fit, by the error given in Table 4.2. The change

in the fit result is given in Table 7.2. The D_1 rate is based on measurements of the branching ratio $\mathcal{B}(B \to D_1 \ell\nu)$. The Monte Carlo for the resonant modes is based on the ISGW2 model, which predicts a rate consistent with that measured for the D_1. The non-resonant contribution modeled with the Goity-Roberts prediction is less constrained by measurements in data. We double the shift given in Table 7.2 for the non-resonant mode when assigning the total systematic error. We add in quadrature the shifts for each mode to obtain the total systematic error given in Table 7.4. Varying each of the modes separately addresses changing the overall shape of the background and the normalization at the same time. Varying the correlated background normalization in the fit by its total uncertainty gives a shift significantly smaller than the systematic error we quote.

	D^{*0}			D^{*+}		
Mode	ΔR_1	ΔR_2	$\Delta\rho^2_{A_1}$	ΔR_1	ΔR_2	$\Delta\rho^2_{A_1}$
D_1	0.001	0.001	0.002	0.004	0.007	0.004
D_2	0.014	0.018	0.011	0.018	0.033	0.017
$P_1^{(1/2)}$	0.007	0.003	0.000	0.007	0.010	0.004
Non-res	0.019	0.001	0.015	0.010	0.004	0.009
Total	0.040	0.018	0.032	0.028	0.036	0.020

Table 7.2: The change in the fit for varying the amount of each D^{**} mode in the combined fit. The total error is the quadrature sum of the individual modes, after doubling the non-resonant error.

7.3.2 Combinatoric Background

The normalization of the combinatoric background is obtained from the data, as discussed in section 4.2.1. We vary the normalization of the combinatoric background in the fit by the uncertainty on the size of this background. For the $B^- \to D^{*0}\ell^-\bar{\nu}$ fit we separately vary the CLEOG and TRKSIM combinatoric backgrounds for both the $K\pi$ and $K\pi\pi^\circ$ modes. The change in fit result for each of these background samples is added in quadrature to obtain the systematic error listed in Table 7.4 as Combinatoric Norm.

We test how well the TRKSIM Monte Carlo events model the shape of the background by comparing the data sidebands with the Monte Carlo sideband events. In Figures 7.8, 7.9, and 7.10, we plot the projections in each of the four fit variables for events from the δm sideband region. The sideband events are not used in the fit, but we use them as a test of the MC, and find good agreement between the data and the MC.

We do a linear fit to the ratio of data to MC events in the one-dimensional projections. Table 7.3 gives the slopes measured in the fits. We find that for all variables the slope is consistent with zero with the largest deviation being 2.2σ for the $D^{*+}(K\pi)$ χ plot. We take the larger of either the measured slope or the measured uncertainty in the slope to do a linear reweighting of the TRKSIM Monte Carlo in the fit. The sample is reweighted in one dimension at a time, and the changes in the fit results are added in quadrature. For the $B^- \to D^{*0}\ell^-\bar{\nu}$ mode, we vary the $K\pi$ and $K\pi\pi^\circ$ background at the same time. The total error is given in Table 7.4 as the TRKSIM shape error.

	Offset	Fitted Slope		
		$D^{*0}(K\pi)$	$D^{*0}(K\pi\pi^\circ)$	$D^{*+}(K\pi)$
q^2	5.35	-0.017 $\pm$ 0.014	0.0054 $\pm$ 0.017	0.0058 $\pm$ 0.022
$\cos\theta_\ell$	0.0	0.0025 $\pm$ 0.079	0.076 $\pm$ 0.087	0.092 $\pm$ 0.12
$\cos\theta^*$	0.0	0.097 $\pm$ 0.070	0.095 $\pm$ 0.073	0.19 $\pm$ 0.12
χ	1.57	0.062 $\pm$ 0.045	0.101 $\pm$ 0.047	0.143 $\pm$ 0.064

Table 7.3: The measured slopes from comparing the data and MC sideband distributions.

7.3.3 Uncorrelated Background

The uncertainty in the uncorrelated background normalization is one of the larger systematic errors, especially for the R_1 parameter. This is a result of two effects. The first is the small number of flipped events in the data, resulting in a large fractional uncertainty on the amount of this background. This is especially true for the D^{*0}

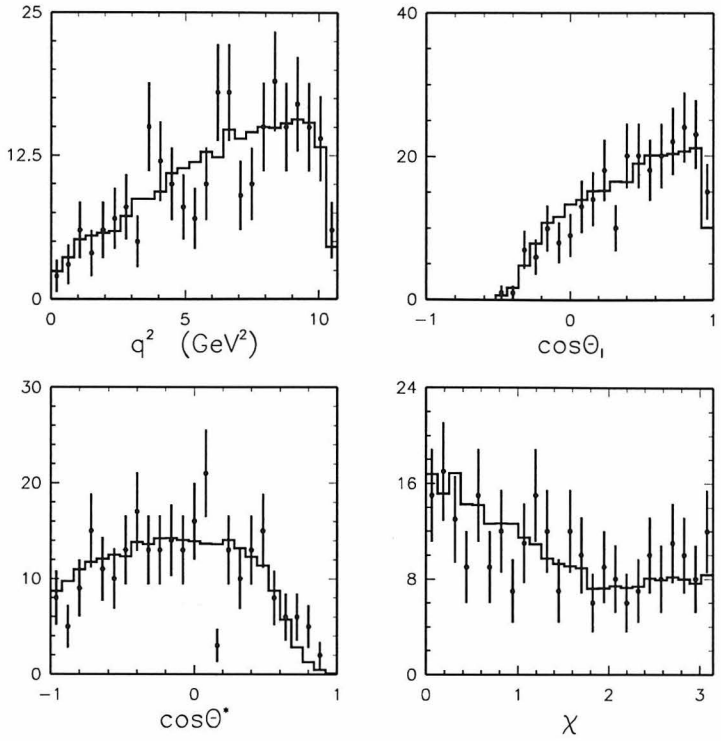


Figure 7.8: $D^{*+}(K\pi)$: Projections in the fit variables for events from the δm sideband. The points are the data and the solid line is the MC.

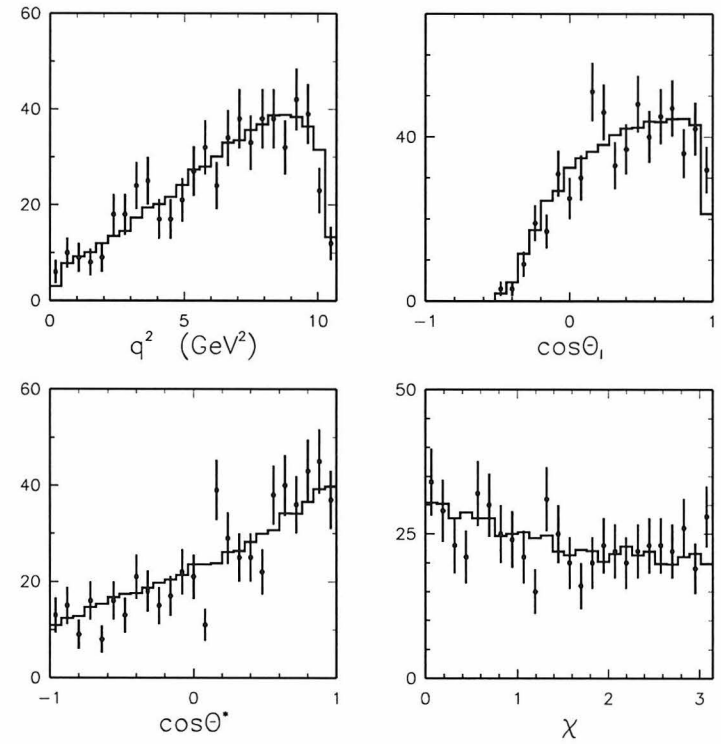


Figure 7.9: $D^{*0}(K\pi)$: Projections in the fit variables for events from the δm sideband. The points are the data and the solid line is the MC.

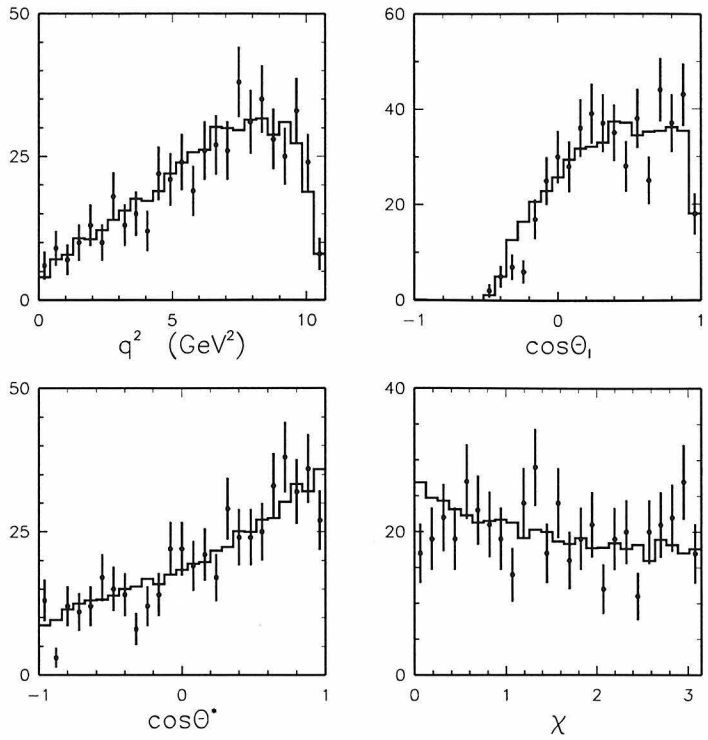


Figure 7.10: $D^{*0}(K\pi\pi^{\circ})$: Projections in the fit variables for events from the δm sideband. The points are the data and the solid line is the MC.

events where the large combinatoric background in the flipped sample results in an error that is larger than the background.

One might expect that, although the fractional error is large, the total amount of background is small and the systematic effect should also be small. However, the uncorrelated background is peaked towards negative values of $\cos\theta_\ell$. This region of phase space has a relatively small number of signal events, and is also the region with greater sensitivity to the R_1 parameter. Figure 7.11 illustrates the difference in shape between the signal and uncorrelated background distributions.

Varying the normalization on this background in the fit by the uncertainty on the normalization determines the systematic error, which is given in Table 7.4.

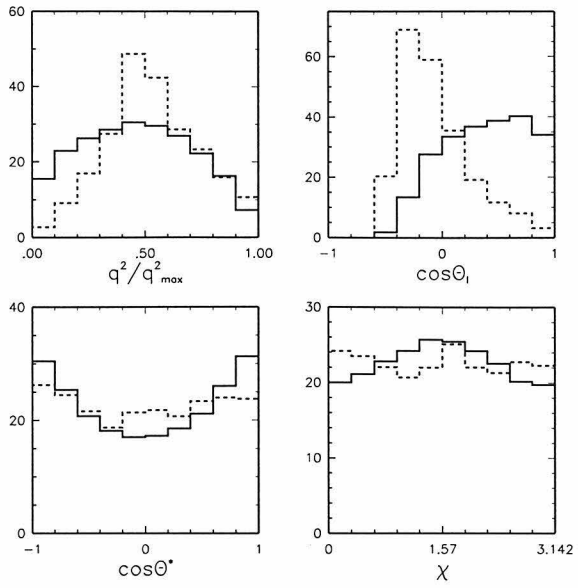


Figure 7.11: $D^{*0}(K\pi)$: The solid line is the signal MC in the fit. The dashed line is the uncorrelated background MC normalized to the same area in order to compare the shapes.

7.4 Decay Radiation

The Monte Carlo used to generate the decay $\bar{B} \to D^* \ell^- \bar{\nu}$ does not include events where one of the final state particles radiates a photon. A radiated photon leads to a change in the momentum spectrum of the particle. Since the electrons are the particles most likely to radiate, we can approximate the presence of decay radiation as a change in the lepton momentum spectrum.

Atwood and Marciano [8] parametrize the effect of decay radiation on the lepton energy spectrum as a correction given by

$$\left(\frac{E_{max} - E_\ell}{cE_\ell}\right)^{(2\alpha/\pi)[\ln(2E_\ell/m_\ell) - 1]}, \tag{7.1}$$

where c is a constant given by $c = (E_{max} - \bar{E}_\ell)/\bar{E}_\ell$ and $\bar{E}_\ell$ is the average lepton energy spectrum. We use $\bar{E}_\ell = 1.5$ GeV. The effect of this correction factor is a decrease of the electron energy spectrum by about 5% at the high end and a corresponding increase in the spectrum for low energy electrons. This correction gives a 1-2% correction for muons. We apply this correction factor to reweight the signal Monte Carlo in

our fits. To evaluate this systematic error, we refit the data without reweighting the signal Monte Carlo by this radiative correction term. We take the change in the fit result to be the systematic error for decay radiation which is given in Table 7.4.

Besides changing the overall lepton energy spectrum, decay radiation changes the lepton four vector in specific events. If the photon energy is large enough, there is a loss of efficiency due to events failing the MM^2 cut. The other effect of changing the lepton four vector is changing the calculated angle, $\cos\Theta_{BY}$, between the B and $D^*\ell$ system. Since that angle is used for calculating the kinematic variables in the "average B rest frame," mismeasuring the angle can introduce a bias into the reconstructed variables.

We study the effect of decay radiation on specific decays by using the PHOTOS Monte Carlo [64]. This program uses the decay products from the decay generator and then applies decay radiation to the decay, changing the decay particles four momenta as necessary. We generated a large sample of TRKSIM MC for the signal decay using PHOTOS to provide decay radiation. The photons are generated with a $1/k$ energy spectrum and an average energy of 130 MeV. The lower energy cutoff for a radiated photon is 1% of the particle's energy and 17% of the events have radiation. The sample was fit using a Monte Carlo sample without radiation, and the fitted parameters are consistent with the parameter values used to generate the Monte Carlo. Based on this study, we do not apply any additional decay radiation systematic error. All the systematic errors described above are summarized in Table 7.4.

7.5 Combined Fit Systematic Errors

To obtain the systematic error for the combined fit result, we simply combine the systematic errors from the individual fits. Most of the systematic errors are uncorrelated between the two modes. For these errors we add weighted errors in quadrature. The weights are calculated using the statistical error on the parameters from the individual fits.

The systematic errors due to lepton efficiency, TRKSIM muons, decay radiation

	$B^- \to D^{*0}\ell^-\bar{\nu}$			$\bar{B}^0 \to D^{*+}\ell^-\bar{\nu}$		
Systematic	σR_1	σR_2	$\sigma\rho^2_{A_1}$	σR_1	σR_2	$\sigma\rho^2_{A_1}$
Fit Technique						
Bin Size	0.036	0.026	0.019	0.033	0.024	0.018
Bkgnd Bin Size	0.07	0.04	0.04	0.07	0.05	0.02
Signal MC Stats.	0.066	0.032	0.026	0.052	0.046	0.023
Combinatoric Stats.	0.047	0.024	0.021	0.044	0.032	0.018
D^{**} Stats.	0.005	0.007	0.007	0.008	0.006	0.006
Uncorrelated Stats.	0.006	0.002	0.002	0.002	0.002	0.001
Backgrounds						
Combinatoric Norm.	0.059	0.030	0.026	0.014	0.020	0.001
D^{**} Norm.	0.040	0.018	0.032	0.028	0.036	0.020
Uncorrelated Norm.	0.115	0.041	0.011	0.066	0.037	0.015
TRKSIM Shape	0.04	0.02	0.04	0.018	0.010	0.019
Efficiency						
Pion Momentum	0.006	0.001	0.030	0.003	0.006	0.032
Lepton Energy	0.013	0.011	0.006	0.014	0.012	0.006
TRKSIM Muons	0.007	0.001	0.001	0.002	0.000	0.000
Decay Radiation	0.018	0.018	0.010	0.020	0.020	0.009
Total	0.186	0.087	0.087	0.130	0.100	0.061

Table 7.4: Contribution to the systematic error from various sources.

and the normalization of the D^{**} background are correlated between the two modes. For these errors we take the weighted average of the individual systematic errors. The total systematic error is the quadrature sum of each systematic error. The systematic errors assigned to the combined result are given in Table 7.5.

7.6 Comparison between Electrons and Muons

This section discusses a difference in the fit results for the $\rho^2_{A_1}$ parameter, when electrons are compared with muons. We describe the nature and significance of the difference, and the possible causes of the difference that were studied. No cause was uncovered and we discuss the assignment of a systematic error.

	Combined Fit		
Systematic	σR_1	σR_2	$\sigma \rho^2_{A_1}$
Fit Technique			
Bin Size	0.024	0.018	0.013
Bkgnd Bin Size	0.050	0.032	0.020
Signal MC Stats.	0.041	0.028	0.017
Combinatoric Stats.	0.032	0.020	0.014
D^{**} Stats.	0.005	0.005	0.005
Uncorrelated Stats.	0.003	0.001	0.001
Backgrounds			
Combinatoric Norm.	0.026	0.018	0.010
D^{**} Norm.	0.033	0.027	0.025
Uncorrelated Norm.	0.063	0.027	0.010
TRKSIM Shape	0.020	0.011	0.020
Efficiency			
Pion Momentum	0.003	0.003	0.023
Lepton Energy	0.014	0.011	0.006
TRKSIM Muons	0.004	0.001	0.001
Decay Radiation	0.019	0.019	0.009
Total	0.112	0.070	0.054

Table 7.5: Combined fit result systematic errors. These errors are based on those given in Table 7.4.

7.6.1 The Nature of the Difference

One can compare the results of two statistically independent fits by forming a χ^2 between the fit parameters, where the correlation between the parameters in the fit are included by using the variance matrix. For example, comparing the fits given in Table 6.1 gives a 33% confidence level that the parameters for the D^{*0} and D^{*+} modes are from the same parent distribution.

When we separate the data into electron and muon samples, we obtain fit results of $R_1 = 0.99 \pm 0.27$, $R_2 = 1.04 \pm 0.18$, and $\rho^2_{A_1} = 0.37 \pm 0.27$ for electrons and $R_1 = 1.94 \pm 0.58$, $R_2 = 0.25 \pm 0.41$, and $\rho^2_{A_1} = 1.23 \pm 0.15$ for muons. Comparing these two fit results gives a χ^2 confidence level of 4.2%. This low level of certainty could just be a result of a statistical fluctuation; however, it certainly merits further study. Table 7.6 gives the fit results for electrons and muons broken up by mode.

For the individual modes the fit errors are quite large, so that the fit results are still quite consistent. However, we observe that for all modes, the measured slope is significantly lower for electrons and is the parameter with the greatest statistical difference between electrons and muons. Fixing $R_1 = 1.3$ and $R_2 = 0.8$ we fit for the slope and obtain $\rho^2_{A_1} = 0.61 \pm 0.13$ for electrons and $\rho^2_{A_1} = 1.03 \pm 0.11$ for muons. This 2.47σ difference corresponds to a 1.4% confidence level.

	R_1	R_2	$\rho^2_{A_1}$
Combined	1.29 ± 0.27	0.76 ± 0.19	0.84 ± 0.14
Electrons	0.99 ± 0.27	1.04 ± 0.18	0.37 ± 0.27
Muons	1.94 ± 0.58	0.25 ± 0.41	1.23 ± 0.15
$D^{*+}(K\pi)$ elec	0.74 ± 0.34	0.93± 0.26	0.58± 0.32
$D^{*+}(K\pi)$ muon	2.38± 0.95	-0.15± 0.72	1.34± 0.18
$D^{*0}(K\pi)$ elec	1.46 ±0.66	1.05 ±0.37	0.35 ±0.51
$D^{*0}(K\pi)$ muon	1.36 ±0.80	0.79 ±0.53	1.13 ±0.30
$D^{*0}(K\pi\pi^\circ)$ elec	1.22 ±0.66	1.31 ±0.33	-0.34 ±0.87
$D^{*0}(K\pi\pi^\circ)$ muon	2.32 ±1.76	-0.005 ±1.18	1.09 ±0.39

Table 7.6: The fit results for separate muon and electrons samples.

Besides the difference in criteria used for lepton identification, there are two differences between the analysis of electrons and muons. Electrons have a lower momentum cut at 1.0 GeV/c, while the muon cut is at 1.4 GeV/c. Electrons also have a tighter missing mass squared cut of $MM^2 < 0.3$, compared to muons with a cut of $MM^2 < 0.7$. We remind the reader that the lower electron momentum cut is used to better measure negative values of $\cos\theta_\ell$, and that muons are not well identified below 1.4 GeV/c. The tighter electron MM^2 cut is used to reduce the extra correlated background that is introduced with the lower electron momentum cut.

We change the cuts for the electron sample to match those of the muons. This change removes 270 electron events and adds an additional 146 events. Fitting electrons with muon cuts gives fit results of $R_1 = 1.19 \pm 0.45$, $R_2 = 0.90 \pm 0.28$, and $\rho^2_{A_1} = 0.59 \pm 0.26$. This result agrees with the muon fit at the 19% C.L., and with the original electron fit at the 62% C.L., where we have taken into account the common statistics for the two electron samples. With muon cuts, the electron slope is

$\rho^2_{A_1} = 0.67 \pm 0.13$ with R_1 and R_2 fixed. This improves the agreement between electrons and muons to a 3.5% C.L. Comparing the electron slope results with the original and new cuts, and accounting for the overlap in statistics, gives a 48% agreement between the two electron fit results.

Since changing the electron cuts to match the muon cuts only results in a small improvement in the agreement between the two samples, it is not the cut differences that is the cause of the discrepancy. Nonetheless, we look at the variation of the fit results for separately varying the MM^2 and lepton momentum cuts. Because varying cuts changes the number of events in the sample, we expect some amount of variation due to statistical fluctuations. We estimate the statistical error on the fluctuation by $\sqrt{\frac{(N-n)}{n}}\sigma$, where σ is the error for the fit with N events, and n is the number of events with the new set of cuts. The fraction of background events can vary with the cut values. This is obviously the case for the correlated background, where a tighter MM^2 cut will reduce more of the background. When varying the cuts, we change the fraction of background events by using the change in the number of Monte Carlo events that model that background, and the change in data events. In Figure 7.12 we show the variation in fit results as a function of the MM^2 cut, for electrons and muons. The difference between the electron and muon slope result is evident. The variation in the slope with R_1 and R_2 fixed is shown in Figure 7.13. This figure shows more variation with the MM^2 cut, but no significant systematic effect. Varying the electron momentum cut from 1.0 to 1.4 GeV/c does not produce any systematic shift in the fitted slope.

7.6.2 Source of the Difference

Figures 7.14 and 7.15 show the projections in the four fit variables for electrons and muons separately, where the fit result is from the combined fit. The fit matches the data for both electrons and muons. Comparing the q^2 distributions, which is what determines the slope parameter, shows that electrons have data in excess of the fit for the lowest q^2 values, and a deficit at high q^2. The muon sample has the

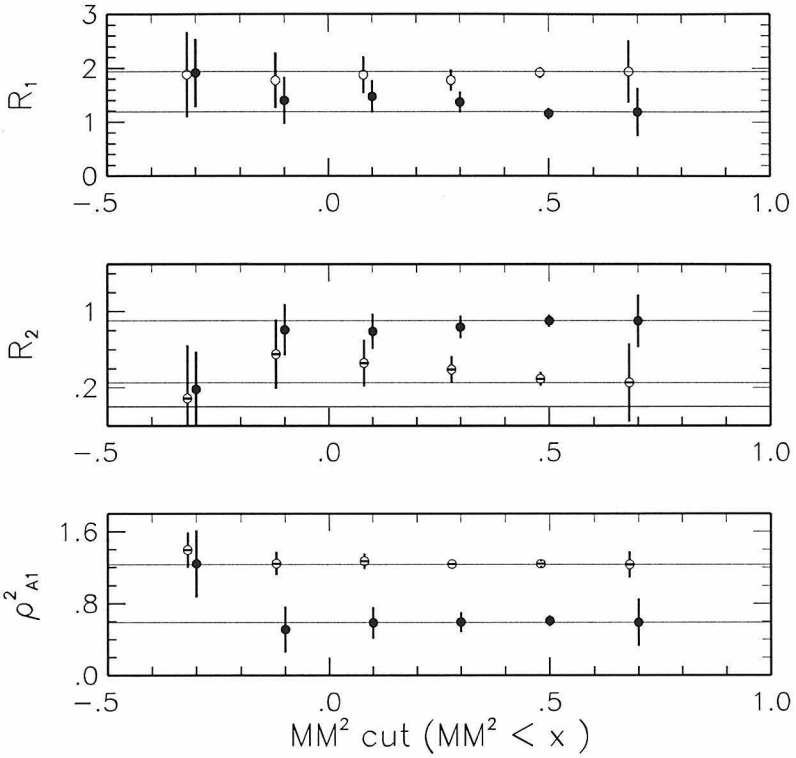


Figure 7.12: The variation in fit results as a function of MM^2 cut. The x-axis is the value of the MM^2 cut. The plot should be read from right to left, which is the direction of tightening the cut. The solid points are electrons and the open circles are muons. The far right point is the fit result and associated error for fitting electrons and muons separately. The errors on the other points are the expected change in error for the statistics that are lost from tightening the cut. Those points and errors should be compared to their respective line.

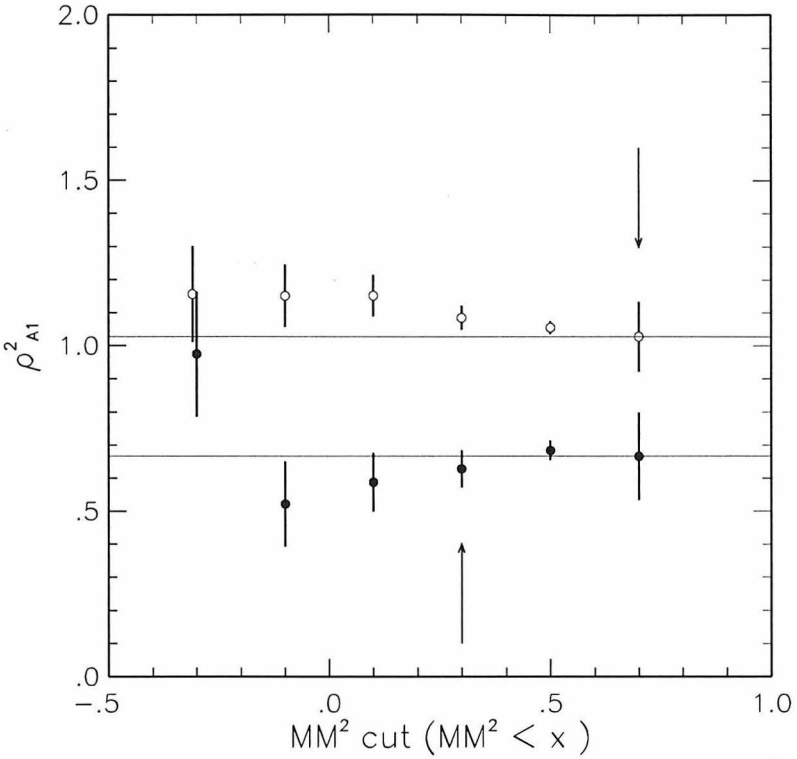


Figure 7.13: The variation in the slope result as a function of MM^2 cut. The x-axis is the value of the MM^2 cut. R_1 and R_2 are fixed in the fit. The solid points are electrons and the open circles are muons. The far right point is the fit result and associated error for fitting electrons and muons separately. The errors on the other points are the expected change in error for the statistics that are lost from tightening the cut. Those points and errors should be compared to their respective line. The arrows show the usual MM^2 cut value for muons (top) and electrons (bottom).

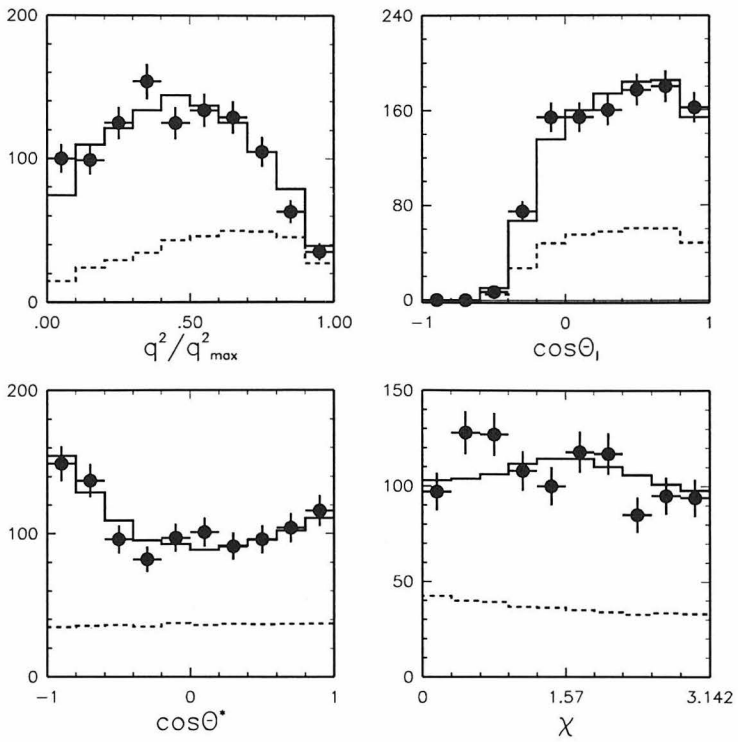


Figure 7.14: Projections in each of the 4 fit variables for electron events. The points are the data, the solid line is the fit and the dashed line is the contribution from backgrounds.

opposite trend, which explains how the muon slope is measured to be higher than the electron slope. However, these fluctuations in a few bins cannot distinguish between a statistical fluctuation or a systematic error.

The possible causes for the difference in the slope result can be due to differences in backgrounds or lepton efficiency. To study possible causes for the difference, we can start by looking at the size of the systematic errors given in Table 7.4. All of the systematic errors for the slope parameter, $\rho^2_{A_1}$, are significantly smaller than the size of the difference. Furthermore, the larger systematic errors, for example the slow pion efficiency or the shape of the TRKSIM MC, are independent of the lepton flavor.

For electrons having the same cuts as muons, the backgrounds are essentially the same. Any lepton specific backgrounds, such as from $(B \to D^* D_s)(D_s \to \mu\nu)$, are too small to have an effect on the fit. Nonetheless, we still looked at the effect of backgrounds on the fitted slope. We studied the effect of the backgrounds by varying the fraction of each of the backgrounds. Since the combinatoric background

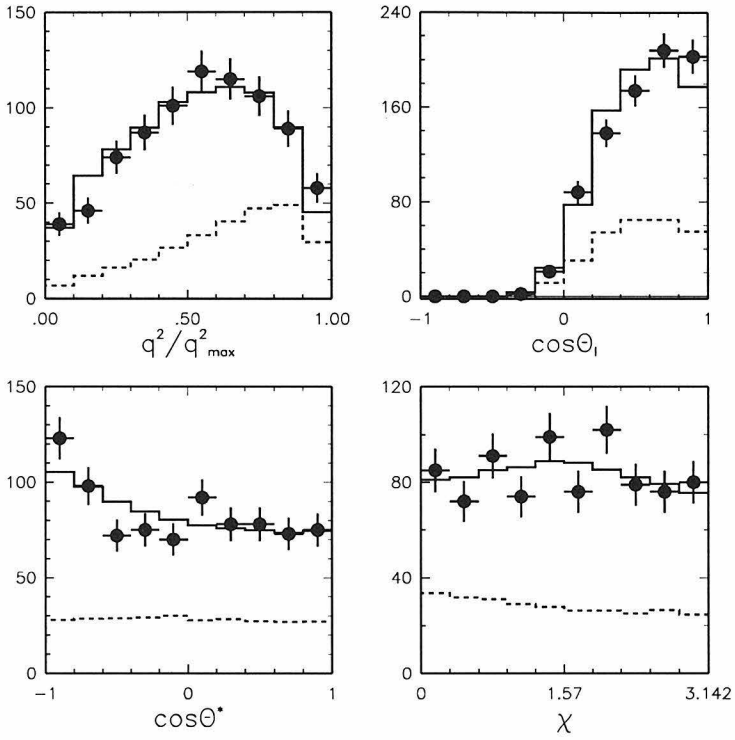


Figure 7.15: Projections in each of the 4 fit variables for muon events. The points are the data, the solid line is the fit and the dashed line is the contribution from backgrounds.

is relatively large, varying the background fraction by a large amount can change the fitted slope. However, the change is in the same direction for electrons and muons, which is expected. The amount of correlated background is different when the electrons and muons have different cuts. However, varying this background fraction by a factor of 3 has little change on the fitted slope result, and the change is in the same direction for both electrons and muons.

The obvious difference between electron and muon samples is the lepton identification efficiency. However, as shown in section 7.1, the lepton momentum efficiency does not have a strong effect on the fitted slope. As a further test, the lepton momentum was reweighted with a linear slope so that the change in efficiency at the endpoints was as large as 50%. Even for this extreme variation, the fitted slope changed by only ± 0.03.

Section 7.4 discusses the effect of decay radiation on the fit results. Since electrons are much more likely to radiate than muons, radiation would be a good candidate for producing a difference between electron and muon fit results. However, the effect of decay radiation on the fit parameters is quite small. Using a sample of TRKSIM electron Monte Carlo with PHOTOS radiation but fitted using an MC sample without PHOTOS, we find that the fitted slope is extremely consistent with the generated slope. If we only use the subset of events that had a radiated photon, we find that the fitted slope is 3.7σ below the generated value. This shows that radiation produces an effect in the same direction as the difference in the data. However, an unreasonable amount of decay radiation would be required.

The other type of radiation is that due to bremsstrahlung in the detector, which again is much more likely for electrons than muons. The signal MC is generated using CLEOG which produces bremsstrahlung based on the amount of material in the detector. Using the MC we find that for electrons in signal events, 7% have bremsstrahlung radiation in the detector. This radiation also has a $1/k$ energy distribution, with a mean of 177 MeV. After all cuts, only 2% of the events have bremsstrahlung radiation. Since the amount of material in the detector is modeled at the level of better than 10%, and bremsstrahlung is included in the simulation, then bremsstrahlung

radiation cannot account for the difference between electrons and muons.

We have fitted the slope for electron and muon samples obtained from a sample of generic $B\bar{B}$ CLEOG Monte Carlo, for the $D^{*+}(K\pi)$ mode. These samples gave fit results of $\rho^2_{A_1} = 0.94 \pm 0.07$ for electrons and $\rho^2_{A_1} = 0.95 \pm 0.07$ for muons, with R_1 and R_2 fixed. The consistency of these results shows that the difference is not simply due to a difference in the way electrons and muons are handled by the fitting program.

We also consider the possibility that the difference is entirely due to a poor fit for one mode. However, for all modes we find good agreement between data and MC in the projections of the kinematic variables and in the $-\ln\mathcal{L}$ per event distributions. Similarly, we consider the possibility of data from a specific set of running conditions as causing the problem. We split the data into 4 datasets ordered by increasing run number. We find the fit results for the 4 datasets to be consistent.

The measured difference between electron and muon slopes is larger than what would likely occur if the difference was entirely due to a statistical fluctuation. However, since the difference is not extremely unlikely, one cannot assign the bulk of the difference to a systematic error. Furthermore, we cannot find any systematic dependence that could cause such a difference. As a result, we do not assign any additional systematic error to the final combined fit result.

Chapter 8 Conclusions

8.1 Summary of Results

We have measured the ratio of form factors R_1 and R_2 and the slope of the overall q^2 dependence, $\rho^2_{A_1}$, for the decays $B^- \to D^{*0}\ell^-\bar{\nu}$ and $\bar{B}^0 \to D^{*+}\ell^-\bar{\nu}$. We use both electrons and muons and exclusively reconstruct the D^* mesons through the decays $D^{*+} \to D^0\pi^+$ and $D^{*0} \to D^0\pi^\circ$, with $D^0 \to K^-\pi^+$ used for both D^{*+} and D^{*0}, and $D^0 \to K^-\pi^+\pi^\circ$ additionally used for D^{*0}. We do an unbinned likelihood fit over the four-dimensional kinematic space describing the four particle final state to extract the form factor parameters. For $B^- \to D^{*0}\ell^-\bar{\nu}$ we obtain the results

$$\begin{aligned} R_1 &= 1.48 \pm 0.42 \pm 0.19, \\ R_2 &= 0.88 \pm 0.26 \pm 0.09, \\ \rho^2_{A_1} &= 0.72 \pm 0.22 \pm 0.09. \end{aligned} \tag{8.1}$$

In $\bar{B}^0 \to D^{*+}\ell^-\bar{\nu}$ we measure

$$\begin{aligned} R_1 &= 1.16 \pm 0.35 \pm 0.13, \\ R_2 &= 0.65 \pm 0.27 \pm 0.10, \\ \rho^2_{A_1} &= 0.94 \pm 0.18 \pm 0.06. \end{aligned} \tag{8.2}$$

For the combined fit using both $B^- \to D^{*0}\ell^-\bar{\nu}$ and $\bar{B}^0 \to D^{*+}\ell^-\bar{\nu}$ decays, we obtain the results

$$\begin{aligned} R_1 &= 1.29 \pm 0.27 \pm 0.11, \\ R_2 &= 0.76 \pm 0.19 \pm 0.07, \\ \rho^2_{A_1} &= 0.84 \pm 0.14 \pm 0.05. \end{aligned} \tag{8.3}$$

These results support the calculations of HQET including symmetry breaking corrections, which predict [26]

$$R_1 \approx 1.3, \tag{8.4}$$
$$R_2 \approx 0.8.$$

The form and slope of the form factors is not predicted, but QCD sum rules are used to place bounds of $0.4 < \rho^2_{A_1} < 1.3$ on the slope [32]. Our measurement falls well within these bounds. Our results support the use of HQET in calculating non-perturbative QCD effects, by showing that the size of the symmetry breaking corrections are not large and that the calculated corrections agree with experiment. This understanding of hadron dynamics is crucial for reliably measuring the CKM matrix V_{cb}.

8.2 Tests of Factorization

As discussed in chapter 1.7, the leptonic and hadronic currents in $\bar{B} \to D^* \ell^- \bar{\nu}$ can be factorized into separate parts of the matrix element. For semileptonic decays this is allowed since there are no gluons exchanged between the leptons and quarks. For hadronic decays, there can be gluons exchanged between the quarks from the upper W vertex, and those from the $B \to D^*$ transition. Nevertheless, factorization provides a method of calculating hadronic decays and to some approximation may be valid. Using factorization, the amplitude for the decay $\bar{B}^0 \to D^{*+}\rho^-$ may be written as [6]

$$A = \frac{G_F}{\sqrt{2}} V_{cb} V^*_{ud} \langle \rho^- | (\bar{u}d) | 0 \rangle \langle D^{*+} | (\bar{c}b) | \bar{B}^0 \rangle. \tag{8.5}$$

The $B \to D^*$ current would then be the same one given in Equation 2.3 for the semileptonic decay, and the hadronic current creating the ρ is $\langle \rho^-(\epsilon, p) | (\bar{u}d) | 0 \rangle = -i f_\rho \epsilon_\mu$, where f_ρ is the meson decay constant. For spectator decays where the W is produced with a large momentum (small q^2), the final state mesons should be well separated and one would expect factorization to hold. The question then remains

how well it holds, and for what q^2 values.

The factorization hypothesis for hadronic decays can be tested by comparisons with semileptonic decays. Typically the rate for a hadronic decay, such as $B \to D^*\rho$, is compared to the rate for the decay $\bar{B} \to D^*\ell^-\bar{\nu}$ at $q^2 = m_\rho^2$ [1]. This can be written as

$$\frac{\Gamma(\bar{B}^0 \to D^{*+}\rho^-)}{\frac{d\Gamma}{dq^2}(\bar{B} \to D^*\ell^-\bar{\nu})|_{q^2=m_\rho^2}} = 6\pi^2 c_1^2 f_\rho^2 |V_{ud}|^2, \tag{8.6}$$

where c_1^2 is a QCD correction factor which is near unity. Browder and Honscheid [6] apply this factorization test for several different final states and show that factorization holds, within the limited statistical precision, to at least $q^2 < m_{a_1}^2$.

An alternative test of factorization is possible when the B decays to two vector mesons. In this case the polarization of the mesons can be compared to the polarization in $\bar{B} \to D^*\ell^-\bar{\nu}$ for a fixed q^2. Specifically we compare the amount of longitudinal polarization, which is expressed as

$$\frac{\Gamma_L}{\Gamma}(B \to D^*\rho) = \frac{\Gamma_L}{\Gamma}(\bar{B} \to D^*\ell^-\bar{\nu})|_{q^2=m_\rho^2}. \tag{8.7}$$

This factorization test has the advantage that it does not require QCD correction factors or knowledge of the meson decay constant which is unknown for D_s^* [6]. Figure 8.1 shows the contribution of the longitudinal and transverse polarizations as a function of q^2.

We calculate $\frac{\Gamma_L}{\Gamma}$ using

$$\frac{\Gamma_L}{\Gamma} = \frac{|H_0|^2}{|H_+|^2 + |H_-|^2 + |H_0|^2} \tag{8.8}$$

with q^2 fixed at the appropriate value. CLEO has measured the longitudinal polarization in $\bar{B}^0 \to D^{*+}\rho^-$ to be $(93 \pm 5 \pm 5)\%$ [65]. Using our measured form factor results, we calculate the ratio $\frac{\Gamma_L}{\Gamma}(\bar{B} \to D^*\ell^-\bar{\nu})|_{q^2=m_\rho^2} = (90.6 \pm 1.5 \pm 0.5)\%$. The agreement between the two results supports the use of factorization for this decay. For a broad

[1] For decays to a spin 0 meson, such as $B \to D^*\pi$, one compares the rate with the semileptonic longitudinal width, Γ_0. However, for $q^2 = m_\pi^2$, $\Gamma_{Total} \approx \Gamma_0$.

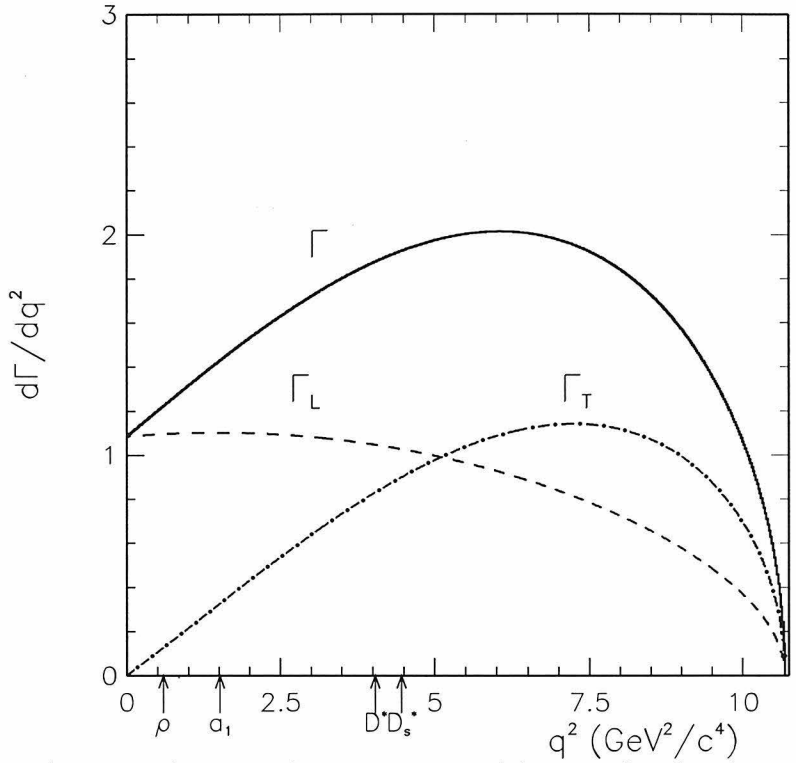


Figure 8.1: The contribution of transverse and longitudinal polarizations to the differential decay rate, as calculated using the measured form factor parameters. Also shown are the q^2 values where one would test factorization for the decays $B \to D^* V$. The vertical axis is an arbitrary scale.

resonance such as the ρ, the mass is not a constant, so we quote the polarization for the peak mass. The polarization does not change rapidly over the width of the ρ, and the difference in polarization between at the peak mass and -151 MeV of the peak mass is 3.6%. Table 8.1 gives the calculated longitudinal polarization for a number of vector final state particles.

q^2	Calculated Polarization (%)
m_ρ^2	$90.6 \pm 1.5 \pm 0.5$
$m_{a_1}^2$	$78.8 \pm 2.7 \pm 1.0$
$m_{D^*}^2$	$57.6 \pm 2.9 \pm 1.0$
$m_{D_s^*}^2$	$55.0 \pm 2.8 \pm 1.0$

Table 8.1: The amount of longitudinal polarization for $\bar{B} \to D^* \ell^- \bar{\nu}$ at $q^2 = m_V^2$. The calculated polarization is based on the form factor results given in this thesis.

8.3 Lorentz Structure of $\bar{B} \to D^* \ell^- \bar{\nu}$

The produced helicity states in $\bar{B} \to D^* \ell^- \bar{\nu}$ are a consequence of the $V - A$ structure of the decay. The weak current produces parity violation which is observable in decay asymmetries, since information on the produced c quark helicity is preserved in the D^* polarization states. These asymmetries are defined in section 2.1.5, and the measurement of the asymmetries is discussed here.

Previous analyses by Argus [66] and CLEO [67] have measured A_{FB} and the D^* polarization, using the distributions in $\cos\theta_\ell$ and $\cos\theta^*$. For the CLEO analyses, the A_{FB} measured depends on the lepton energy cutoff. In the B rest frame, $\cos\theta_\ell$ is given by

$$\cos\theta_\ell = \frac{4E_\ell m_B - m_B^2 - q^2 + m_{D^*}^2}{2m_B p_{D^*}}. \tag{8.9}$$

With a lepton energy cutoff, $\cos\theta_\ell$ cannot vary between -1 and +1 for the entire q^2 range, and the integrated asymmetry will be smaller. For leptons with energy greater than $(m_B - m_{D^*})/2$, $\cos\theta_\ell$ can only have positive values. In contrast, since we have measured the form factors, we simply calculate the asymmetries using Equations 2.15

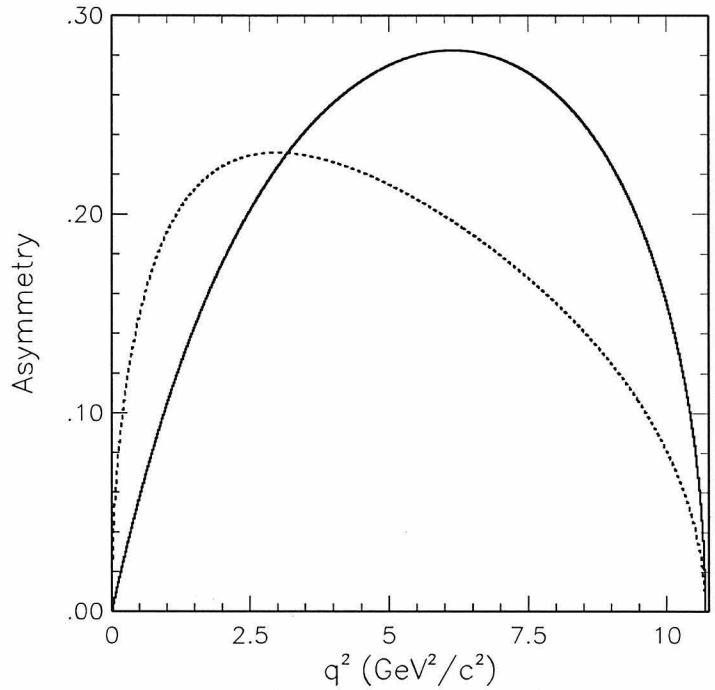


Figure 8.2: The asymmetries a_{FB} (solid line) and a_A (dashed line) as functions of q^2.

and 2.17, as is also done for the previous CLEOII form factor measurement [68]. This is essentially the same approach used by Argus in [66]. Table 8.2 gives the previous asymmetry measurements for A_{FB} and A_{pol}, our results and the predictions of HQET.

We also calculate the integrated asymmetry A_A, given by Equation 2.16, to be $0.18 \pm 0.03 \pm 0.01$. The asymmetries, before integration, depend on q^2. Figure 8.2 plots a_{FB} and a_A as a function of q^2. Figure 8.3 illustrates the effect of non-zero A_A in the data.

	A_{FB}	A_{pol}
This Result	$0.22 \pm 0.03 \pm 0.01$	$1.45 \pm 0.22 \pm 0.08$
Argus[66]	$0.20 \pm 0.08 \pm 0.06$	$1.1 \pm 0.4 \pm 0.2$
CLEO[67]	$0.14 \pm 0.06 \pm 0.03$	$0.65 \pm 0.66 \pm 0.25$
CLEOII[68]	$0.20 \pm 0.03 \pm 0.02$	$1.55 \pm 0.26 \pm 0.13$
HQET[26]	0.22	1.44

Table 8.2: Measurements and predictions of decay asymmetries. The CLEO results on A_{FB} and A_{pol} are for lepton momentum cuts of 1.0 GeV/c and 1.4 GeV/c respectively. The HQET prediction is for $\rho^2_{A_1} = 0.8$.

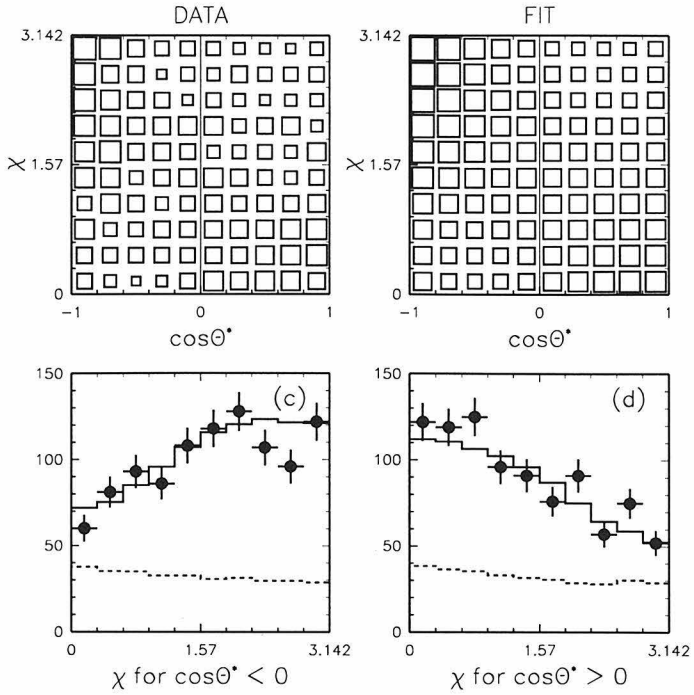


Figure 8.3: $\cos\theta^*$ versus χ. Top: The two-dimensional distribution for the data and the fit. Bottom: The projections in χ for $\cos\theta^* < (>)0$. The sign of the slope would change for a $V + A$ coupling.

The exact size of these asymmetries are determined by the hadronic physics governing the weak interaction. However, the sign of the asymmetry is a probe of the Lorentz structure of the $b \to c$ current. If the quark coupling was $V + A$, then $H_+ \leftrightarrow -H_-$ and $H_0 \to -H_0$ [25]. If the lepton coupling remained $V - A$, the sign of the asymmetries A_{FB} and A_A would be changed, and the slopes of the asymmetries in Figures 2.2 and 8.3 would change sign. If the lepton coupling was also $V + A$, the asymmetry would remain the same. Our measurement of A_{FB} excludes a $(V + A)(V - A)$ coupling at the 14σ level. If the $b \to c$ coupling was purely axial, then the asymmetries would be zero which is excluded at the 7σ level. The previous measurements of A_{FB} given in Table 8.2 also essentially excluded a $(V + A)(V - A)$ coupling. Furthermore, studies of the inclusive B decay lepton spectrum would have revealed a $V + A$ coupling. A measurement by the L3 experiment of the inclusive neutrino spectrum from b quark decay excludes a $(V + A)(V - A)$ coupling at the 6σ level [69].

8.4 Other Form Factor Results

The form factors have previously been measured at CLEO in the decay $\bar{B}^0 \to D^{*+}\ell^-\bar{\nu}$[68]. That measurement used both the $D^0 \to K^-\pi^+$ and $D^0 \to K^-\pi^+\pi^\circ$ modes and obtained form factor results of $R_1 = 1.18 \pm 0.30 \pm 0.12$, $R_2 = 0.71 \pm 0.22 \pm 0.07$ and $\rho^2_{A_1} = 0.91 \pm 0.15 \pm 0.06$. The measurement of the $D^{*+}(K\pi)$ mode in this thesis uses many of the same events as this previous analysis, and is consistent with that result [46]. Using the statistical errors and the correlations between the parameters, the $B^- \to D^{*0}\ell^-\bar{\nu}$ form factor results of this thesis are consistent with those $\bar{B}^0 \to D^{*+}\ell^-\bar{\nu}$ form factor results at the 39% confidence level.

The form factors were previously measured indirectly, using a combination of several results. This result [67] combined CLEO and Argus [66] measurements of A_{fb}, A_{pol}, $d\Gamma/dq^2$, and the $\bar{B} \to D^*\ell^-\bar{\nu}$ branching ratio in a single χ^2. The χ^2 was minimized for the A_1, A_2, and V form factors using two different parametrizations of the q^2 dependence with a fixed slope. They quote the ratios V/A_1 and A_2/A_1 at q^2_{max}. We convert their measurements to R_1 and R_2 which gives values of $R_1 = 0.85 \pm 0.46$ and $R_2 = 0.81 \pm 0.19$ when using an ISGW slope, and $R_1 = 1.05 \pm 0.50$ and $R_2 = 0.63 \pm 0.22$ for the second exponential form given in Equation 2.23 with $\rho = 1.19 \pm 0.25$.

Several experiments have measured $|V_{cb}|$ in $\bar{B} \to D^*\ell^-\bar{\nu}$ decay using the $d\Gamma/dq^2$ distribution. These measurements set R_1 and R_2 to the HQS prediction of 1, and perform a 2 parameter fit to extract $|V_{cb}|$ and $\hat{\rho}^2$, the overall form factor slope. Because R_1 and R_2 have been fixed to unity, the slope, $\hat{\rho}^2$, measured in these experiments, is not identical to the $\rho^2_{A_1}$ in this thesis. However, the two slope parameters can be related to each other by [70]

$$\Delta\rho^2 = \hat{\rho}^2 - \rho^2_{A_1} = -\frac{1}{6}(R_1^2 - 1) - \frac{1}{3}\frac{m_B}{m_B - m_{D^*}}(1 - R_2), \tag{8.10}$$

if R_1 and R_2 are known. Using our measured values of $R_1 = 1.29$ and $R_2 = 0.76$, we calculate $\Delta\rho^2$ = -0.24. We convert our measurement of $\rho^2_{A_1}$ to a value of $\hat{\rho}^2$ and

obtain $\hat{\rho}^2 = 0.60 \pm 0.14 \pm 0.06$. The errors quoted include the errors on R_1 and R_2 and their correlations with $\rho^2_{A_1}$.

Table 8.3 gives the slope parameters obtained from the measurements of $|V_{cb}|$. There is a large variation in the measured slope values. Gibbons [18] obtains an average value of 0.75 ± 0.11 for these results, where the error has been inflated to account for the poor agreement between the measurements. Our converted slope value agrees with this average. It should also be noted that the quoted CLEO result has a partial overlap in statistics with our measurement.

We point out that performing a weighted average of the slope results is not exactly the correct procedure for averaging the slope parameter. The difficulty lies in the dependence of the error on the measured value. This is discussed in section 5.4 and illustrated in Figure 5.10.

	$\hat{\rho}^2$
This Result	$0.60 \pm 0.14 \pm 0.06$
CLEOII	$0.84 \pm 0.12 \pm 0.08$
ARGUS	$1.17 \pm 0.24 \pm 0.06$
ALEPH	$0.29 \pm 0.18 \pm 0.12$
DELPHI	$0.78 \pm 0.16 \pm 0.11$
OPAL	$0.44 \pm 0.24 \pm 0.06$
Theory	$0.3 < \rho^2 < 1.1$

Table 8.3: The slope parameter, $\hat{\rho}^2$, as measured by several experiments. The numbers are taken from [18].

8.5 Measurement of $|V_{cb}|$

In order to measure the CKM matrix element $|V_{cb}|$, one needs to measure the width for $\bar{B} \to D^* \ell^- \bar{\nu}$ and know the contribution of the hadronic form factors. However, besides just knowing the ratios of form factors and form factor slope measured in this thesis, one also needs the normalization of the A_1 form factor at some fixed q^2. One can then separate the contributions of the form factors and $|V_{cb}|$ to the decay width.

This thesis is not a measurement of the decay rate, and the systematic errors associated with the absolute efficiency have not been studied. However, as a check the branching ratio has been measured and using the B lifetimes, we have calculated the decay width in section 4.3 to be $\Gamma(\bar{B} \to D^* \ell^- \bar{\nu}) = (30.7 \pm 3.0)$ ns^{-1}. We use this number to extract a measurement of $|V_{cb}|$ and illustrate an important prediction of HQET.

Since we cannot independently measure the normalization of the A_1 form factor, we rely on a HQET calculation [26]. At $q^2 = q^2_{max}$, which corresponds to $w = 1$ and the D^* produced at rest, only the A_1 form factor contributes, as the other form factors are multiplied by vanishing kinematic terms. This is a fortuitous coincidence since Luke's theorem gives the result that the $1/m_Q$ corrections to A_1 vanish at zero recoil [17], so the leading corrections arise at $1/m_Q^2$. In contrast, the $1/m_Q$ corrections to the other form factors remain.

In the full symmetry limit, the normalization of the Isgur-Wise function is 1, giving the result $h_{A_1}(1) = 1$. The leading corrections are proportional to $1/m_b^2$, $1/m_c^2$ and $1/m_b m_c$, and have been calculated. The normalization is also modified by perturbative QCD effects which have also been calculated. Including these corrections gives the result [26]

$$\frac{m_B + m_{D^*}}{2\sqrt{m_B m_{D^*}}} A_1(q^2_{max}) = h_{A_1}(1) = \eta_A + \delta_{1/m^2}, \tag{8.11}$$

where $\eta_A \approx 0.99 \pm 0.01$ is the perturbative QCD contribution and δ_{1/m^2} has been estimated as $\pm 3\%$. This gives the prediction $A_1(q^2_{max}) = 0.88 \pm 0.04$.

Using this prediction and the form factor ratios and slope measured in this thesis, we integrate Equation 2.10 over the q^2 range to obtain $\Gamma(\bar{B} \to D^* \ell^- \bar{\nu})|V_{cb}|^{-2} = 17.8$ ps^{-1}. Using the measured width obtained from the branching ratio measurement, we extract $|V_{cb}| = 0.0416 \pm 0.0025$. This error does not include the theoretical uncertainty on $A_1(q^2_{max})$ or the uncertainty on the measured form factor parameters. The result is consistent with the world average value of $|V_{cb}| = 0.0391 \pm 0.0027 \pm 0.0013$ [18]. Figure 8.4 shows the linear form of $h_{A_1}(w)$ using the measured slope, as compared to

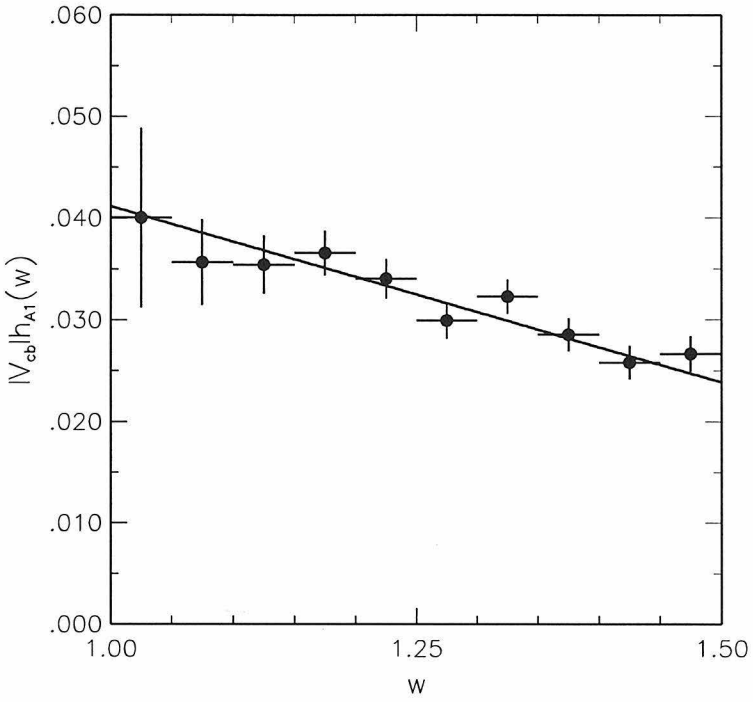


Figure 8.4: The line is $h_{A_1}(w)$ using the measured slope and the linear form. The points are the square root of the data after dividing out all factors except $|V_{cb}|^2|h_{A_1}|^2$. The data actually shown are the measured values of w which include smearing effects.

the data distribution for the measured variable w which includes smearing effects.

Appendix A $\bar{B} \rightarrow D^* \ell^- \bar{\nu}$ Decay Details

The decay $\bar{B} \rightarrow D^* \ell^- \bar{\nu}$ with $D^* \rightarrow D\pi$ has a decay rate given by

$$d\Gamma = \frac{|A|^2 d\Phi_4}{2m_B}, \tag{A.1}$$

where $|A|^2$ is the matrix element squared and Φ_4 is four body phase space for the final state $D^0 \pi \ell^- \bar{\nu}$. This appendix gives a somewhat detailed calculation of the decay rate, including 4 body phase space, and the amplitude calculation using the helicity formalism.

A.1 Phase Space

Since the $D^0 \pi \ell^- \bar{\nu}$ final state has 4 particles, each with a four-momentum, there are 16 variables in the decay. However, each of the 4 particles has a definite mass which reduces the independent variables to 12. Overall energy and momentum conservation reduce the independent variables to 8. There are 3 Euler angles which describe the overall orientation of the 4 body system. Since the B is spinless, it has no preferred direction in space, and one can integrate over the 3 angles leaving 5 independent variables to describe the final state. Since the $D^0 \pi$ system came from a D^*, which has a narrow mass width, that is a further constraint to reduce the total degrees of freedom to 4. These can be chosen to be the four kinematic variables described in section 2.1.3, and are used below.

Phase space for a n-body decay may be written generally as

$$\Phi_n = (2\pi)^4 \delta(P - \sum_i^n p_i) \prod_i^n \frac{d^4 p_i}{(2\pi)^4} 2\pi \delta(p_i^2 - m_i^2), \tag{A.2}$$

where the first δ function conserves overall energy and momentum, and the last δ function is for final state particles that are on mass shell. The last part may be

simplified by using the delta function and integrating over the particle's energy to give

$$\int \frac{d^4p_i}{(2\pi)^4} 2\pi\delta(p_i^2 - m_i^2) = \int \frac{d^3p_i dE_i}{(2\pi)^3}\delta(E_i^2 - \vec{p}^2 - m^2) \quad (A.3)$$

$$= \frac{d^3p_i}{(2\pi)^3 2E_i}. \quad (A.4)$$

From now on we consider 4 body phase space for the decay $\bar{B} \to D^*\ell^-\bar{\nu}$ ($D^* \to D\pi$). This 4 body phase space can be written as 3 sets of 2 body phase space,

$$d\Phi_4 = (2\pi)^4\delta(P - p_1 - p_2 - p_3 - p_4)\prod_i^4 \frac{d^3p_i}{2E_i(2\pi)^3} \quad (A.5)$$

$$= d\Phi_2(\bar{B} \to D^*W^-)d\Phi_2(D^* \to D\pi)\frac{dm_{D^*}^2}{2\pi}d\Phi_2(W^- \to \ell^-\bar{\nu})\frac{dq^2}{2\pi} \quad (A.6)$$

$$= (2\pi)^4\delta(P - q - p_{D^*})\frac{d^3p_{D^*}}{2E_{D^*}(2\pi)^3}\frac{d^3q}{2E_q(2\pi)^3} \quad (A.7)$$

$$\times(2\pi)^4\delta(k - p_1 - p_2)\frac{d^3p_1}{2E_1(2\pi)^3}\frac{d^3p_2}{2E_2(2\pi)^3}\frac{dm_{D^*}^2}{2\pi}$$

$$\times(2\pi)^4\delta(q - p_3 - p_4)\frac{d^3p_3}{2E_3(2\pi)^3}\frac{d^3p_4}{2E_4(2\pi)^3}\frac{dq^2}{2\pi},$$

where P, p_{D^*} and q are the 4 momentum of the B, D^* and the $\ell\nu$ system respectively, and p_1, p_2, p_3, and p_4 are for the D, π, lepton and neutrino. After integrating over the δ functions, 2-body phase space is $\frac{|\vec{p}|d\Omega}{16\pi^2 m}$, where $|\vec{p}|$ is the momentum in the parent's rest frame. Substituting this formula into Equation A.8 gives

$$d\Phi_4 = \frac{1}{(4\pi)^5 4\pi^2}\frac{|\vec{p}_{D^*}|}{m_B}\frac{|\vec{p}_D|}{m_{D^*}}\frac{(q^2 - m_\ell^2)}{2q^2}d\Omega_\ell d\Omega^* dq^2 dm_{D\pi}^2, \quad (A.8)$$

where $|\vec{p}_D|$ and Ω^* defines the momentum of the D in the D^* rest frame, and $|\vec{p}_\ell| = (q^2 - m_\ell^2)/2q$ and Ω_ℓ are the momentum and solid angles of the lepton in the $\ell\nu$ rest frame. The angles for the decay $\bar{B} \to D^*W^-$ have been integrated out. This result is a differential in 6 variables; however, the $D\pi$ mass is a constant, and the matrix element does not depend on one of the angles as will be shown later.

A.2 Decay Amplitude

The matrix element for the decay $\bar{B} \to D^* \ell^- \bar{\nu}$ ($D^* \to D\pi$) can be expressed as the product of matrix elements for the decays
$\bar{B} \to D^* W^-(D^* \to D\pi)(W^- \to \ell^- \bar{\nu})$. We write this as

$$\mathcal{M} = \sum_{W, D^* spins} \mathcal{M}(\bar{B} \to D^* W^-) P(W) \mathcal{M}(W^- \to \ell^- \bar{\nu}) P(D^*) \mathcal{M}(D^* \to D\pi), \quad \text{(A.9)}$$

where $P(W)$ and $P(D^*)$ are propagators, and the sum is over the internal spin states of the W and D^*.

The W propagator is given by

$$P(W) = \frac{i\left(-g^{\mu\nu} + \frac{q^\mu q^\nu}{m_W^2}\right)}{q^2 - m_W^2}. \quad \text{(A.10)}$$

Since $q^2 << m_W^2$, the propagator reduces to $\frac{ig^{\mu\nu}}{m_W^2}$, which when combined with the weak coupling strength $\frac{g}{2\sqrt{2}}$ at each W vertex, gives the Fermi constant $ig^{\mu\nu} G_F/\sqrt{2}$. At the $b \to c$ vertex, there is also the CKM matrix element V_{cb}.

The D^* propagator is a Breit-Wigner given by

$$P(D^*) = \frac{1}{m_{D^*}^2 - m_{K\pi}^2 - i m_{D^*}\Gamma}. \quad \text{(A.11)}$$

Since the D^* has such a narrow width we will treat the propagator as a delta function, as shown later.

The decay amplitudes can be expressed by several different formalisms. In all the methods, one sums over the internal spin states, squares the matrix element, and then averages over initial state spins and sums over final state spins. Here we present the result using the helicity formalism, which works well for describing the angular distributions used in the fit.

A.2.1 Helicity Formalism

The helicity formalism amplitude for the decay of $1 \to 2 + 3$ is given by [71]

$$A(\Omega; m\lambda_2\lambda_3) = \sqrt{\frac{2s_1+1}{4\pi}} D^{s_1 *}_{m_1,\lambda_2-\lambda_3}(\phi, \theta, -\phi) A_{\lambda_2\lambda_3}, \tag{A.12}$$

where s_1 and m_1 are the spin and third component of spin of the initial state particle, and λ_2 and λ_3 are the helicity states of the two final state particles. The helicities are subject to the constraint that $|\lambda_2 - \lambda_3| \leq s_1$. $A_{\lambda_2\lambda_3}$ is the amplitude for a given helicity configuration and its value is determined by the decay dynamics. The other part is the D function defined as

$$D^j_{m',m}(\phi, \theta, \gamma) = e^{-i\phi m'} d^j_{m',m}(\theta) e^{-i\gamma m}. \tag{A.13}$$

We use the Jacob-Wick convention which sets $\gamma = -\phi$.

For the sequential decay $\bar{B} \to D^* W^- (D^* \to D\pi)(W^- \to \ell^- \bar{\nu})$, we sum over the internal spin states of the D^* and W. The amplitude is

$$\begin{aligned} A(\Omega, \Omega^*, \Omega_\ell) \;=\; & \sqrt{\frac{2s_{D^*}+1}{4\pi}\frac{2s_W+1}{4\pi}} \sum_{\lambda_{D^*},\lambda_W} D^{s_B *}_{\lambda_B,\lambda_{D^*}-\lambda_W}(\Omega) A_{\lambda_{D^*}\lambda_W} \\ & D^{s_{D^*} *}_{\lambda_{D^*},\lambda_D-\lambda_\pi}(\Omega^*) B_{\lambda_D\lambda_\pi} D^{s_W *}_{\lambda_W,\lambda_\ell-\lambda_{\bar{\nu}}}(\Omega_\ell) C_{\lambda_\ell\lambda_{\bar{\nu}}}, \end{aligned} \tag{A.14}$$

where Ω, Ω^* and Ω_ℓ are the solid angles in the rest frames of the B, D^* and W respectively.

The angles for the decay of the D^* and the W are θ^* and ϕ^*, and θ_ℓ and ϕ_ℓ respectively. The angles θ^* and θ_ℓ have been defined in Figure 2.1. The azimuthal angles ϕ^* and ϕ_ℓ are illustrated in Figure A.1.

This amplitude is further simplified by explicitly writing the spins of the particles and using the requirement $|\lambda_{D^*} - \lambda_W| \leq s_B$. We have $s_B = 0$, $\lambda_B = 0$, $\lambda_{D^*} = \lambda_W$, $\lambda_D = \lambda_\pi = 0$, and $\lambda_\ell = -1/2$, and $\lambda_{\bar{\nu}} = +1/2$. The fact that the B is spinless has been implicity used in writing Equation A.14, since that equation does not contain the spin density matrix to describe the production of the B. $\lambda_\ell = -1/2$ only holds if

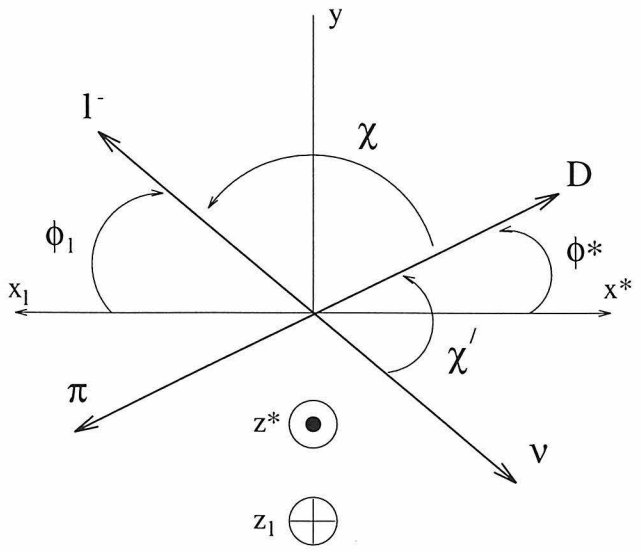


Figure A.1: Definition of azimuthal decay angles. The axes z^* and z_ℓ define the direction of the D^* and W respectively. We also define the angles $\chi' = \phi^* + \phi_\ell$ and $\chi = \pi - \chi'$.

the lepton is massless. Massive leptons are treated in a later section.

Explicitly writing the helicity states, expanding the D functions and using $\lambda_{D^*} = \lambda_W$ gives

$$\begin{aligned} A(\Omega, \Omega^*, \Omega_\ell) &= \sqrt{\frac{3}{4\pi}\frac{3}{4\pi}} \sum_{\lambda_{D^*}} A_{\lambda_{D^*}\lambda_{D^*}} e^{i\lambda_{D^*}\phi^*} d^1_{\lambda_{D^*},0}(\theta^*) B_{00} \\ & \quad e^{i\lambda_{D^*}\phi_\ell} d^1_{\lambda_{D^*},-1}(\theta_\ell) e^{i\phi_\ell} C_{-1/2\ 1/2}. \end{aligned} \tag{A.15}$$

The helicity of the D^* is either $\pm 1, 0$ and the resulting d functions are

$$d^1_{\pm 1,0}(\theta^*) = \mp \frac{\sin\theta^*}{\sqrt{2}}, \tag{A.16}$$

$$d^1_{0,0}(\theta^*) = \cos\theta^*, \tag{A.17}$$

$$d^1_{\pm 1,-1}(\theta_\ell) = \frac{1 \mp \cos\theta_\ell}{2}, \tag{A.18}$$

$$d^1_{0,-1}(\theta_\ell) = -\frac{\sin\theta_\ell}{\sqrt{2}}. \tag{A.19}$$

We define the angle $\chi' = \phi^* + \phi_\ell$ which removes the dependence of the amplitude on one angle. We rewrite $A_{\lambda_{D^*}\lambda_{D^*}}$ as H_+, H_-, and H_0, which are defined in Equation 2.6.

We square the amplitude to obtain

$$\begin{aligned}|A|^2(\theta^*,\theta_\ell,\chi') = |V_{cb}|^2\frac{G_F^2}{2}\frac{9}{32\pi^2}|B_{00}|^2|C_{-1/2\,1/2}|^2[&\frac{1}{2}(1-\cos\theta_\ell)^2(\frac{1}{2}\sin^2\theta^*)|H_+|^2 \\ &+\frac{1}{2}(1+\cos\theta_\ell)^2(\frac{1}{2}\sin^2\theta^*)|H_-|^2+\sin^2\theta_\ell\cos^2\theta^*|H_0|^2 \\ &-(\frac{1}{2}\sin^2\theta_\ell)(\frac{1}{2}\sin^2\theta^*\cos 2\chi')2H_+H_- \\ &+\frac{1}{\sqrt{2}}\sin\theta_\ell(1-\cos\theta_\ell)(\frac{1}{\sqrt{2}}\sin\theta^*\cos\theta^*\cos\chi')2H_+H_0 \\ &-\frac{1}{\sqrt{2}}\sin\theta_\ell(1+\cos\theta_\ell)(\frac{1}{\sqrt{2}}\sin\theta^*\cos\theta^*\cos\chi')2H_-H_0].\end{aligned} \tag{A.20}$$

The helicity amplitudes $H_\pm, H_0$ for the B decay have been discussed previously and are measured in this thesis. The helicity amplitude for the W decay, $C_{-1/2\ 1/2}$, can be directly calculated from the weak interaction coupling to the two leptons with

$$A = \sqrt{\frac{3}{4\pi}}D^{1*}_{\lambda_W -1}C_{-1/2\ 1/2} = \varepsilon^\mu u(p_\ell)\gamma_\mu(1-\gamma_5)v(p_{\bar{\nu}}). \tag{A.21}$$

The lepton current is squared to give the lepton tensor

$$L_{\mu\nu} = 8[p_\mu p'_\nu + p'_\mu p_\nu - 4(p\cdot p')g_{\mu\nu} + i\epsilon_{\mu\nu\alpha\beta}p^\alpha p'^\beta], \tag{A.22}$$

where p and p' are the four momenta of the charged lepton and neutrino. Multiplying by the W propagator, $-g^{\mu\nu}$, gives the result

$$\frac{3}{4\pi}|C_{-1/2\ 1/2}|^2 = 16(p\cdot p') = 16\frac{(q^2-m_\ell^2)}{2}, \tag{A.23}$$

where the coupling of the leptons to the W has already been included in the factor G_F.

Since there is only one helicity amplitude, B_{00}, for the D^* decay, we can relate it to the decay width for the decay $D^* \to D\pi$, using

$$\Gamma(D^* \to D\pi) = \frac{1}{2m_{D\pi}}\int|\mathcal{M}|^2\frac{P_D d\Omega}{16\pi^2 m_{D\pi}}. \tag{A.24}$$

The decay amplitude for a given helicity is

$$\mathcal{M}_{\lambda_{D^*}} = \sqrt{\frac{3}{4\pi}} D^1_{\lambda_{D^*},0}(\theta,\phi) B_{00}, \tag{A.25}$$

and the matrix element squared is

$$|\mathcal{M}|^2 = \frac{1}{3}\sum_{\lambda_{D^*}} |M_{\lambda_{D^*}}|^2 = \frac{|B_{00}|^2}{4\pi}, \tag{A.26}$$

where the factor of 1/3 is for the average over initial state spins. Integrating over phase space and rearranging terms gives the result

$$|B_{00}|^2 = 32\pi^2 m_{D\pi}\Gamma(D^* \to D\pi)\frac{m_{D\pi}}{P_D}, \tag{A.27}$$

which is needed in the total decay rate.

If the D^* were a broad resonance, we would leave the Breit-Wigner propagator in the differential decay rate, which would then also be a differential in the $D\pi$ invariant mass. Since the D^* is a very narrow resonance, we can simplify the final result by using [72]

$$\frac{m_{D\pi}\Gamma_{Total}}{(m^2_{D\pi} - m^2_{D^*})^2 + m_{D\pi}\Gamma_{Total}} \to \pi\delta(m^2_{D\pi} - m^2_{D^*}), \tag{A.28}$$

which is valid for $\Gamma << m$. Combining the term $|B_{00}|^2$ and the D^* propagator gives

$$\frac{|B_{00}|^2}{(m^2_{D\pi} - m^2_{D^*})^2 + m_{D\pi}\Gamma_{Total}} 32\pi^2 \mathcal{B}(D^* \to D\pi)\frac{m_{D\pi}}{P_D}\pi\delta(m^2_{D\pi} - m^2_{D^*}), \tag{A.29}$$

where we have used the relation $\mathcal{B}(D^* \to D\pi) = \Gamma(D^* \to D\pi)/\Gamma_{Total}$.

Combining phase space given in Equation A.8, the matrix element squared in Equation A.20, using the calculated values of $|B_{00}|^2$ and $|C_{-1/2\ 1/2}|^2$, and integrating over $dm^2_{D\pi}$ and ϕ_ℓ gives the full differential decay rate

$$\frac{d\Gamma}{dq^2 d\cos\theta_\ell d\cos\theta^* d\chi'} = \frac{3G_F^2|V_{cb}|^2}{8(4\pi)^4}\frac{P_{D^*}(q^2 - m_\ell^2)^2}{m_B^2 q^2}\mathcal{B}(D^* \to D\pi)[\tag{A.30}$$
$$(1 - \cos\theta_\ell)^2(\sin^2\theta^*)|H_+|^2 + (1 + \cos\theta_\ell)^2(\sin^2\theta^*)|H_-|^2$$

$$+4\sin^2\theta_\ell\cos^2\theta^*|H_0|^2 - 2(\sin^2\theta_\ell)(\sin^2\theta^*\cos 2\chi')H_+H_-$$
$$+4\sin\theta_\ell(1-\cos\theta_\ell)(\sin\theta^*\cos\theta^*\cos\chi')H_+H_0$$
$$-4\sin\theta_\ell(1+\cos\theta_\ell)(\sin\theta^*\cos\theta^*\cos\chi')H_-H_0].$$

This formula is the same as that given in Equation 2.9, except for the angle $\chi' = \pi - \chi$, which gives a difference in sign for the last two terms.

A.2.2 Decays with Massive Leptons

Because the charged lepton produced in the decay is not massless, it can also be produced with a right handed spin. This spin-flip of the lepton is helicity suppressed by the mass of the lepton and is generally ignored for electrons and muons where the contribution is quite small. However, the effect is important for decays to tau's where it should not be ignored.

Since the prescription for calculating decay rates is to sum over final state spins after squaring the matrix element, the contribution of the spin-flip terms can be separately calcuated and simply added to the result given in Equation A.30.

The calculation proceeds in the same way as given in the previous section. The decay amplitude is basically the same with several important changes. Since the lepton helicity is now $\lambda_\ell = +1/2$, the D functions change and the lepton-neutrino system can also couple to the spin zero part of the W. The spin-flip amplitude for $W^- \to \ell^-\bar{\nu}$ is given by

$$A(\Omega_\ell) = \sqrt{\frac{3}{4\pi}}D^{1*}_{\lambda_W,0}(\Omega_\ell)C_{1/2\ 1/2} + \sqrt{\frac{1}{4\pi}}D^{0*}_{0,0}(\Omega_\ell)C_{1/2\ 1/2}. \qquad \text{(A.31)}$$

The first part of this amplitude can simply be substituted into Equation A.15 and will give a different angular distribution for the lepton. The associated d functions are

$$d^1_{\pm1,0}(\theta_\ell) = \mp\frac{\sin\theta_\ell}{\sqrt{2}}, \qquad \text{(A.32)}$$
$$d^1_{0,0}(\theta_\ell) = \cos\theta_\ell. \qquad \text{(A.33)}$$

The second term couples to a new helicity amplitude H_t which was defined in Equation 2.6. Its d function is $d^0_{0,0} = 1$, which gives a flat distribution for $\cos\theta_\ell$. Because of the constraint that the helicities of the D^* and the W are the same, the angular distribution of the D^* decay associated with the H_t amplitude is that for the helicity zero state. As before, we square the amplitude after summing over the internal spin states.

The other difference with the spin-flip amplitude is the value of $C_{1/2\ 1/2}$. Again we can calculate its value directly from the weak interaction coupling for the spin flip case where

$$\mathcal{M} \propto \frac{\varepsilon \cdot q q^\mu}{q^2} \bar{u}(p_\ell)\gamma_\mu(1-\gamma_5)v(p_{\bar{\nu}}), \tag{A.34}$$

where $q = p_\ell + p_{\bar{\nu}}$, ε is the spin of the W, and we have dropped the weak coupling strength. Squaring the matrix element gives

$$\begin{aligned} |\mathcal{M}|^2 &\propto \frac{|\varepsilon \cdot q|^2}{q^4} m_\ell^2 Tr[(\not{p}_\ell + m_\ell)(1-\gamma_5)\ \not{p}_{\bar{\nu}}(1+\gamma_5)] \\ &\propto \frac{m_\ell^2}{q^2} 4(q^2 - m_\ell^2), \end{aligned} \tag{A.35}$$

where we have used $|\varepsilon \cdot q|^2 = q^2$.

The contribution of the spin-flip amplitude to the differential decay rate is

$$\begin{aligned} \frac{d\Gamma_{spin-flip}}{dq^2 d\cos\theta_\ell d\cos\theta^* d\chi'} = \frac{3G_F^2|V_{cb}|^2}{8(4\pi)^4} \frac{P_{D^*}(q^2 - m_\ell^2)^2}{m_B^2 q^2} \mathcal{B}(D^* \to D\pi) \frac{m_\ell^2}{q^2} [\\ \sin^2\theta_\ell \sin^2\theta^* |H_+|^2 + \sin^2\theta_\ell \sin^2\theta^* |H_-|^2 \\ +4\cos^2\theta_\ell \cos^2\theta^* |H_0|^2 + 4\cos^2\theta^* |H_t|^2 \\ +2\sin^2\theta_\ell \sin^2\theta^* \cos 2\chi' H_+ H_- \\ +4\sin\theta_\ell \cos\theta_\ell \sin\theta^* \cos\theta^* \cos\chi' H_+ H_0 \\ +4\sin\theta_\ell \cos\theta_\ell \sin\theta^* \cos\theta^* \cos\chi' H_- H_0 \\ +4\sin\theta_\ell \sin\theta^* \cos\theta^* \cos\chi' H_+ H_t \\ +4\sin\theta_\ell \sin\theta^* \cos\theta^* \cos\chi' H_- H_t \\ +8\cos^2\theta^* \cos\theta_\ell H_0 H_t]. \end{aligned} \tag{A.36}$$

A.2.3 Partial Wave Amplitudes

Decay amplitudes can also be expressed in terms of the angular momentum states of the decay. The angular momentum states allowed depend on the spins of the initial and final state particles, and also on their parity, if parity is conserved in the decay. The partial wave amplitude for the decay $1 \rightarrow 2 + 3$ is generally given as [71]

$$A_{PW}(\Omega; m_1, m_2, m_3) = \sum_{L,s} C_{s_2 s_3}(s\ m_s; m_2\ m_3) C_{Ls}(s_1\ m_1; m_L\ m_s) Y_L^{m_L}(\Omega) M(L,s). \quad \text{(A.37)}$$

The labels s_n and m_n refer to the spin and third component of spin for each of the particles. $M(L,s)$ are the amplitudes for each of the partial waves, and $Y_L^{m_L}$ is the spherical harmonic. The terms $C_{j_1 j_2}(j\ m; m_1\ m_2)$ are the Clebsch–Gordon coefficients for the combinations $\vec{s} = \vec{s}_2 + \vec{s}_3$ and $\vec{s}_1 = \vec{L} + \vec{s}$.

The partial wave method is just another basis for describing angular distributions in the decay, and can be related to the helicity formalism. The helicity amplitudes can be expressed in terms of the partial wave amplitudes using the Jacob Wick relation

$$A_{\lambda_2 \lambda_3} = \sqrt{\frac{2L+1}{2s_1+1}} \sum_{Ls} C_{s_2 s_3}(s\ m_1; \lambda_2\ -\lambda_3) C_{Ls}(s_1\ m_1; 0\ m_1) M(L,s). \quad \text{(A.38)}$$

This relationship can be inverted, giving the partial wave amplitudes in terms of the helicity amplitudes. For $\bar{B} \rightarrow D^* \ell^- \bar{\nu}$ we obtain

$$\begin{aligned} S &= \sqrt{\frac{1}{3}}(H_+ + H_0 + H_-) \\ P &= \sqrt{\frac{1}{2}}(H_- - H_+) \\ D &= (\sqrt{\frac{1}{6}} H_+ - \sqrt{\frac{2}{3}} H_0 + \sqrt{\frac{1}{6}} H_-), \end{aligned} \quad \text{(A.39)}$$

where S, P and D are the partial wave amplitudes for the $L = 0$, $L = 1$, and $L = 2$ states respectively. Using Equation 2.6, one can easily relate these partial wave amplitudes to the Lorentz invariant form factors given in Equation 2.3. We find

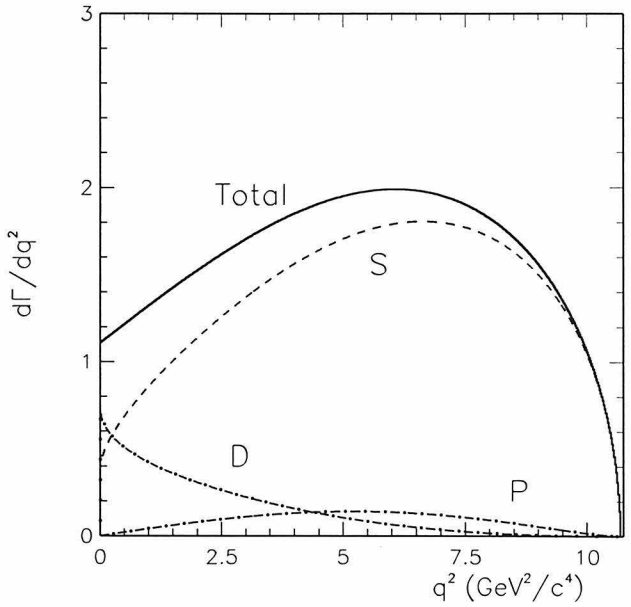


Figure A.2: Differential q^2 distribution and the contribution of the different partial wave amplitudes.

that the P wave amplitude is directly proportional to the vector form factor V, and that the S and D wave amplitudes are combinations of the A_1 and A_2 form factors.

After integrating over all variables except q^2, the decay rate in terms of partial wave amplitudes is given by

$$\frac{d\Gamma}{dq^2} = \frac{G_F^2 |V_{cb}|^2 P_{D^*} q^2}{96\pi^3 {m_B}^2}(|S|^2 + |P|^2 + |D|^2). \tag{A.40}$$

Figure A.2 plots the differential distribution in q^2, along with the contribution of each partial wave. The S wave contribution dominates the total decay rate over most of the q^2 range.

A.3 CP Violating Terms

In all previous mention of the helicity amplitudes, we have assumed that they are relatively real for the decay $\bar{B} \to D^* \ell^- \bar{\nu}$. Although in the Standard Model this is a good assumption, we can consider the possibility that the helicity amplitudes are

complex. In general the helicity amplitudes can be written as [71]

$$H_\lambda = \sum_k h_\lambda^k e^{i(\phi_k + \delta_\lambda^k)}, \tag{A.41}$$

where the sum is over the k diagrams that contribute to the final state, ϕ_k are the associated CKM phases and δ_λ^k is the strong phase due to final state interactions. The charge conjugate amplitude is

$$\overline{H}_\lambda = \sum_k h_{-\lambda}^k e^{i(-\phi_k + \delta_{-\lambda}^k)}. \tag{A.42}$$

In this case the helicity index and weak phase change sign, but the strong phase remains the same.

For $\bar{B} \to D^* \ell^- \bar{\nu}$, the leptonic and hadronic currents factorize, which is the same as saying there are no final state interactions. As a result, there is no strong phase associated with the helicity amplitude. For charged B mesons there is only one CKM phase contributing, and the helicity amplitude is $H_\lambda(q^2) = V_{cb} h_\lambda(q^2)$ with $h_\lambda(q^2)$ relatively real. Neutral B's also have a diagram that includes mixing. However, we measure the angular distributions integrated over all decay times. As a result, the interference between the mixing and direct diagrams vanish and the contribution of the mixing and direct terms give the identical result [71].

CP violation in $\bar{B} \to D^* \ell^- \bar{\nu}$ can result from the contribution of diagrams beyond the Standard Model, for example where the W is replaced by a charged Higgs boson. In this case the helicity amplitudes are complex, and the imaginary components of the helicity amplitudes contribute additional terms to the differential decay distribution given in Equation 2.9. These are given by [73]

$$\begin{aligned} \frac{d\Gamma_{T-odd}}{dq^2 d\cos\theta_\ell d\cos\theta^* d\chi} = \frac{3G_F^2 |V_{cb}|^2 P_{D^*} q^2 \mathcal{B}(D^* \to D\pi)}{8(4\pi)^4 m_B^2} [\\ -2(\sin^2\theta_\ell)(\sin^2\theta^* \sin 2\chi) \mathrm{Im}(H_+ H_-^*) \\ -4\sin\theta_\ell (1 - \cos\theta_\ell)(\sin\theta^* \cos\theta^* \sin\chi) \mathrm{Im}(H_+ H_0^*) \\ -4\sin\theta_\ell (1 + \cos\theta_\ell)(\sin\theta^* \cos\theta^* \sin\chi) \mathrm{Im}(H_- H_0^*)]. \end{aligned} \tag{A.43}$$

These additional interference terms are T-odd, or equivalently CP-odd assuming CPT invariance. These additional terms are distinct from the rest of the terms in the decay rate in that they are all proportional to $\sin\chi$ or $\sin 2\chi$. In contrast, only terms proportional to $\cos\chi$ and $\cos 2\chi$ appeared before. As a result, the angle χ must now be defined from 0 to 2π. Therefore the direction taken for the angle between the $\ell\nu$ and $D\pi$ decay planes is important.

That these additional angular terms are T-odd is shown by relating them to a triple product of 3 momenta which is odd under T. We have [73]

$$\begin{aligned} \sin\theta_\ell \sin\chi &\propto \vec{p}_\ell \cdot (\vec{p}_{D^*} \times \vec{p}_D), \\ \sin^2\theta_\ell \sin 2\chi &\propto \vec{p}_\ell \cdot \vec{p}_{D_\perp} \vec{p}_\ell \cdot (\vec{p}_{D^*} \times \vec{p}_D), \\ \sin 2\theta_\ell \sin\chi &\propto \vec{p}_\ell \cdot \vec{p}_{D^*} \vec{p}_\ell \cdot (\vec{p}_{D^*} \times \vec{p}_D), \end{aligned} \tag{A.44}$$

where $\vec{p}_{D_\perp}$ is the D momentum perpendicular to the D^* direction. The triple product $\vec{p}_\ell \cdot (\vec{p}_{D^*} \times \vec{p}_D)$ is a pseudoscalar that is odd under T, while the other scalar products are even under T.

The contribution of diagrams due to Higgs bosons, left-right symmetric models and other non-Standard Model physics has been discussed in [73, 74, 75]. These additional diagrams will lead to T violating effects in the decay. We look for non-zero values for the imaginary part of the helicity form factors, by plotting the observables given in Equation A.44. Figure A.3 plots these observables as well as χ from 0 to 2π, for the combined $D^{*+}(K\pi)$ and $D^{*0}(K\pi)$ modes. We find the expectation values of the observables to be consistent with zero.

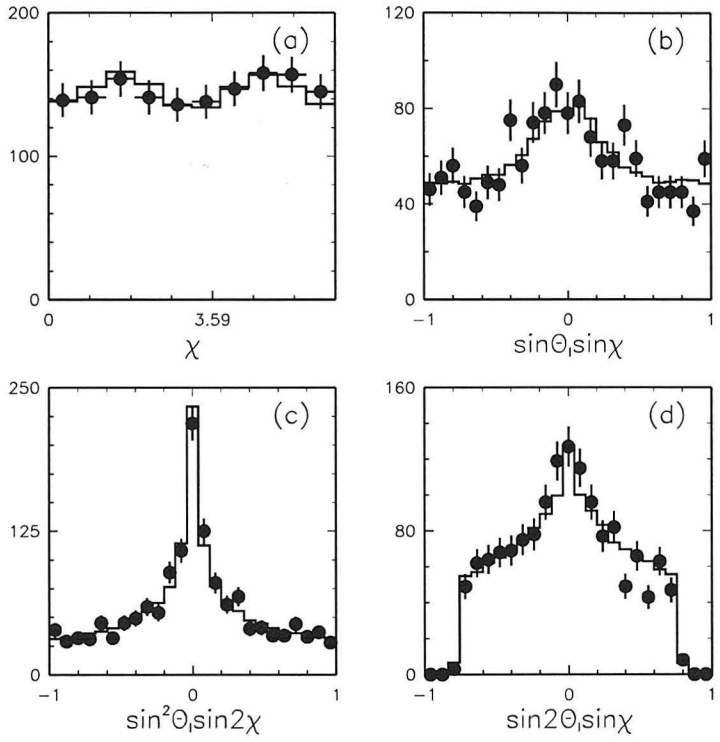


Figure A.3: a) χ from 0 to 2π. b-d) The T-odd observables given in Equation A.44. The points are the data and the solid line is signal MC.

Bibliography

[1] R. N. Cahn. The eighteen arbitrary parameters of the standard model in your everyday life. *Rev. Mod. Phys.*, 68:951, 1996.

[2] F. Halzen and D. Martin. *Quarks and Leptons.* John Wiley and Sons, New York, 1984.

[3] Particle Data Group. Review of particle physics. *Phys. Rev. D*, 54:1, 1996.

[4] Mandeepa Chadha. *A Measurement of the Michel Parameters ρ and η in Leptonic Tau Decays.* PhD thesis, California Institute of Technology, 1993.

[5] J. Richman and P. Burchat. Leptonic and semileptonic decays of charm and bottom hadrons. *Rev. Mod. Phys*, 67:893, 1995.

[6] T. Browder and K. Honscheid. B mesons. *Prog. Part. Nucl. Phys.*, 35:81, 1995.

[7] S. W. Herb *et al.* Observation of a dimuon resonance at 9.5-GeV in 400-Gev proton-nucleus collisions. *Phys. Rev. Lett.*, 39:252, 1977.

[8] D. Atwood and W. J. Marciano. Radiative corrections and semileptonic B decays. *Phys. Rev. D*, 41:1736, 1990.

[9] B. Barish *et al.* Measurement of the $\bar{B} \to D^* \ell^- \bar{\nu}$ branching fractions and $|V_{cb}|$. *Phys. Rev. D*, 51:1014, 1995.

[10] J. Kroll. Invited talk at 1997 Heavy Flavours Symposium.

[11] R. Ammar *et al.* Radiative penguin decays of the B meson. CLEO CONF 96-05. Contributed paper to ICHEP96, Warsaw, Poland, reference PA05-093.

[12] M. S. Alam *et al.* First measurement of the rate for the inclusive radiative penguin decay $b \to s\gamma$. *Phys. Rev. Lett.*, 74:2885, 1995.

[13] J. L. Hewitt. The role of top in heavy flavor physics. In *Proceedings of the XXIII SLAC Summer Institute on Particle Physics*, 1995.

[14] N. Isgur *et al.* Semileptonic B and D decays in the quark model. *Phys. Rev. D*, 39:799, 1989.

[15] Samuel Wong. *Introductory Nuclear Physics.* Prentice-Hall, New Jersey, 1990.

[16] M. Ademollo and R. Gatto. Nonrenormalizable theorem for the strangeness violating vector currents. *Phys. Rev. Lett.*, 13:264, 1964.

[17] M. E. Luke. Effects of subleading operators in the heavy quark effective theory. *Phys. Lett. B*, 252:447, 1990.

[18] L. Gibbons. Status of weak quark mixing, 1997. Invited talk at ICHEP96, Warsaw, Poland.

[19] R. J. Morrison D. M. Schmidt and M. S. Witherell. A general method of estimating physical parameters from a distribution with acceptance and smearing effects. *Nucl. Instrum. Methods A*, 328:547, 1993.

[20] A. Ryd. Invited talk at 1997 Heavy Flavours Symposium.

[21] J. G. Körner and G. A. Schuler. Exclusive semi-leptonic decays of bottom mesons in the spectator quark model. *Z. Phys. C*, 38:511, 1988.

[22] J. G. Körner and G. A. Schuler. Exclusive semileptonic heavy meson decays including lepton mass effects. *Z. Phys. C*, 46:93, 1990.

[23] F. J. Gilman and Jr. R. L. Singleton. Analysis of semileptonic decays of mesons containing heavy quarks. *Phys. Rev. D*, 41:142, 1990.

[24] J. G. Körner and G. A. Schuler. Aspects of the chirality of weak $b \to c$ transitions in the exclusive semi-leptonic decay $B(b) \to D^*(c)+\ell+\bar{\nu}_\ell$. *Phys. Lett. B*, 226:185, 1989.

[25] M. Gronau and S. Wakaizumi. Testing the chirality of b to c coupling in $\bar{B} \to D^* \ell^- \bar{\nu}$. *Phys. Lett. B*, 280:79, 1992.

[26] M. Neubert. Heavy quark symmetry. *Phys. Reports*, 245:259, 1994.

[27] N. Isgur and M. Wise. Weak decays of heavy mesons in the static quark approximation. *Phys. Lett. B*, 232:113, 1989.

[28] N. Isgur and M. Wise. Weak transition form factors between heavy mesons. *Phys. Lett. B*, 237:527, 1990.

[29] J.D. Bjorken, in *Results and Perspectives in Physics, Proceedings of the 4th Rencontres de Physique de la Valle d'Aoste, La Thuile, Italy* ed. by M. Greco (Editions Frontières, France), p. 583 (1990); and *Proceedings of the Eighteenth SLAC Summer Institute on Particle Physics, Gauge Bosons and Heavy Quarks, July 1990,* edited by J.F. Hawthorne, SLAC-Report-378, p. 167 (1991).

[30] A. K. Leibovich it et al. Model independent results for $B \to D_1(2420)\ell\bar{\nu}$ and $B \to D_2^*(2460)\ell\bar{\nu}$ at order $\Lambda_{QCD}/m_{c,b}$. *Phys. Rev. Lett.*, 78:3995, 1997.

[31] M. B. Voloshin. 'Optical' sum rule for form-factors of heavy mesons. *Phys. Rev. D*, 46:3062, 1992.

[32] A. G. Boyd it et al. Corrections to the Bjorken and Voloshin sum rules. *Phys. Rev. D*, 55:3027, 1997.

[33] F. E. Close and A. Wambach. Flavor dependence of form-factors in heavy meson decays. *Phys. Lett. B*, 348:207, 1995.

[34] M. Wirbel, B. Stech and M. Bauer. Exclusive semileptonic decays of heavy mesons. *Z. Phys. C*, 29:637, 1985.

[35] N. Isgur and D. Scora. Semileptonic meson decays in the quark model: an update. *Phys. Rev. D*, 52:2783, 1995.

[36] CESR Web Page. www.lns.cornell.edu/public/CESR/info/cesrinfo.html.

[37] M. Sands. The physics of electron storage rings: An introduction. SLAC-121, 1970.

[38] Y. Kubota *et al.* The CLEO II detector. *Nucl. Instrum. Methods A*, 320:66, 1992.

[39] S. Menary. Measuring the relative slow pion efficiency in the data and monte carlo. Internal CLEO note CBX92-103, 1992.

[40] B. Gittelman *et al.* Electron identification with CLEOII. Internal CLEO note CBX91-82, 1991.

[41] F. Muheim. Fake rates of leptons for the CLEO II detector. Internal CLEO note CBX92-104, 1992.

[42] B. Heltsley. Muon identification efficiencies. Internal CLEO note CBX92-117, 1992.

[43] C. Bebek *et al.* CLEOII trigger system. *Nucl. Instrum. Methods A*, 302:261, 1991.

[44] C. Bebek *et al.* A new data acquisition system for CLEO-II. *Nucl. Instrum. Methods A*, 338:447, 1994.

[45] A. Ryd and D. Lange. Internal CLEO note in preparation.

[46] A. Ryd and J. Richman. Measurement of the $\bar{B}^0 \to D^{*+}\ell^-\bar{\nu}$ form factors. Internal CLEO notes CBX94-32 and CBX95-82, 1994.

[47] G. Fox and S. Wolfram. Observables for the analysis of event shapes in e^+e^- annhiliation and other processes. *Phys. Rev. Lett.*, 41:1581, 1978.

[48] S. Roberts. TRKMAN for track quality. Internal CLEO note CBX92-103, 1992.

[49] J. C. Anjos *et al.* Dalitz plot analysis of $D \to K\pi\pi$ decays. *Phys. Rev. D*, 48:56, 1993.

[50] Ian C. Brock. MnFit a fitting and plotting package using MINUIT. Internal CLEO note CSN Note 245-B, 1992.

[51] N. Isgur and M. B. Wise. Excited charm mesons in semileptonic $\bar{B}$ decay and their contributions to a Bjorken sum rule. *Phys. Rev. D*, 43:819, 1991.

[52] P. Avery *et al.* Production and decay of $D_1(2420)^0$ and $D_2^*(2460)^0$. *Phys. Lett. B*, 331:236, 1994.

[53] T. Bergfeld *et al.* Observation of $D_1(2420)^+$ and $D_2^*(2460)^+$. *Phys. Lett. B*, 340:194, 1994.

[54] D. Buskulic *et al.* Production of orbitally excited charm mesons in semileptonic B decays. Contributed paper to ICHEP96, Warsaw, Poland, reference PA01-073.

[55] T.E. Browder *et al.* Measurement of semileptonic B meson decay to p-wave charm mesons. CLEO CONF 96-2. Contributed paper to ICHEP96, Warsaw, Poland, reference PA05-077.

[56] J. L. Goity and W. Roberts. Soft pion emission in semileptonic B-meson decays. *Phys. Rev. D*, 51:3459, 1995.

[57] C. O'Grady. *Exclusive Semi-leptonic decays of B Mesons.* PhD thesis, Cornell University, 1993.

[58] D. M. Schmidt. *Measurement of Charm Semileptonic Form-Factors.* PhD thesis, University of California, Santa Barbara, 1992.

[59] G. P. Yost. Lectures on probability and statistics, 1985.

[60] PROB, Cern Program Library Entry G100.

[61] Eadie *et al. Statistical Methods in Experimental Physics.* North-Holland, London, 1971.

[62] HDIFF, Cern Program Library Entry Y250.

[63] M. Garcia-Sciveres. Monte Carlo simulation of the ratio of neutral to charged slow pion efficiencies. Internal CLEO note CBX93-114, 1993.

[64] E. Barberio and Z. Was. PHOTOS - a universal monte carlo for QED radiative corrections: Version 2.0. CERN Report CERN-TH.7033/93, 1993.

[65] M. S. Alam *et al.* Exclusive hadronic B decays to charm and charmonium final states. *Phys. Rev. D*, 50:43, 1994.

[66] H. Albrecht *et al.* Investigation of the decays $\bar{B}^0 \to D^{*+}\ell^-\bar{\nu}$ and $\bar{B} \to D^{**}\ell^-\bar{\nu}$. *Z. Phys. C*, 57:533, 1993.

[67] S. Sanghera *et al.* Lepton asymmetry measurement in $\bar{B} \to D^*\ell^-\bar{\nu}$, implications for V-A and the form factors. *Phys. Rev. D*, 47:791, 1993.

[68] J. E. Duboscq *et al.* Measurement of the form factors for $\bar{B} \to D^*\ell^-\bar{\nu}$. *Phys. Rev. Lett.*, 76:3898, 1996.

[69] M. Acciarri *et al.* Measurement of the weak charged current structure in semileptonic b-hadron decays at the Z peak. *Phys. Lett. B*, 351:375, 1995.

[70] M. Neubert. Theoretical update on the model-independent determination of $|V_{cb}|$ using heavy quark symmetry. *Phys. Lett. B*, 338:84, 1994.

[71] R. Kutschke, 1996. An angular distribution cookbook.

[72] S. M. Bilenkii. *Basics of introduction to Feynman diagrams and electroweak interactions physics.* Editions Frontieres, Gif-sur-Yvette, France, 1994.

[73] J. G. Korner *et al.* T-odd and CP-odd triple momentum correlations in the exclusive semi-leptonic bottom meson decay $\bar{B} \to D^*\ell^-\bar{\nu}$. *Phys. Lett. B*, 242:119, 1990.

[74] E. Golowich and G. Valencia. Triple product correlations in semileptonic decays. *Phys. Rev. D*, 40:112, 1989.

[75] G. Wu *et al.* Polarization measurements and T-violation in exclusive semileptonic B decays. TRI-PP-97-13 hep-ph/9705293, 1997.